A Pseudo-Optimal Control Approach for a Redundant Degree-of-Freedom in a Gimbaled Mechanical System

by

Jason T. Smith

B.S. Mechanical Engineering
Brigham Young University, 2002

SUBMITTED TO THE DEPARTMENT OF AERONAUTICS AND ASTRONAUTICS
IN PARTIAL FULFILLMENT OF THE REQUIREMENTS FOR THE DEGREE OF

MASTER OF SCIENCE IN AERONAUTICS AND ASTRONAUTICS
at the
MASSACHUSETTS INSTITUTE OF TECHNOLOGY

June 2004

Signature of Author: _____
Department of Aeronautics and Astronautics
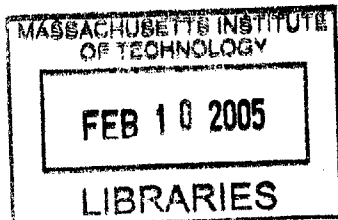May 14, 2004

Certified by: _____
Russell D. Smith
Charles Stark Draper Laboratory
Thesis Supervisor

Certified by: _____
Prof. Wallace E. Vander Velde
Professor Emeritus/Senior Lecturer
Thesis Advisor

Accepted by: _____
Edward M. Greitzer
H.N. Slater Professor of Aeronautics and Astronautics
Chair, Committee on Graduate Students

This page intentionally left blank.

A Pseudo-Optimal Control Approach for a Redundant Degree-of-Freedom in a Gimbaled Mechanical System

by

Jason T. Smith

Submitted to the Department of Aeronautics and Astronautics on
May 14, 2004 in Partial Fulfillment of the Requirements for the
Degree of Master of Science in Aeronautics and Astronautics

Abstract

Unaided inertial navigation systems of sufficient quality allow a missile or other body to navigate freely for potentially long periods of time. The use of four gimbals in such systems allows for elimination of large platform excursions while avoiding the uncontrollable condition of gimbal lock. The thesis investigates the benefits of applying a Linear Quadratic Regulator (LQR) to the control of the redundant degree-of-freedom present in a four gimbal inertial navigation system.

Equations of motion for a four gimbal system are defined and linearized. A benchmark controller is developed, using classical time and frequency domain techniques, for comparison with the LQR controller. The quadratic weightings for the LQR controller are investigated using principles of loop shaping. Due to the time-varying nature of the linearized gimbal system, optimal gains are calculated for a variety of nominal conditions and stored in a look-up table. The classical and LQR controllers, as well as models of the four gimbal system components and sensors, are evaluated strictly via simulation.

Metrics for determining controller performance are defined and a search is made for worst-case initial conditions and disturbances. A comparison with the benchmark controller at these worst-case conditions is made.

It is found that the LQR control technique is of significant benefit when applied to the redundant degree-of-freedom. In particular, several of the metrics show significant improvement and others show marginal improvement. Also, the LQR controller makes more complete use of the available torque capacity, improving the performance of the four gimbal system. Ideas for future areas of investigation are presented.

Technical Supervisor: Russell D. Smith
Title: Principle Member of the Technical Staff

Thesis Advisor: Professor Wallace E. Vander Velde
Title: Professor Emeritus/Senior Lecturer

This page intentionally left blank.

ACKNOWLEDGEMENTS

I would like to express my appreciation first and foremost to my wife Jeni and our two beautiful daughters, Kamryn and Lindsy. Their unwavering support and gentle encouragement have made the long hours of my graduate experience bearable. Also, I wish to thank my parents for their examples both in education and in life, and my brother for knowing how to make me laugh. I love you all.

To my friends here in Boston; Dave, Doreen, Adam, Leslie, Marshall, Andrew, Steven, David, Ryan, Tiffany and Luke, thanks for all the good times, fond memories, and help with tough classes and crying babies.

This thesis would not have been possible without help from many wonderful people at Draper Laboratory. I especially wish to thank Chris Gibson, for his excellent answers to countless questions and for going above and beyond in helping this project come to fruition. Also, I am indebted to Russell Smith, for knowing the answers when nobody else did. In addition, my thanks go to Dave Baumgart and Nathan Lowry for taking the time to review much of this thesis.

Finally, I need to thank my thesis advisor, Professor Vander Velde, who has helped a great deal in defining the scope of this thesis and in reviewing its technical contents. I am grateful for the time he has spent instructing me, both in classes and throughout my thesis work.

Jason T. Smith   Date

This page intentionally left blank.

Table of Contents

List of Tables

This page intentionally left blank.

List of Figures

This page intentionally left blank.

Chapter 1

Introduction

1.1 Inertial Navigation

The theory behind inertial navigation has been well known for several decades. Utilized in a wide variety of applications, including airplanes, submarines, missiles, and spacecraft, an aided or unaided inertial navigation system (INS) provides reliable, uninterrupted determination of position and velocity via measured acceleration [12]. Historically, an INS offered a solution to some very complex navigational situations including fighter aircraft, ballistic missiles, and even the Apollo moon landings [12]. Today, unaided INS continues to be important due to its independent operation. Unlike more recent aided INS schemes which utilize technologies such as Global Positioning System (GPS) satellites for error corrections, unaided inertial systems must be capable of freely navigating for potentially long periods of time without using external sources for corrections [1]. This demand for long periods of free navigation generally necessitates high quality, gimbaled systems.

In three dimensions, six generalized coordinates are required to fix a body in inertial space; three for linear position and three for angular rotation. Considering the body to be a point mass and hence ignoring the angular rotation, six states are required for navigation; three for position and three for velocity. If the linear acceleration is known, along with the proper initial conditions, double integration of the second-order

translational equations of motion will yield velocity and position. This is the theory under which an INS operates.

At the most basic level, an INS consists of three accelerometers mounted orthogonally to a platform, along with three orthogonal gyroscopes in a fixed and known orientation relative to the accelerometers. The gyros sense the motion of the platform relative to inertial space. This information, along with the accelerations, can be used to compute the velocity and position.

For a variety of reasons, it is desirable to limit as much as possible, erratic motions of the platform. Although it is theoretically possible to calculate velocity and position regardless of platform motion, doing so for large excursions of the platform away from the inertial reference frame introduces large measurement errors [1]. As long as the platform rotation is stabilized close to inertial space, the measurement errors remain small and the calculated position and velocity of the body remain accurate. To stabilize the platform, it is mounted inside a series of four gimbals, each with a single axis of rotation and torque motor. The outermost gimbal is mounted to a case which is suitably attached to the body. Deviations in platform orientation from inertial space are sensed by the relative motion of the gyro axes with respect to the platform and are called gyro errors. By applying torque to the proper gimbals to null the gyro errors, large platform excursions can be eliminated regardless of the orientation of the carrier vehicle.

This thesis will investigate the scheme for controlling the platform to prevent large platform motions in the case of a long-range missile. First, a control design utilizing classical time and frequency domain techniques will be presented. Then, a controller using more modern optimal control techniques will be outlined. These two controllers will be compared on the basis of a series of metrics which will be outlined. Ultimately, the objective will be to show that by using optimal control techniques, the torque resources available can be put to better use in preventing large platform motions than with the classical techniques.

Although an attempt at using optimal control techniques for platform control has been made previously [14], the current attempt restricts the optimization to the redundant degree-of-freedom. In this way, a more accurate understanding of the importance of the redundant controller can be obtained. In addition, this thesis presents a new and thorough method for calculating the nominal conditions associated with the optimal controller.

1.2 Thesis Organization

The thesis is divided into six chapters. Chapter 1 is the introduction, giving background about inertial navigation systems and an overview of the thesis. Chapter 2 contains a description of a four gimbal system including generalized physical parameters of the hardware components. The nonlinear equations of motion for the four gimbal system are presented. Also, Chapter 2 contains a discussion of the linearization of the system. This linearization is necessary when working with the optimal control technique. Finally, testing of the linearized system model is presented.

Chapter 3 discusses a controller design using the principles of classical control theory. Time and frequency domain requirements are given and a controller meeting these requirements is outlined. In addition, Chapter 3 introduces the need for a Gimbal Lock Avoidance (GLA) compensator and outlines the design of this compensator. The platform controller presented is used as a benchmark for comparison with the optimal controller.

Chapter 4 explains the design of a pseudo-optimal, Linear Quadratic Regulator (LQR) controller. A cost function and weightings are defined and a simplified version of the linearized system from Chapter 2 is utilized in calculating optimal LQR gains. The optimal controller is then implemented in a software version of the four gimbal system.

Chapter 5 presents a set of missile maneuvers designed to test the classical and LQR versions of the platform controller. Also, metrics on which the two controllers can be

compared are defined. Finally, results of the two control schemes are presented in a series of plots and tables.

Chapter 6 presents conclusions which can be drawn from the results presented in Chapter 5. In addition, ideas for future work and areas for further investigation are presented.

Four appendices are included in the thesis. Appendix A gives the derivation of the nonlinear equations of motion for the four gimbal system. Appendix B includes definitions of terms generated by the linearization of the system. Appendix C presents the calculation of nominal conditions which are utilized by the optimal controller. Appendix D shows diagrams of the four gimbal system as implemented in Matlab Simulink software.

Chapter 2

The Four Gimbal System

2.1 The Feedback Control System

The figure below shows a diagram of the four gimbal Inertial Navigation System including axis and angle definitions. For ease of viewing, the gimbals are represented by rings. Each gimbal angle is defined as a relative angle between the gimbal and the gimbal immediately exterior to it, measured along the rotational axis. The gimbals are called the outer, middle, inner, and instrumentation platform gimbals and the angles are numbered starting with the outer and working in to the platform as follows: $\theta_1, \theta_2, \theta_3, \theta_4$. The accelerometers and gyroscopes are mounted on the innermost, or instrumentation platform gimbal.

The missile is limited to a maximum angular rate of rotation about any axis of 45 degrees per second. In addition, the maximum angular acceleration of the missile is 3 radians per second squared. As missile motion will be treated as a disturbance, these limits define the worst-case platform disturbance conditions.

A diagram of the four gimbal system is as follows.
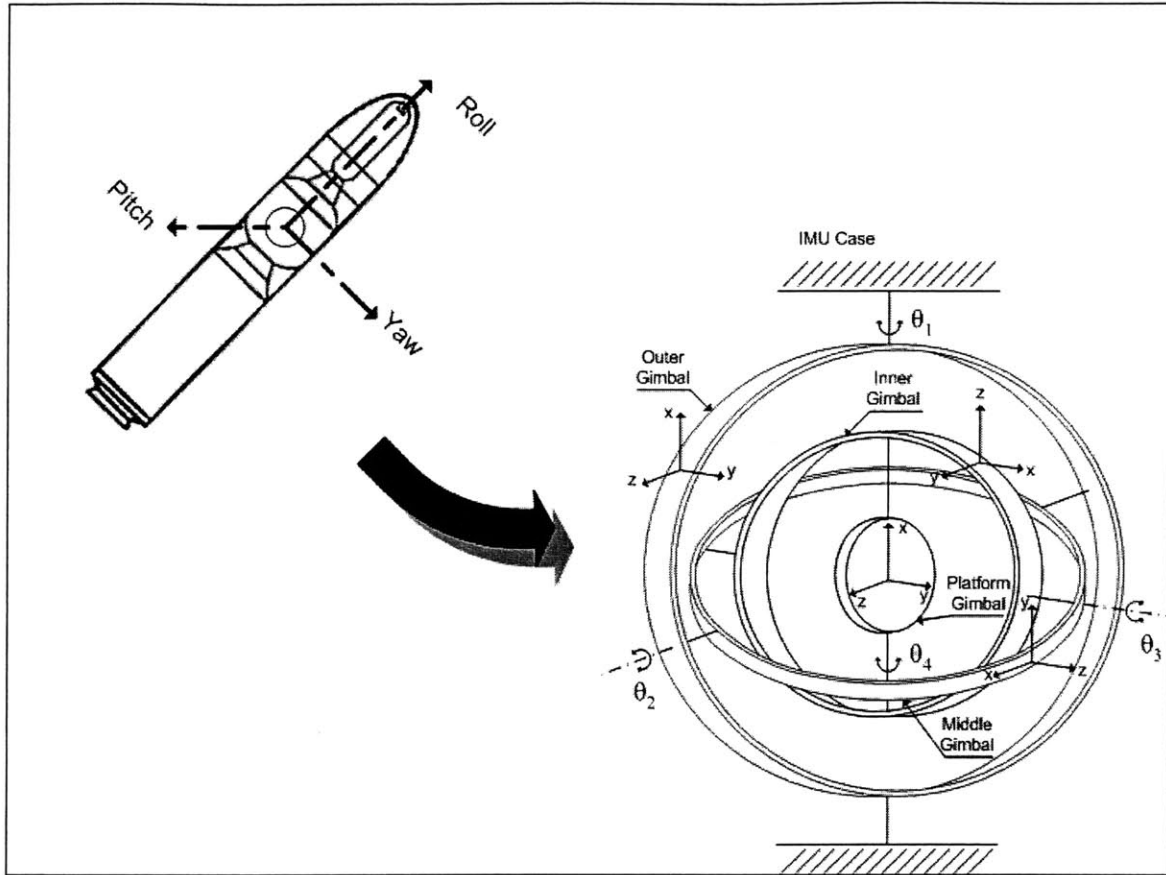
Figure 2.1.1 - The four gimbal system as mounted inside a representative missile.

The Inertial Measurement Unit or IMU case is attached to the missile, or other moving body, via elastic, shock isolation mounts. In Figure 2.1.1 above, the gimbals appear with all gimbals angles at zero degrees, also called the all-attitude zero configuration. As a feedback control system block diagram, the closed-loop system appears as follows.
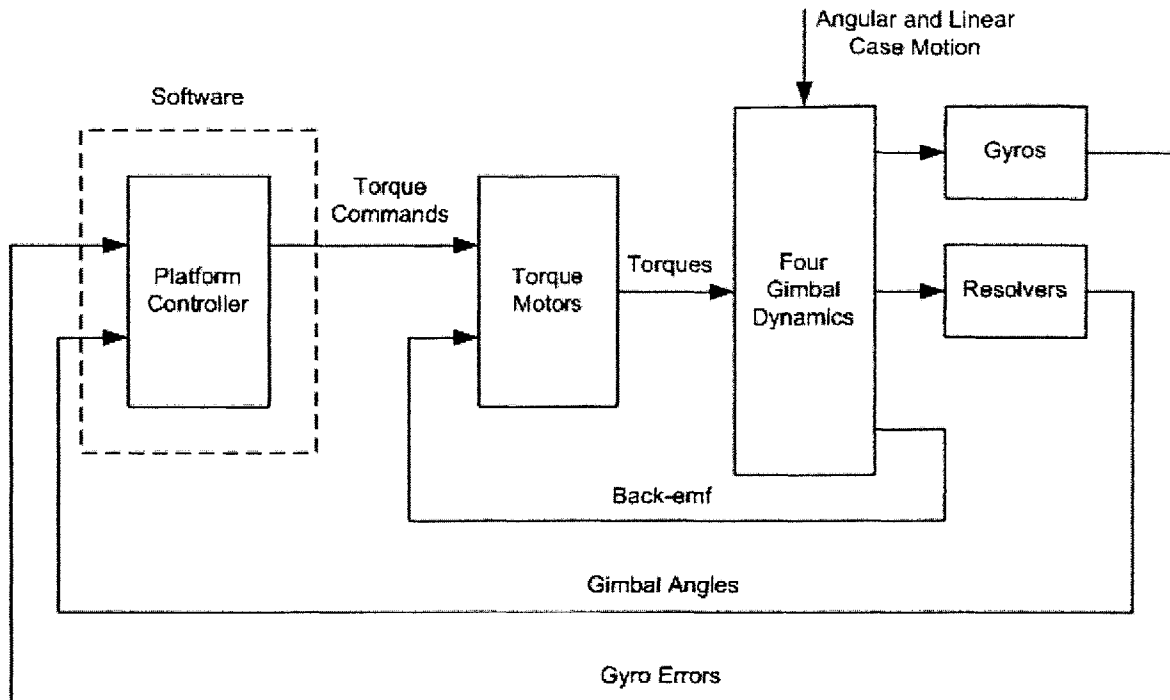
Figure 2.1.2 - Block diagram of the four gimbal closed-loop feedback control system.

As can be seen in Figure 2.1.2 above, the closed-loop system contains both hardware and software components, with the software components confined to the dashed box. For the design, implementation, and testing of the platform controllers discussed in this thesis, the entire closed-loop system of Figure 2.1.2 will be simulated using Matlab Simulink. The remainder of this chapter will describe the hardware components found outside of the dashed box in Figure 2.1.2. Subsequent chapters will focus on the platform controller inside the dashed box.

2.2 The Hardware Components

The following sections contain descriptions of the various hardware components in the four gimbal system in Figure 2.1.2. All of these components are modeled in Simulink for the testing of the controllers which will eventually be presented. In addition, it should be noted that the components presented below are not taken from any particular missile system. Instead, they are intended to represent a realistic, if not actual, missile system.

21

2.2.1 The Gimbals

The four gimbal dynamic system is here represented by the following inertias.

$$J^1 = \begin{bmatrix} J^1_{xx} & 0 & 0 \\ 0 & J^1_{yy} & 0 \\ 0 & 0 & J^1_{zz} \end{bmatrix} \Rightarrow J^1_s = \begin{bmatrix} 0.07 & 0 & 0 \\ 0 & 0.07 & 0 \\ 0 & 0 & 0.07 \end{bmatrix} ft \cdot lb \cdot s^2 \qquad (2.2.1)$$

$$J^2 = \begin{bmatrix} J^2_{xx} & 0 & 0 \\ 0 & J^2_{yy} & 0 \\ 0 & 0 & J^2_{zz} \end{bmatrix} \Rightarrow J^2_s = \begin{bmatrix} 0.06 & 0 & 0 \\ 0 & 0.06 & 0 \\ 0 & 0 & 0.06 \end{bmatrix} ft \cdot lb \cdot s^2 \qquad (2.2.2)$$

$$J^3 = \begin{bmatrix} J^3_{xx} & 0 & 0 \\ 0 & J^3_{yy} & 0 \\ 0 & 0 & J^3_{zz} \end{bmatrix} \Rightarrow J^3_s = \begin{bmatrix} 0.04 & 0 & 0 \\ 0 & 0.04 & 0 \\ 0 & 0 & 0.04 \end{bmatrix} ft \cdot lb \cdot s^2 \qquad (2.2.3)$$

$$J^4 = \begin{bmatrix} J^4_{xx} & 0 & 0 \\ 0 & J^4_{yy} & 0 \\ 0 & 0 & J^4_{zz} \end{bmatrix} \Rightarrow J^4_s = \begin{bmatrix} 0.05 & 0 & 0 \\ 0 & 0.05 & 0 \\ 0 & 0 & 0.05 \end{bmatrix} ft \cdot lb \cdot s^2 \qquad (2.2.4)$$

The J terms in (2.2.1) to (2.2.4) represent moments of inertia with the products of inertias being neglected. For example, the J^2_{xx} term represents the moment of inertia of gimbal two about its x axis, and so forth. In addition, for simplification, differences in moments have been neglected, thus allowing for the spherical inertias as defined above.

It can be observed in (2.2.4) above that it is assumed that the platform gimbal has a slightly higher inertia than the inner gimbal, despite the fact that the inner gimbal would necessarily be physically larger. The inertia of the platform gimbal is taken to be larger

due to its denser material properties as well as the gyros and accelerometers mounted on the instrumentation platform.

2.2.2 The Torque Motors

The gimbals are controlled via four torque motors, one mounted to each gimbal. The assumed torque motor characteristics are in the table below.

Table 2-1 Parameters of the four gimbal torque motors

Parameter	Description	Outer	Middle	Inner	Platform	Units
Kt	Torque Constant	9.008	4.323	1.773	1.698	ft-lb/A
R	Motor Resistance	8.2	7.5	15	15	ohms
Kv	Motor Back-emf	0.0804	0.0353	0.0289	0.0277	V-s/rad
Pk	Peak Torque	32.96	17.29	3.55	3.40	ft-lb

In Table 2-1 above, the motors are designed for a maximum voltage of 30 volts. The torque motors are sized based on the amount of inertia they are required to drive. As this effective inertia varies with gimbal configuration, the all-attitude zero location is chosen for simplicity. Here, the following effective inertias must be driven by each of the torque motors.

$$J_{eff}^{OG} = J_{xx}^1 + J_{yy}^2 + J_{zz}^3 = 0.17 ft \cdot lb \cdot s^2 \qquad (2.2.5)$$

$$J_{eff}^{MG} = J_{xx}^2 + J_{yy}^3 + J_{zz}^4 = 0.15 ft \cdot lb \cdot s^2 \qquad (2.2.6)$$

$$J_{eff}^{IG} = J_{xx}^3 + J_{yy}^4 = 0.09 ft \cdot lb \cdot s^2 \qquad (2.2.7)$$

$$J_{eff}^{PG} = J_{xx}^4 = 0.05 ft \cdot lb \cdot s^2 \qquad (2.2.8)$$

The definitions in (2.2.5) to (2.2.8) can be explained by observing Figure 2.1.1. Take, for example, the outer gimbal torque motor. At all-attitude zero, the x axis of the outer gimbal is aligned with the y axis of the middle gimbal, the z axis of the inner gimbal and the x axis of the platform gimbal. As the x axis is the degree-of-freedom for the platform gimbal and would be free to counter-rotate in this configuration, its inertia is not included. Hence, the effective inertia the outer gimbal torque motor must drive at all-attitude zero is given by (2.2.5). The other effective inertias are defined in a similar manner.

It can be easily seen in (2.2.5) to (2.2.8) that the outer motors are required to drive much larger inertias and therefore must have a larger torque capacity. To this end, the following are the ratios of peak torque to effective inertias.

$$P_k^{OG} \big/ J_{eff}^{OG} = 193.9 \qquad\qquad (2.2.9)$$

$$P_k^{MG} \big/ J_{eff}^{MG} = 115.3 \qquad\qquad (2.2.10)$$

$$P_k^{IG} \big/ J_{eff}^{IG} = 39.4 \qquad\qquad (2.2.11)$$

$$P_k^{PG} \big/ J_{eff}^{PG} = 67.9 \qquad\qquad (2.2.12)$$

In (2.2.9) to (2.2.12) above, it is observed that the outer and middle ratios are significantly higher, due to the larger inertias which must be driven. Also, the platform ratio is somewhat larger than the inner ratio due to the added inertia of the accelerometers and gyroscopes on the platform.

Were the four gimbal system in Figure 2.1.2 to be implemented in hardware, the various components would need a method for communication. In trying to preserve this communication method in the Matlab simulation, the following units of bits are

introduced. The torque motor commands are quantized with a range of ± 30 volts and the following quantization level.

$$1 \ torque \ motor \ bit = 2.72 \ mV \qquad (2.2.13)$$

Thus, each torque motor has a range of ± 11,029 bits. All four torque motors have the same voltage quantization level but, as can be seen in Table 2-1, the torque constants are different. Thus, one bit of motor torque produces an equivalent torque command in volts but a different torque command in foot pounds across the four motors.

2.2.3 The Gyros

The gyros in Figure 2.1.2 are rate integrating gyros. Thus, the gyro errors, as shown in Figure 2.1.2, are actually the integrated inertial rates of the platform about each of the three gyro axes. Also, it is assumed that the gyros have the convenient range of ± 0.0175 radians. The continuous gyro error signals from the four gimbal dynamics are quantized with the following quantization interval.

$$1 \ gyro \ bit = 1.75 \times 10^{-6} \ radians \qquad (2.2.14)$$

Thus, a gyro error signal with a range of ± 10,000 bits is obtained.

Up to this point, several assumptions have been made to simplify as much as possible the components of the closed-loop system for the purposes of simulation. However, in an attempt to model an actual system more closely, some filtering has been added to the gyro error measurements. A real system would almost certainly contain some type of filtering on the error signals to reduce as much as possible the effects of noise or harmonics caused by the gyros themselves [15]. In the case of the four gimbal system, filters have been added, but they will be understood to be part of the gyros. As the filters

have been normalized, the net result appears in the controller as a reduction in phase margin.

2.2.4 The Resolvers

In Figure 2.1.2, the relative gimbal angles from the four gimbal dynamics are measured via four resolvers, one about each gimbal axis. These resolvers report gimbal angle with the following assumed resolution.

$$1 \ resolver \ bit = 5.992 \times 10^{-6} \ radians \qquad (2.2.15)$$

As expected, each resolver also has a range of $\pm \ \pi$ radians. Thus, each gimbal angle has a range of $\pm$ 524,288 bits.

Although the communication bits for the torque motors, gyros and resolvers are introduced above in order to represent the hardware accurately in the software model, it should be noted that it was assumed that no communication delay exists between the blocks in Figure 2.1.2. In a real hardware system such delay would exist, but it would be very minor.

2.3 The Four Gimbal Dynamics

The four gimbal dynamics block of Figure 2.1.2 consists of the four concentric gimbals as further detailed in Figure 2.1.1, which are assumed to be rigid. The figure below shows the set of body-fixed reference frames relevant to the system.
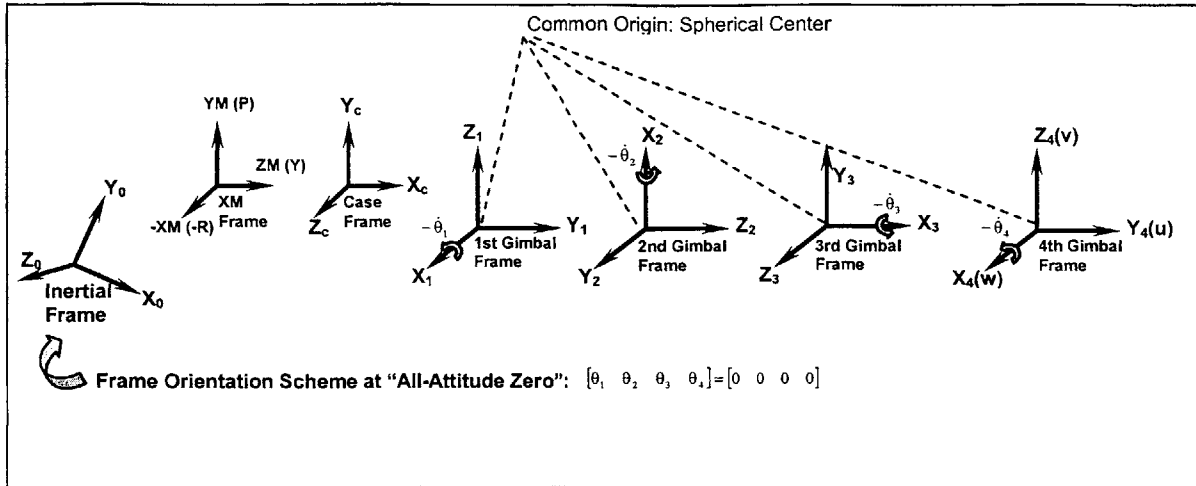
Figure 2.3.1 - Reference Frames.

In keeping with Figure 2.1.1, Figure 2.3.1 is intended to convey that, while each gimbal has its own reference frame, they may be conveniently taken so as to share a common origin. While the definitions of reference frames in Figure 2.3.1 above are convenient, it should not be implied that these are the only choices possible. Also defined in Figure 2.3.1 are a case-fixed frame and the XM, or missile-fixed, frame.

Because the case is attached to the missile, the case is also missile-fixed to within the small, elastic degrees-of-freedom afforded by the shock isolation mounts. Thus, the case frame is a mere permutation of the roll, pitch, and yaw missile frame axes. This straightforward permutation is as follows: the x component of the case frame is taken as missile yaw, the y component as missile pitch, and the z component as negative roll. Generally, the case frame will be used instead of the missile frame. Also, the transformation from one gimbal frame to the next inner frame is as follows [13].

$$T_i^{i+1} = \begin{bmatrix} 0 & 0 & 1 \\ c\theta_{i+1} & -s\theta_{i+1} & 0 \\ s\theta_{i+1} & c\theta_{i+1} & 0 \end{bmatrix} \qquad (2.3.1)$$

A series of the transformation matrices in (2.3.1) may be used to transform between reference frames which are not adjacent.

Each gimbal is acted upon by a torque motor to control its rotational axis. According to the arbitrary definition of reference frames Figure 2.3.1, the x axis is defined as the independent axis degree-of-freedom of each gimbal, meaning, the motor is free to rotate the gimbal about this axis. The gimbal will generally rotate about the y and z axes as well, but by using a series of transformation matrices, this kinematically dependent motion can be mapped to the motion of the other gimbals about their independent x axes (the gimbal rotational velocity states) plus case motion driving disturbances. As angular control is the only concern here, linear acceleration is treated as an external input which, by non-coincidence of center-of-gravity with gimbal rotational axes, could allow for additional torque disturbances.

The four gimbal system is described with a state vector of eight components as follows.

$$\underline{x}(t) = \begin{bmatrix} \varpi_{1x} & \varpi_{2x} & \varpi_{3x} & \varpi_{4x} & \theta_1 & \theta_2 & \theta_3 & \theta_4 \end{bmatrix}^T \qquad (2.3.2)$$

The first four states in (2.3.2) are the inertial angular velocity components of the respective gimbals about their degree-of-freedom axes. The over-bar notation is adopted here and elsewhere to convey the fact that the vector is expressed in a rotating, body-fixed reference frame such as those depicted in Figure 2.3.1. The x subscript indicates the x component of the vector.

The second four scalar-valued states are the relative gimbal angles, or the angle of each gimbal relative to the gimbal immediately exterior to it. They are taken as displacement states.

The four gimbal system also has four control inputs.

$$\underline{u}(t) = \begin{bmatrix} \tau_1^{mot} & \tau_2^{mot} & \tau_3^{mot} & \tau_4^{mot} \end{bmatrix}^T \qquad (2.3.3)$$

The four control inputs are the torque components generated by the torque motors mounted on each gimbal. It should be noted that these are the net external mechanical torques after accounting for any back-emf or frictional losses.

The derivation of the equations of motion for the four gimbal system is described in Appendix A. This will be used, with a slight simplification. For the first four states, the governing equation is (A.6), repeated here.

$$\dot{\underline{\omega}}_{ind} = M_{sys}^{-1}\left[B^{T}P^{T}\left(Q_{e}+Q_{v}\right)-B^{T}P^{T}MP\overline{Q}_{c}\right]$$
(2.3.4)

The independent angular accelerations are the x axis accelerations for the reasons discussed previously.

$$\dot{\underline{\omega}}_{ind} = \begin{bmatrix}\dot{\omega}_{1x} & \dot{\omega}_{2x} & \dot{\omega}_{3x} & \dot{\omega}_{4x}\end{bmatrix}^{T}$$
(2.3.5)

There are three torque components on the right hand side of equation (2.3.4). The Q_e term contains the actual, external mechanical torques acting on the system including motor torques, friction, and so forth, but modified by sine and cosine projections to account for reactive effects. The motor torque elements have already been defined as inputs. The Q_v term contains the velocity dependent or gyroscopic momentum terms. Although these are calculable and could be taken into account, they will remain zero here due to the assumption of equal moments of inertia. The $\overline{Q}_c$ term is a momentum forcing function due to the angular kinematic case inputs.

The M_{sys} term is the system mass matrix. When evaluated from (A.7), it is as follows.

$$M_{sys} = \begin{bmatrix} J_{ox} & -\left(c\theta_{3}s\theta_{3}c\theta_{2}\right)J_{s}^{4} & 0 & 0 \\ -\left(c\theta_{3}s\theta_{3}c\theta_{2}\right)J_{s}^{4} & J_{mx} & 0 & 0 \\ 0 & 0 & J_{ix} & 0 \\ 0 & 0 & 0 & J_{s}^{4} \end{bmatrix}$$
(2.3.6)

Here, some approximations are made.

$$J_{ox} \approx J_{xx}^1 + J_s^2 + c\theta_2^2 J_s^3 + c\theta_2^2 s\theta_3^2 J_s^4 \tag{2.3.7}$$

$$J_{mx} \approx J_{xx}^2 + J_s^3 + c\theta_3^2 J_s^4 \tag{2.3.8}$$

$$J_{ix} \approx J_{xx}^3 + J_s^4 \tag{2.3.9}$$

$$J_s^{2,3,4} \approx \left(J_{xx}^{2,3,4} + J_{yy}^{2,3,4} + J_{zz}^{2,3,4} \right)/3 \tag{2.3.10}$$

Utilizing equations (A.8), (A.12), (A.18), and (A.20), as well as the inversion of the mass matrix, the following simplification of equation (2.3.4) is obtained.

$$\frac{d}{dt}\begin{bmatrix} \varpi_{1x} \\ \varpi_{2x} \\ \varpi_{3x} \\ \varpi_{4x} \end{bmatrix} = \begin{bmatrix} \frac{J_{mx}}{\Delta}\left(\tau_1 - s\theta_2\tau_3 - c\theta_2 c\theta_3 \tau_4 - \tau_1^{ff}\right) + \frac{\left(c\theta_2 c\theta_3 s\theta_3 J_s^4\right)}{\Delta}\left(\tau_2 - s\theta_3\tau_4 - \tau_2^{ff}\right) \\ \frac{\left(c\theta_2 c\theta_3 s\theta_3 J_s^4\right)}{\Delta}\left(\tau_1 - s\theta_2\tau_3 - c\theta_2 c\theta_3 \tau_4 - \tau_1^{ff}\right) + \frac{J_{ox}}{\Delta}\left(\tau_2 - s\theta_3\tau_4 - \tau_2^{ff}\right) \\ \frac{1}{J_{ix}}\left(\tau_3 - \tau_3^{ff}\right) \\ \frac{\tau_4}{J_s^4} \end{bmatrix} \tag{2.3.11}$$

Here, the delta term is defined for convenience.

$$\Delta = J_{ox}J_{mx} - c\theta_2^2 c\theta_3^2 s\theta_3^2 J_s^4 J_s^4 \tag{2.3.12}$$

Also, the $\tau_{1,2,3}^{ff}$ terms are the forcing function terms as a result of the expansion of the $B^T P^T M P \overline{Q}_c$ term. They are complex functions of gimbal angles, inertias, case angular velocities, and case angular accelerations and can be found in Appendix B.

30

Before going further, six kinematic disturbances to the system, which come from the missile motion, are defined. Linear acceleration disturbance inputs are eliminated due to the assumption of equal moments of inertia.

$$\underline{d}(t) = \begin{bmatrix} \dot{\varpi}_{cx} & \dot{\varpi}_{cy} & \dot{\varpi}_{cz} & \varpi_{cx} & \varpi_{cy} & \varpi_{cz} \end{bmatrix}^{T} \tag{2.3.13}$$

The six disturbances are the x, y, and z components, transformed from roll-pitch-yaw driving motion as mentioned above, of the case absolute angular acceleration and velocity respectively.

To solve for the gimbal angles, the gimbal angle convention (A.19) is used. As stated previously, gimbal angles are relative angles between the gimbal and the gimbal directly exterior to it. Hence, as given by (A.23), this is the expression for the gimbal angle rates.

$$\begin{bmatrix} \dot{\theta}_1 \\ \dot{\theta}_2 \\ \dot{\theta}_3 \\ \dot{\theta}_4 \end{bmatrix} = \begin{bmatrix} -1 & 0 & 0 & 0 \\ 0 & -1 & 0 & 0 \\ s\theta_2 & 0 & -1 & 0 \\ c\theta_3 c\theta_2 & s\theta_3 & 0 & -1 \end{bmatrix} \begin{bmatrix} \varpi_{1x} \\ \varpi_{2x} \\ \varpi_{3x} \\ \varpi_{4x} \end{bmatrix} + \begin{bmatrix} [0 & 0 & 1]\varpi_c \\ [s\theta_1 & c\theta_1 & 0]\varpi_c \\ c\theta_2[c\theta_1 & -s\theta_1 & 0]\varpi_c \\ -c\theta_3 s\theta_2[c\theta_1 & -s\theta_1 & 0]\varpi_c \end{bmatrix} \tag{2.3.14}$$

Substituting and simplifying yields this expression for the gimbal angles.

$$\frac{d}{dt}\begin{bmatrix} \theta_1 \\ \theta_2 \\ \theta_3 \\ \theta_4 \end{bmatrix} = \begin{bmatrix} -\varpi_{1x} + \varpi_{cz} \\ -\varpi_{2x} + s\theta_1 \varpi_{cx} + c\theta_1 \varpi_{cy} \\ s\theta_2 \varpi_{1x} - \varpi_{3x} + c\theta_1 c\theta_2 \varpi_{cx} - s\theta_1 c\theta_2 \varpi_{cy} \\ c\theta_2 c\theta_3 \varpi_{1x} + s\theta_3 \varpi_{2x} - \varpi_{4x} - c\theta_1 s\theta_2 c\theta_3 \varpi_{cx} + s\theta_1 s\theta_2 c\theta_3 \varpi_{cy} \end{bmatrix} \tag{2.3.15}$$

Equations (2.3.11) and (2.3.15) above fully describe the four gimbal system as a function of states, inputs, and disturbances. It should be quite obvious that this is a highly nonlinear system.

2.4 System Linearization

As is common with nonlinear systems, the four gimbal dynamic system described in section 2.3 will be linearized about nominal operating points. This step is important as it will yield a sufficiently linear and time-invariant system, two conditions needed for the eventual optimal control design.

Consider a general, nonlinear system as a function of states, $\underline{x}(t)$, inputs, $\underline{u}(t)$, and disturbances, $\underline{d}(t)$. The system can be described by the following differential equation.

$$\dot{\underline{x}}(t) = f\{\underline{x}(t), \underline{u}(t), \underline{d}(t)\} \tag{2.4.1}$$

By taking a Taylor series expansion of (2.4.1) about nominal conditions $\underline{x}_N(t)$, $\underline{u}_N(t)$, $\underline{d}_N(t)$, and discarding all terms higher than first order, the following equation is obtained [2].

$$f\{\underline{x}, \underline{u}\} = f\{\underline{x}_N, \underline{u}_N\} + A\{\underline{x} - \underline{x}_N\} + B\{\underline{u} - \underline{u}_N\} + G\{\underline{d} - \underline{d}_N\} \tag{2.4.2}$$

Note that each term in equation (2.4.2) above is a function of time, although the time arguments have been dropped for visual clarity. Also in (2.4.2) above, A, B, and G are Jacobian matrices with the following definitions [2].

$$A(t)_{i,j} = \frac{\partial f_i}{\partial x_j}\bigg|_{x_N(t), u_N(t), d_N(t)} \tag{2.4.3}$$

$$B(t)_{i,j} = \frac{\partial f_i}{\partial u_j}\bigg|_{x_N(t), u_N(t), d_N(t)} \tag{2.4.4}$$

$$G(t)_{i,j} = \left. \frac{\partial f_i}{\partial d_j} \right|_{x_N(t), u_N(t), d_N(t)}$$

(2.4.5)

The perturbed conditions, $\delta \underline{x}(t)$, $\delta \underline{u}(t)$, $\delta \underline{d}(t)$, can be defined as functions of states, inputs, and disturbances and nominal states, inputs, and disturbances in the following manner.

$$\delta \underline{x}(t) = \underline{x}(t) - \underline{x}_N(t)$$

(2.4.6)

$$\delta \underline{u}(t) = \underline{u}(t) - \underline{u}_N(t)$$

(2.4.7)

$$\delta \underline{d}(t) = \underline{d}(t) - \underline{d}_N(t)$$

(2.4.8)

The nominal system can be further defined as follows.

$$\underline{\dot{x}}_N(t) = f\{\underline{x}_N(t), \underline{u}_N(t), \underline{d}_N(t)\}$$

(2.4.9)

Now, by substituting (2.4.1), (2.4.6), (2.4.7), (2.4.8), and (2.4.9) into (2.4.2), the following differential equation is obtained.

$$\underline{\dot{x}}(t) = \underline{\dot{x}}_N(t) + A(t)\delta \underline{x}(t) + B(t)\delta \underline{u}(t) + G(t)\delta \underline{d}(t)$$

(2.4.10)

By taking the derivative of (2.4.6) and using this to simplify (2.4.10), it can be easily shown that the following linear system describes the perturbed states [2].

$$\delta \underline{\dot{x}}(t) = A(t)\delta \underline{x}(t) + B(t)\delta \underline{u}(t) + G(t)\delta \underline{d}(t)$$

(2.4.11)

Some clarification about system names should be made at this point. Although this may seem a matter of semantics, it will eventually become clear why it is so important to

maintain these definitions. The system described in equation (2.4.1) will be referred to as the *nonlinear system*. The system described in equation (2.4.10) will be known as the *linearized system* or *linearized model*. Finally, the system in (2.4.11) will be known as the *linearized perturbation model*. Although the difference between (2.4.10) and (2.4.11) is simply a matter of algebra, the systems describe very different things. The linearized system (2.4.10) is an approximation of the nonlinear system (2.4.1) but the linearized perturbation model (2.4.11) describes the perturbed states.

There is a distinct advantage to working with linear instead of nonlinear systems. Linear systems can be put in state-space form which lends itself nicely to many modern methods of control system design.

2.4.1 The Linearized Perturbation Model

The A, B, and G matrices of equation (2.4.11) must be defined. This is done by taking a series of partial derivatives as expressed in (2.4.3) to (2.4.5). The results are below.

$$A(t) = \begin{bmatrix} 0 & 0 & 0 & 0 & A_{1,5} & A_{1,6} & A_{1,7} & 0 \\ 0 & 0 & 0 & 0 & A_{2,5} & A_{2,6} & A_{2,7} & 0 \\ 0 & 0 & 0 & 0 & A_{3,5} & A_{3,6} & A_{3,7} & 0 \\ 0 & 0 & 0 & 0 & 0 & 0 & 0 & 0 \\ A_{5,1} & 0 & 0 & 0 & 0 & 0 & 0 & 0 \\ 0 & A_{6,2} & 0 & 0 & A_{6,5} & 0 & 0 & 0 \\ A_{7,1} & 0 & A_{7,3} & 0 & A_{7,5} & A_{7,6} & 0 & 0 \\ A_{8,1} & A_{8,2} & 0 & A_{8,4} & A_{8,5} & A_{8,6} & A_{8,7} & 0 \end{bmatrix} \qquad (2.4.12)$$

$$B(t) = \begin{bmatrix} B_{1,1} & B_{1,2} & B_{1,3} & B_{1,4} \\ B_{2,1} & B_{2,2} & B_{2,3} & B_{2,4} \\ 0 & 0 & B_{3,3} & 0 \\ 0 & 0 & 0 & B_{4,4} \\ 0 & 0 & 0 & 0 \\ 0 & 0 & 0 & 0 \\ 0 & 0 & 0 & 0 \\ 0 & 0 & 0 & 0 \end{bmatrix} \qquad (2.4.13)$$

$$G(t) = \begin{bmatrix} G_{1,1} & G_{1,2} & 0 & G_{1,4} & G_{1,5} & G_{1,6} \\ G_{2,1} & G_{2,2} & 0 & G_{2,4} & G_{2,5} & G_{2,6} \\ 0 & 0 & 0 & G_{3,4} & G_{3,5} & 0 \\ 0 & 0 & 0 & 0 & 0 & 0 \\ 0 & 0 & 0 & 0 & 0 & G_{5,6} \\ 0 & 0 & 0 & G_{6,4} & G_{6,5} & 0 \\ 0 & 0 & 0 & G_{7,4} & G_{7,5} & 0 \\ 0 & 0 & 0 & G_{8,4} & G_{8,5} & 0 \end{bmatrix} \qquad (2.4.14)$$

All the non-zero elements in the matrices are labeled. The analytic expressions for many of these terms are highly complex, so they will not be presented here. They can be found in Appendix B.

The matrices above are intended to be evaluated at some nominal condition. Hence, by picking nominal values for the states, inputs, and disturbances, and evaluating the matrices at these points, the elements in A, B, and G become constants.

2.4.2 Testing the Linearized Perturbation Model

Once the A, B, and G matrices have been evaluated, the system is now of the following form.

$$\delta \underline{\dot{x}}(t) = A \delta \underline{x}(t) + B \delta \underline{u}(t) + G \delta \underline{d}(t) \qquad (2.4.15)$$

35

Here, A, B, and G are constants. It is important to note that, although this system is linear, it does not really represent the nonlinear system, but rather the perturbed system. Furthermore, even the linearized model (2.4.10) is not an exact representation of the nonlinear system due to the fact that all terms in the Taylor series expansion higher than first order were discarded. This leads to the question of how closely the linearized model approximates the nonlinear system. Care must be taken to ensure that any advantages in control that can be gained by working with a linear system are not offset by errors created by a poor approximation of the nonlinear system.

In evaluating the linearized perturbation model, the disturbance term will be neglected. The optimal controller that will be used will also not include a disturbance term. The evaluation of the perturbation model is done in the following manner. From a slight modification of the linearized model (2.4.10) above, and neglecting $\delta \underline{d}(t)$, this expression is obtained.

$$\underline{\dot{x}}(t) - \underline{\dot{x}}_N(t) = A\delta \underline{x}(t) + B\delta \underline{u}(t) \tag{2.4.16}$$

Substituting equations (2.4.1) and (2.4.9) for the left hand side leaves the following.

$$f\left\{\underline{x}(t), \underline{u}(t)\right\} - f\left\{\underline{x}_N(t), \underline{u}_N(t)\right\} = A\delta \underline{x}(t) + B\delta \underline{u}(t) \tag{2.4.17}$$

Finally, rearranging equations (2.4.6) and (2.4.7) and substituting into (2.4.17), the expression below is obtained.

$$f\left\{\underline{x}_N(t) + \delta \underline{x}(t), \underline{u}_N(t) + \delta \underline{u}(t)\right\} - f\left\{\underline{x}_N(t), \underline{u}_N(t)\right\} = A\delta \underline{x}(t) + B\delta \underline{u}(t) \tag{2.4.18}$$

The expression in (2.4.18) is the means by which the linearized perturbation model can be tested.

Several tests are performed below using Matlab computer software. A Simulink function, which implements the nonlinear system as per equation (2.3.4), is used. A small modification of this function allows for the same simplifications as were made in the linearized system, namely neglecting the Q_v term and approximating the inertia terms as in (2.3.7) - (2.3.10).

The procedure for testing is as follows. The nonlinear system is given a set of nominal initial conditions $\underline{x}_{NO}$ and constant inputs $\underline{u}_{NC}$. This system is numerically integrated and the system states $\underline{x}(t)$ are saved. In equation (2.4.18) this becomes the $f\{\underline{x}_N(t), \underline{u}_N(t)\}$ derivatives term. Next, a small perturbation is added to each of the nominal conditions. Again, the nonlinear system is numerically integrated with these new conditions and this becomes the $f\{\underline{x}_N(t) + \underline{\delta x}(t), \underline{u}_N(t) + \underline{\delta u}(t)\}$ derivatives term. These two terms are differenced and the results plotted. For the other side of equation (2.4.18), the A and B matrices in the linearized perturbation model are evaluated at the nominal conditions $\underline{x}_{NO}$ and $\underline{u}_{NC}$. This system is then given the perturbed initial conditions and inputs $\underline{\delta x}_O, \underline{\delta u}_C$ and is numerically integrated. The system states are plotted on the same graph as the nonlinear results. As equation (2.4.18) describes, the results should be equal for arbitrarily small perturbations $\underline{\delta x}(t)$ and $\underline{\delta u}(t)$.

From equation (2.4.18) above, it is also evident that, in the special case that the nominal states and inputs are all zero, the expression reduces to the following.

$$f\{\underline{x}(t), \underline{u}(t)\} = f\{\underline{\delta x}(t), \underline{\delta u}(t)\} = A\underline{\delta x}(t) + B\underline{\delta u}(t) \qquad (2.4.19)$$

This means that with zero nominal conditions, the nonlinear system can be directly compared to the linearized perturbation model. This is the first test that is performed.

The eight states are shown on four separate graphs for ease of viewing. For this case, the following conditions apply.

$$\underline{x}_{NO} = 0$$

$$\underline{u}_{NC} = 0$$

$$\underline{\delta x}_O = 0$$

$$\underline{\delta u}_C = \begin{bmatrix} 0.7005 & 0.3362 & 0.1397 & 0.1321 \end{bmatrix} ft \cdot lbs$$
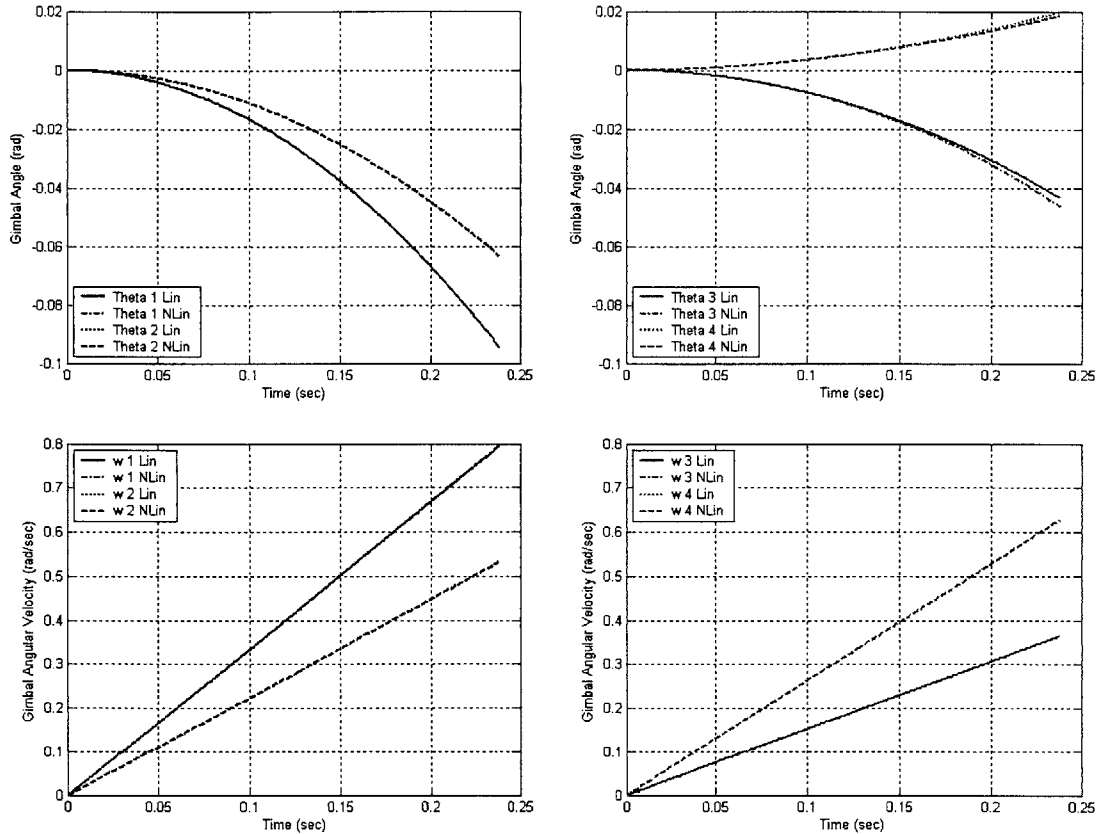
Figure 2.4.1 - Gimbal angles and velocities for zero nominal conditions.

The legend on each graph identifies the lines representing the linearized perturbation model states as well as those of the nonlinear states. The input torque values are small fractions of the full motor torque capacities for each of the motors and are used to create motion in the system. This case represents a relatively benign condition and is used primarily to test the computer code representing the linearized perturbation model. The perturbation states move in the correct direction, generally follow the nonlinear states,

and gradually deviate from the nonlinear states over time. This is as expected and is a good indication that the computer model is correct.

Aside from simply evaluating the computer code, the testing of the linearized perturbation model can yield a second piece of information. It is important to know over what period of time the linearized perturbation model remains an accurate representation of the nonlinear system. The linearized perturbation model in (2.4.18) is only valid over a range where the states and inputs are close to the nominal conditions. To determine the size of this range, the following procedure is followed.

For a particular instant in time, the difference between the nonlinear states and the perturbations states is determined. Each element in this error vector is then divided by the value of the corresponding nonlinear state at the same instant in time to produce a relative error vector. This relative error vector is then divided into two vectors, one for angles and one for inertial rates. The norm of each of these vectors is determined and as soon as either the angle or rate norms reach a value above 0.1, or ten percent, the simulation is halted. Thus, as shown in Figure 2.4.1, the perturbation model with the conditions listed above will maintain the perturbation states within ten percent of the nonlinear states for a period of 0.238 seconds.

Obviously, the condition where the nominal states and inputs are all zero is an unlikely idealization. For this reason, the linearized perturbation model is tested at other, more strenuous, conditions as well. First, the case where the nominal and perturbed inertial rates are nonzero is considered.

The missile motion is limited to a maximum angular rate of 45 degrees per second as discussed in section 2.1. Thus, a conservative estimate for the maximum inertial rates of the gimbals is also 45 degrees per second. It is obvious that the larger the gimbal inertial rates, the faster the linearized states will diverge from the nonlinear states simply due to the fact that the gimbal system is moving more rapidly. Therefore, the most strenuous condition occurs when the nominal inertial rates are equal to 45 degrees per second.

Testing above these limits will not yield useful results as the system will never be subjected to rates larger than these values. Also, as seen below, the perturbed conditions are chosen to be five percent of the nominal conditions, a physically realistic value.

$$\underline{x}_{NO} = \begin{bmatrix} 45 & 45 & 45 & 45 & 0 & 0 & 0 & 0 \end{bmatrix}$$

$$\underline{u}_{NC} = \begin{bmatrix} 0 & 0 & 0 & 0 \end{bmatrix}$$

$$\underline{\delta x}_O = \begin{bmatrix} 2.25 & 2.25 & 2.25 & 2.25 & 0 & 0 & 0 & 0 \end{bmatrix}$$

$$\underline{\delta u}_C = \begin{bmatrix} 0.7005 & 0.3362 & 0.1397 & 0.1321 \end{bmatrix}$$

Here, the units are degrees, degrees per second, and foot pounds as appropriate.
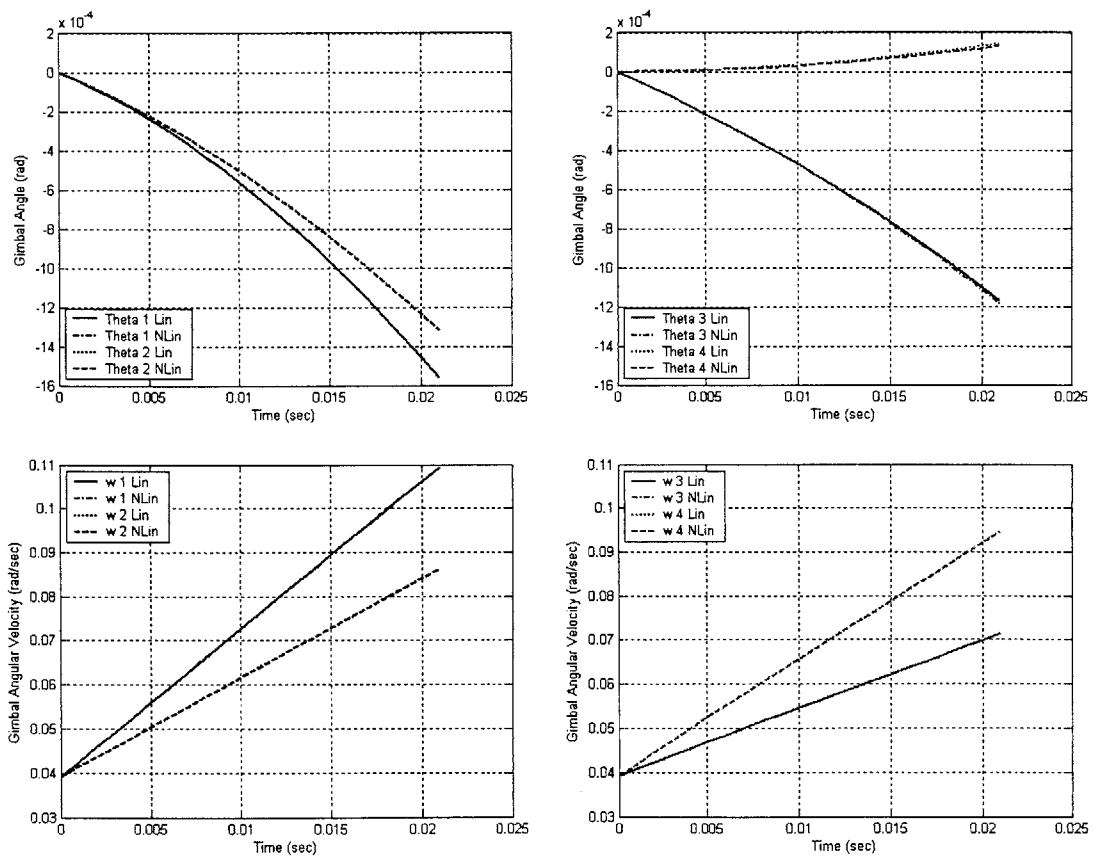
Figure 2.4.2 - Gimbal angles and velocities for maximum angular velocity conditions.

40

Again, the perturbation model generally follows the nonlinear model, and degrades over time. However, under these conditions, the linearized perturbation model degrades an order of magnitude more quickly as the ten percent limit of the vector norms is reached in just 0.021 seconds as shown in Figure 2.4.2.

Finally, an attempt is made at choosing a worst-case scenario for the nominal and perturbed gimbal angles. In the case of the inertial rates it is intuitively clear that the higher the rate, the more quickly the states will diverge, hence the maximum rate will yield the maximum error. However, as can be seen in Appendix B, there is a good deal of coupling with regard to the gimbal angles. Fortunately, with zero case motion, it can be easily seen that θ_1 and θ_4 do not appear in any of the terms in the A or B matrices and therefore, since the nominal values will not affect the dynamics, they can remain zero.

To choose a worst-case nominal θ_2 and θ_3, a series of more than 1200 simulations is performed. First, the angles are discretized over their entire range, $-\pi \leq \theta_i \leq \pi$. Then, the simulator varies the two angles independently and simulates every possible combination of angles. Finally, the angle combination producing the shortest range in which the error remained within the ten percent limit, as discussed above, is taken to be the worst case.

The perturbed conditions are taken to be a fixed value of eight degrees. As with the inertial rates, it can be easily seen that for larger perturbed conditions, the states will diverge more quickly. The value of eight degrees, therefore, represents an approximation of the physical limits of the system.

Thus, for the final case, the following conditions apply.

$$\underline{x}_{NO} = \begin{bmatrix} 45 & 45 & 45 & 45 & 0 & -60 & -70 & 0 \end{bmatrix}$$

$$\underline{u}_{NC} = \begin{bmatrix} 0 & 0 & 0 & 0 \end{bmatrix}$$

$$\underline{\delta x}_O = \begin{bmatrix} 2.25 & 2.25 & 2.25 & 2.25 & 8 & 8 & 8 & 8 \end{bmatrix}$$

$$\underline{\delta u}_C = \begin{bmatrix} 0.7005 & 0.3362 & 0.1397 & 0.1321 \end{bmatrix}$$

As before, the units are degrees, degrees per second, and foot pounds.
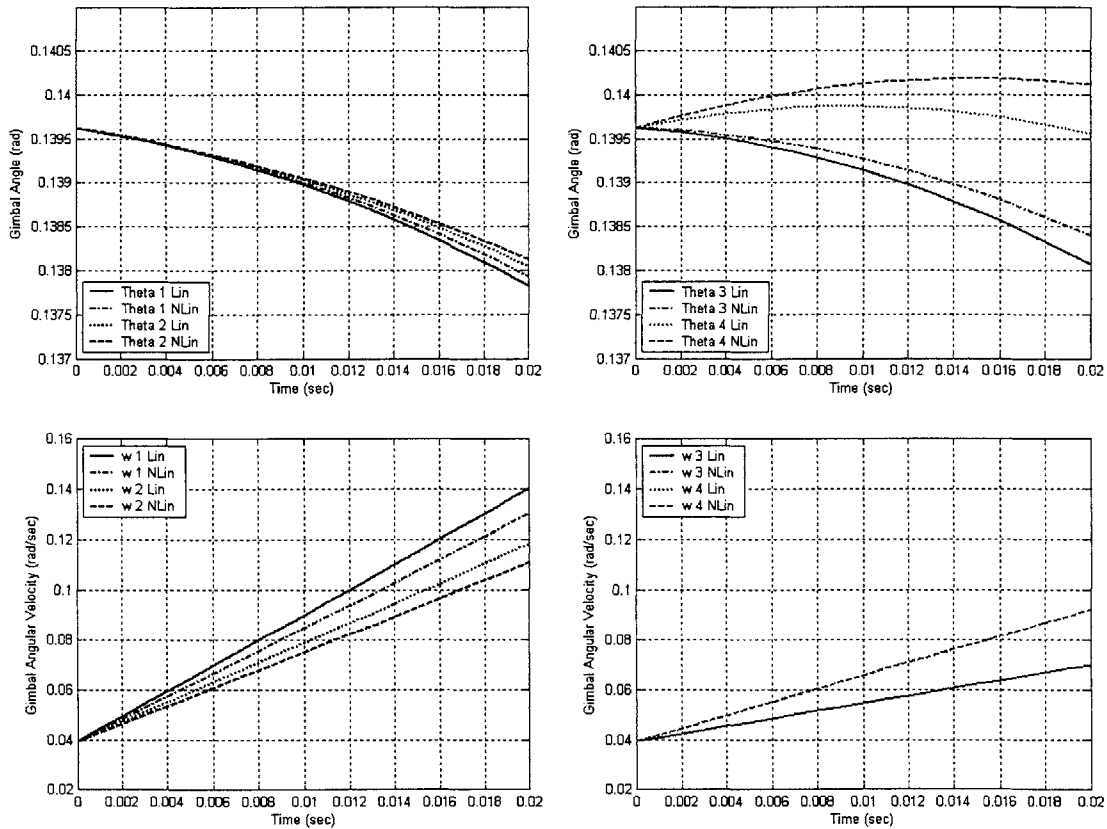
Figure 2.4.3 - Gimbal angles and velocities for worst case gimbal angle and angular velocity conditions.

The states diverge more quickly and in this case the ten percent limit is reached in a marginally faster 0.020 seconds. Obviously the searching method herein employed, while quick and simple, cannot find a true global minimum and hence this value cannot be taken as an absolute minimum. However, there is high confidence that the true minimum would be on the order of the case given in Figure 2.4.3.

2.4.3 Updating the Linearized Perturbation Simulation

The immediate problem with the linearized perturbation model is the short timeframe over which it is valid. An attempt is made at lengthening this time period by updating the linearized perturbation model with new nominal and perturbed conditions at some specified rate. In other words, the A and B matrices are reevaluated and new initial conditions and inputs are used. It is shown below that, with these updates, the linearized perturbation model performed excellently.

Taking the same nominal and perturbed conditions as in Figure 2.4.3, the following results are obtained.
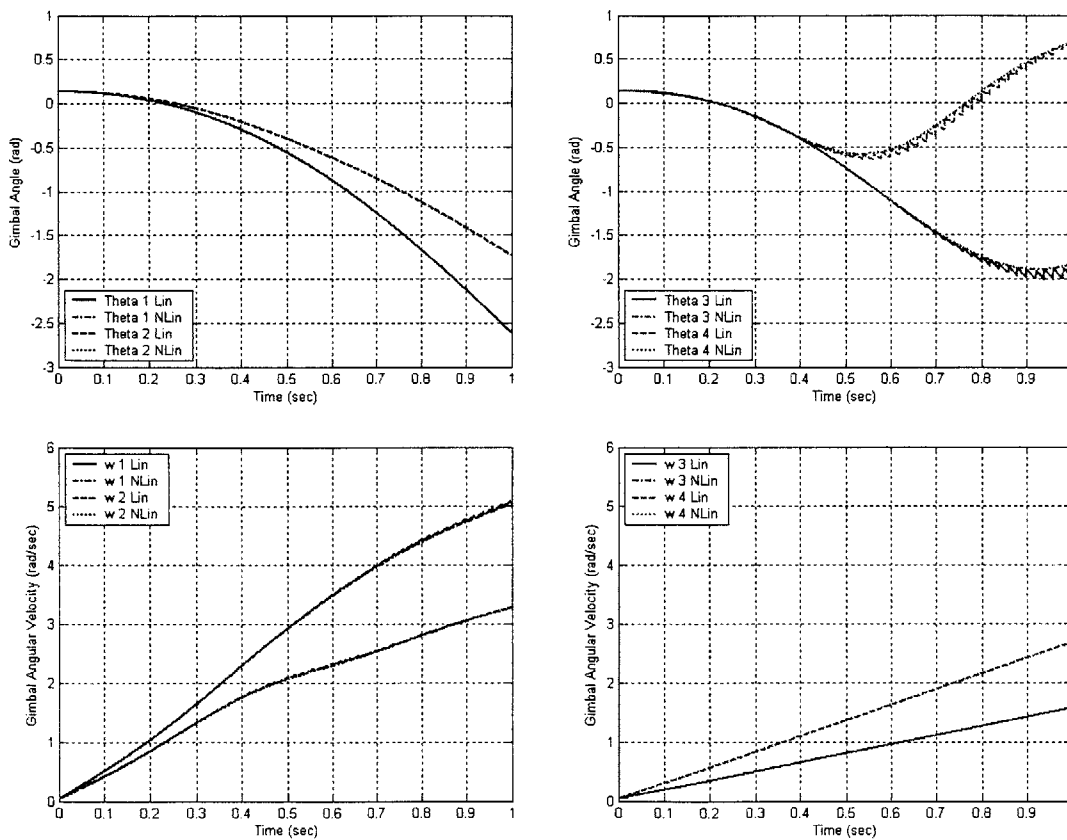
Figure 2.4.4 - Gimbal angles and velocities with nominal condition updates.

The linearized perturbation model is updated at 50 Hz. This represents a period of 0.020 seconds which is equivalent to the range obtained in the worst case scenario of Figure 2.4.3. As can be seen in Figure 2.4.4, the linearized perturbation states and the nonlinear states never vary by more than ten percent over the entire one second interval. This represents a dramatic improvement over the previous interval of just 0.020 seconds. Although there is very close agreement between the nonlinear and linearized systems in this case, it should be emphasized that the evaluation is not a real-time operation. In other words, the nonlinear system is numerically integrated twice as before, once with the nominal conditions and a second time with the nominal plus the perturbed conditions. All the data are saved and then sampled at 50 Hz. The nominal conditions data set is used to reevaluate the A and B matrices and the difference between the two data sets is used as the perturbed conditions for the linearized perturbation model. Obviously, this could only work in a post-processing environment and thus, the results here do not suggest an on-line computed metric of linearization quality.

Chapter 3

A Classical Control Approach

3.1 Platform Control

With the equations of motion adequately expressed, controller design can commence. A design using techniques of classical control theory is implemented as a benchmark against which an optimal control design will be compared.

Before discussing the design of the controller, it is important to understand the eventual goal of platform control. As discussed in section 1.1, the primary role of the platform controller is to null the sensed gyro errors by applying torque to the gimbals, hence stabilizing the platform in inertial space and preventing large platform motions. At first it may appear that only three gimbals are necessary to perform this task, one for each orthogonal direction. However, three gimbals are inadequate. Take, for example, a case where all gimbal torque motor axes lie in the same plane. In this configuration, it is not possible to move the platform about an axis perpendicular to this plane, and hence gyro errors in this direction could not be corrected. This uncontrollable gimbal configuration is called gimbal lock.

Historically, early inertial systems utilized three-gimbal configurations, but much care had to be taken to avoid case trajectories leading to gimbal lock [12]. This restriction gave rise to a desire to use a fourth, or redundant gimbal. The advantage gained is an extra degree-of-freedom to maintain controllability in cases where a three gimbal system

would be uncontrollable. However, the disadvantage is an increase in complexity of the platform controller.

It should be apparent that simply adding another gimbal is not enough to guarantee the system will not reach gimbal lock. Now, instead of having three torque motor axes lie in a single plane, by aligning all four axes in a plane, a direction perpendicular to the plane will be uncontrollable. For the four gimbal system pictured in Figure 2.1.1, this occurs when both of the following conditions are met.

$$\theta_2 = \frac{\pi}{2} + n \cdot \pi \quad (n = \ldots, -2, -1, 0, 1, 2, \ldots)$$ (3.1.1)

$$\theta_3 = \frac{\pi}{2} + m \cdot \pi \quad (m = \ldots, -2, -1, 0, 1, 2, \ldots)$$ (3.1.2)

Still, the advantage of the four gimbal system over the three gimbal system is that with four gimbals, these instances of gimbal lock can be prevented for a much larger class of input motions.

Although it is theoretically possible to avoid gimbal lock for a larger class of input motions with a four gimbal system, it is not immediately clear how this is best accomplished. Essentially, the platform controller of a four gimbal system has two tasks. First, it must stabilize the platform in inertial space by nulling gyro errors and second, it must arrange the gimbals in such a way that they avoid gimbal lock. With two tasks at hand the question becomes how much motor torque capacity should be spent on avoiding gimbal lock versus nulling gyro errors. Utilizing too much torque for gimbal lock avoidance could result in inadequate torque for nulling the gyro errors, leading to large platform rotation transients. However, too little torque dedicated to gimbal lock avoidance could result in a loss of system controllability, and hence equally large platform transients.

Accordingly, an explanation of the control design proceeds as follows. First, a single-axis compensator design is presented for one gimbal and one gyro error component. Then, this design is expanded to include all four gimbals and three gyro errors. Finally, a Gimbal Lock Avoidance or GLA controller is added to enable the dual goals presented above.

3.2 Gyro Error Compensation

3.2.1 A Single-Axis Gyro Controller

The goal for the single-axis compensator is to design a controller for a single gimbal and gyro error with an acceptable response and subsequently map that response into the three gyro loops of the four gimbal system. The design begins with the platform gimbal only, as it is dynamically uncoupled from the rest of the system. As can be seen previously in Figure 2.3.1, the independent axis of rotation, or x-axis, of the platform gimbal corresponds directly to the W gyro error. Hence, any and all error sensed by the W gyro must be corrected by the platform gimbal torque motor and, in addition, the only error which the platform gimbal motor can affect is the W error.

A block diagram of the single-axis gyro error loop is presented below.
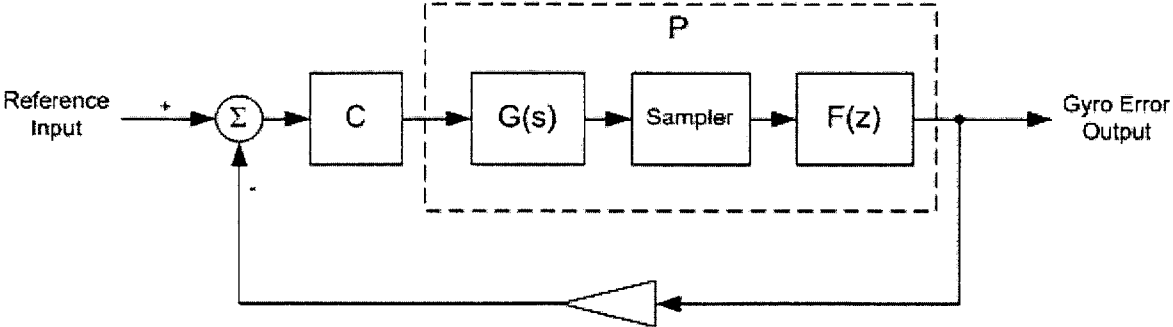
Figure 3.2.1 – The single-axis gyro control loop.

Above in Figure 3.2.1, the plant P includes the torque motor acting on the platform gimbal. It takes a torque command from the compensator, C, and outputs the resulting gyro error. Thus, the plant consists of the continuous gimbal dynamics, *G(s)*, and the discrete gyro quantization and filters, *F(z)*. A sampler transitions from the continuous plant to the discrete filters.

The gimbal dynamics are quite simple, consisting of a double integrator with a small back-emf component from the torque motor as follows.

$$G(s) = \frac{K_t/V \cdot 1/J}{s(s + K_t/V \cdot K_y/J)} \tag{3.2.1}$$

Equation (3.2.1) can be shown in block diagram form as below.
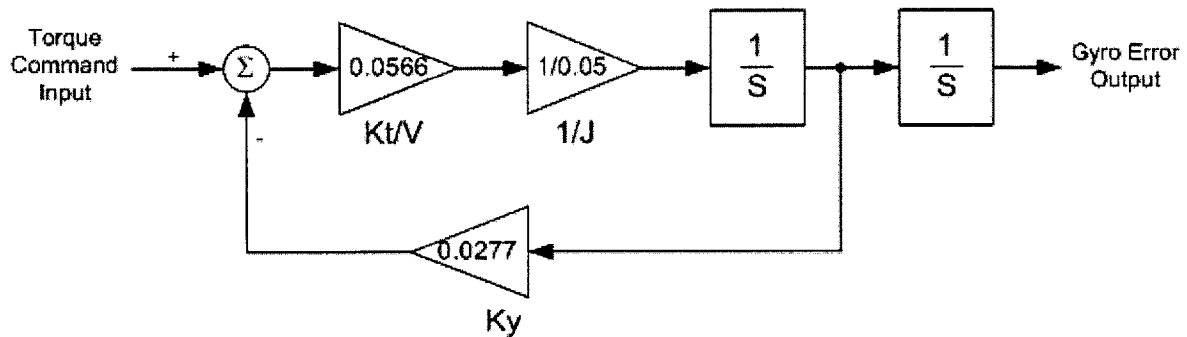
Figure 3.2.2 - Block diagram of the platform gimbal dynamics.

In Figure 3.2.2, the output of the dynamics model is the gyro error. The roots of (3.2.1), or open loop poles of the plant, are at zero and -0.0314.

The plant P in Figure 3.2.1 also includes the gyro quantization and filtering as outlined in section 2.2. Thus, a filtered gyro error signal with a range of ± 10,000 bits is obtained. The controller must be designed to keep the gyro error appropriately within this range.

In Figure 3.2.1, the gyro error signal is fed back to the compensator C. The gain in the feedback path converts the gyro error signal from bits to radians. Note that no resolver is

present for the single-axis gyro controller. This is because the controller does not need a measure of the gimbal angle as the W gyro error corresponds directly to platform gimbal angle in the single-axis case.

In Figure 3.2.1 above, a reference input is added to the error signal. This is to allow for the tracking of a specific gyro error command, such as a step or ramp input. This tracking functionality is solely for design and evaluation of the single-axis compensator. In the eventual implementation of the multi-axis controller, the general goal will be to regulate all gyro errors to zero.

Table 3-1 Single-axis gyro error compensator performance requirements

Requirement	Value
Overshoot	$< 40\%$
Settling time (within 5% final value)	< 0.2 sec
Steady-state error for a ramp input	0
Closed-loop Bandwidth	> 100 rad/sec

Table 3-1 gives the performance requirements for the gyro error compensator. In designing the compensator below, optimum gains are chosen so that the single-axis gyro loop meets the performance requirements.

The compensator C takes the gyro error and computes a torque input to the plant P. Through experimentation, it has been found that an operating frequency of 300 Hz for the discrete compensator produces acceptable results [4]. The compensation equation is as follows.

$$C(z) = 22.2308 \cdot \left[\frac{z - 0.9532}{z - 0.4448} + 0.002 \frac{z}{z - 1} \right] \qquad (3.2.2)$$

As a block diagram, the compensator is implemented as follows.
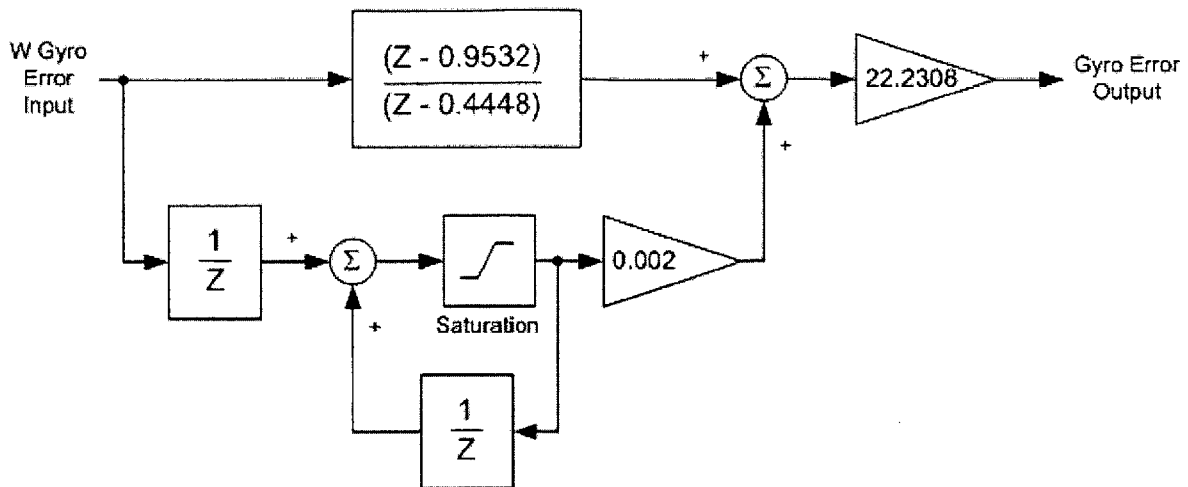
Figure 3.2.3 - Block diagram of the *W* gyro error compensator.

As can be seen in (3.2.2) and Figure 3.2.3, the compensator includes two pieces. The first is a filter which serves to stabilize the single-axis control loop and provide the desired overshoot and damping characteristics. The second is an integrator to insure zero steady-state error for ramp inputs. In addition, the integrator helps to counteract friction effects which, while not modeled by this plant, would be present in any hardware. The response of the single-axis gyro loop can be seen in the following plots.
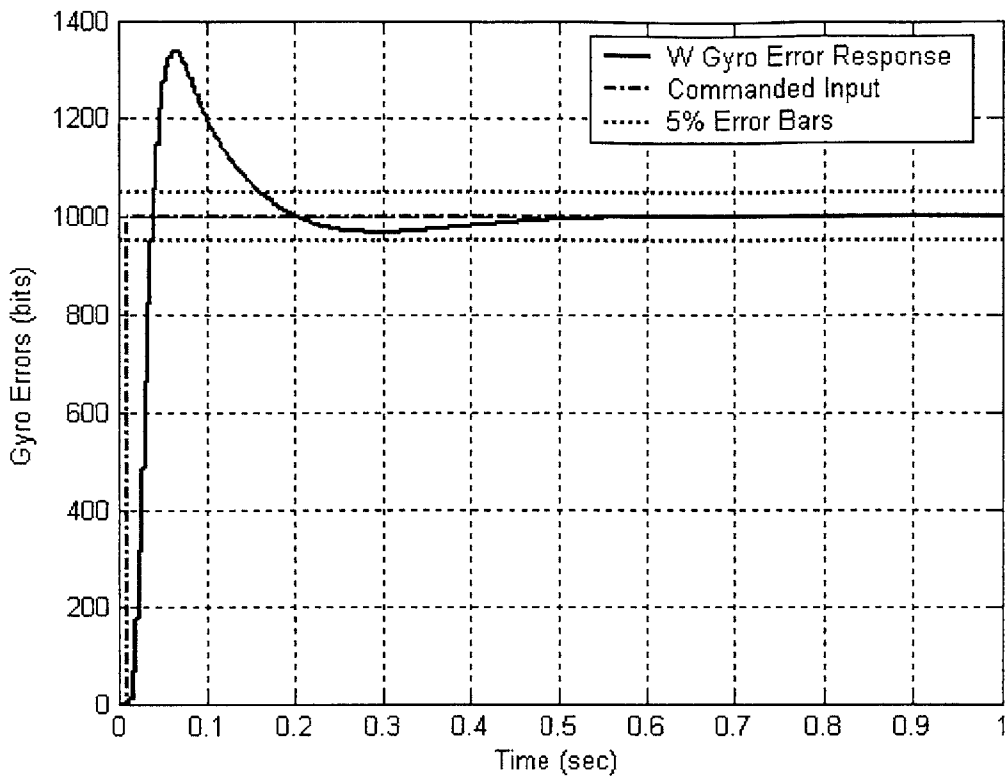
Figure 3.2.4 - A 1000 bit step response for the single-axis W gyro controller.

In Figure 3.2.4 above, the gyro errors are given in bits, so this 1000 bit step response is equivalent to a 0.00175 radian response. It can be seen from the figure that both the overshoot and settling time are well below the requirements outlined in Table 3-1 above.
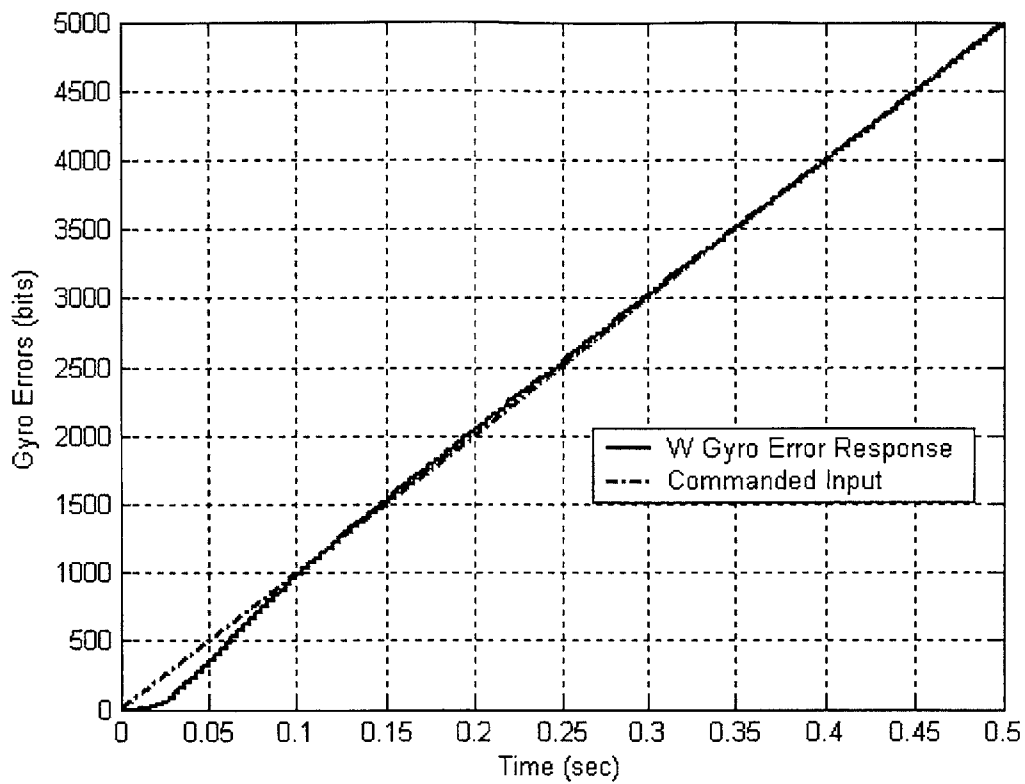
Figure 3.2.5 - A ramp response for the single-axis *W* gyro controller.

Figure 3.2.5 shows the response to a ramp input. Here, it is shown that by including the integrator, zero steady-state error for the ramp input is achieved.
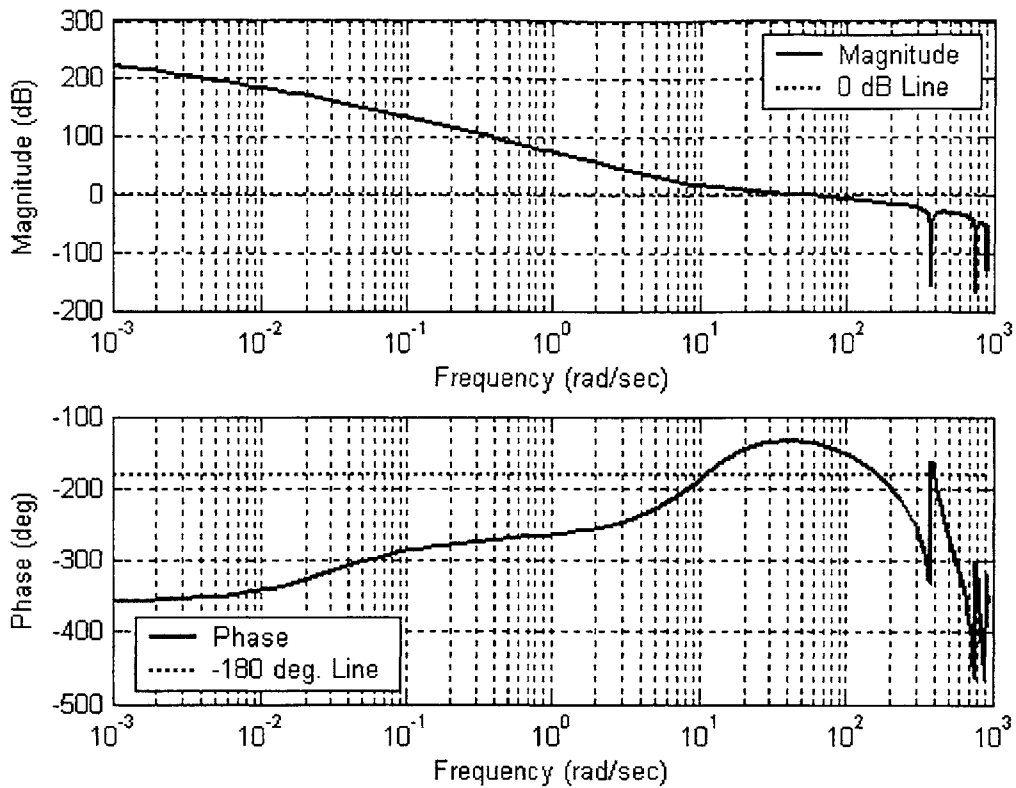
Figure 3.2.6 - An open-loop frequency response for the single-axis *W* gyro controller.

Figure 3.2.6 shows the open-loop frequency response for the single-axis controller. The gain margin at -180 degrees of phase is 11.5 dB and the phase margin at 0 dB is 45.6 degrees.
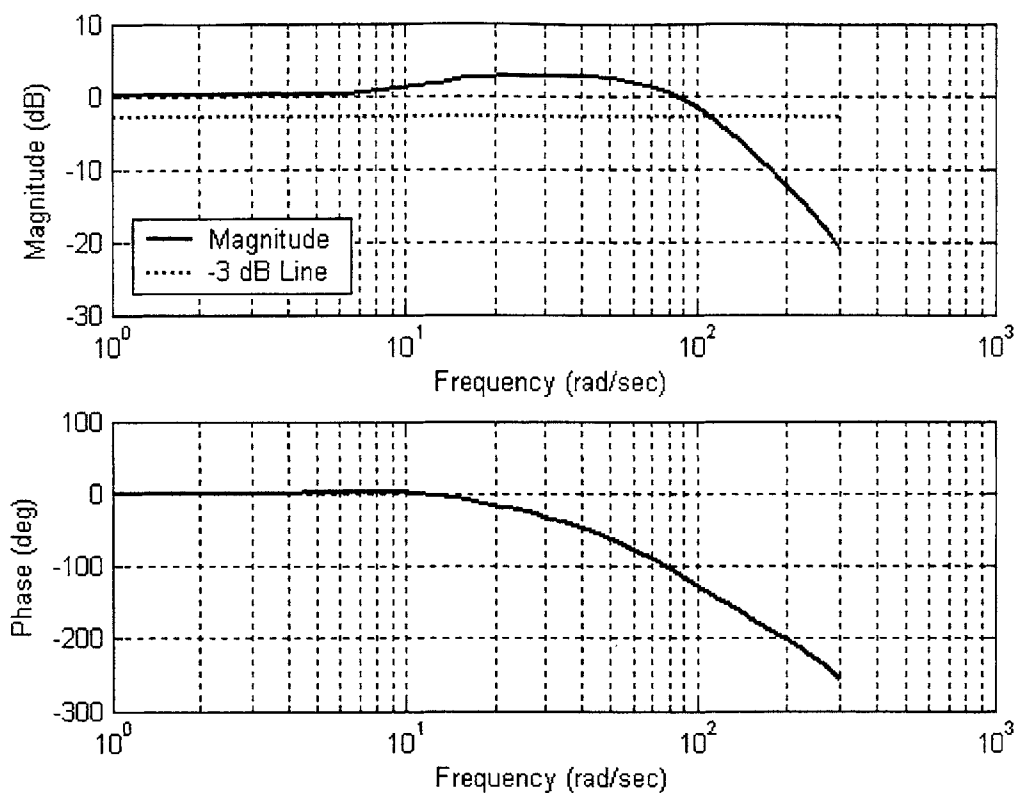
Figure 3.2.7 - A closed-loop frequency response for the single-axis *W* gyro controller.

Finally, Figure 3.2.7 shows the closed-loop frequency response for the single-axis controller. Here, the closed-loop bandwidth is 111 radians per second, well above the requirement in Table 3-1.

3.2.2 A Multi-Axis Gyro Controller

The next step in designing a platform controller is to expand the compensation from the single-axis gyro loop to three gyro loops. The following block diagram depicts the multi-axis gyro control loop.
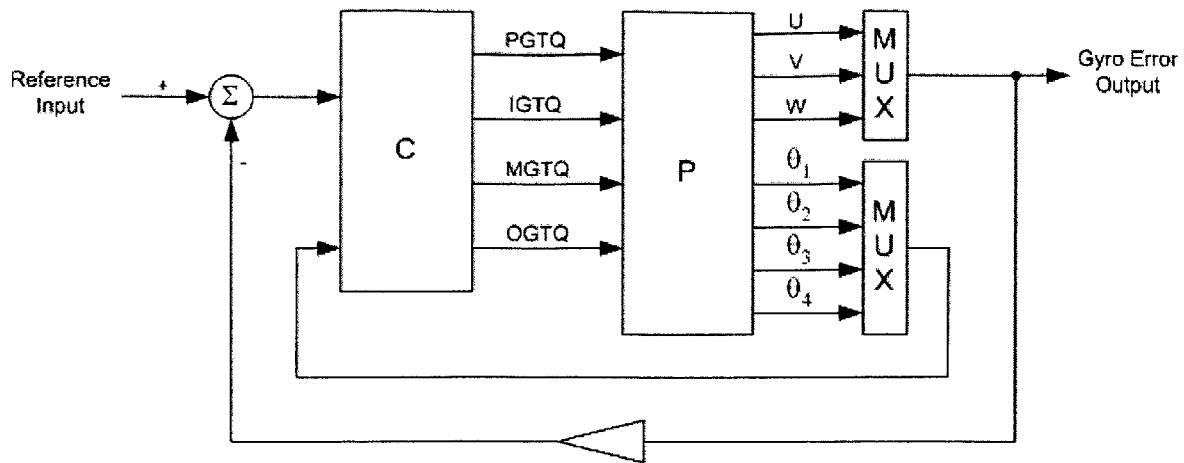
Figure 3.2.8 - The multi-axis gyro control loop.

In Figure 3.2.8 above, the plant P contains the four gimbal non-linear dynamics outlined in (2.3.14) and (2.3.15). Also, the quantization and filtering is present, just as in the single-axis plant. In addition, the plant P models the resolvers described in section 2.2. Thus, the plant takes four torque command inputs, one for each gimbal torque motor, and reports three gyro errors, U, V, and W, from the gyro sensors, as well as four gimbal angles from the resolvers.

As in the single-axis controller, a reference signal is differenced from the gyro errors to enable responses to commanded inputs. This reference signal is only used for testing, as the controller will eventually regulate all gyro errors to zero.

The compensator C in Figure 3.2.8 uses the three gyro errors and three of the angles to compute four torque commands. Following is a block diagram overview of this compensator.
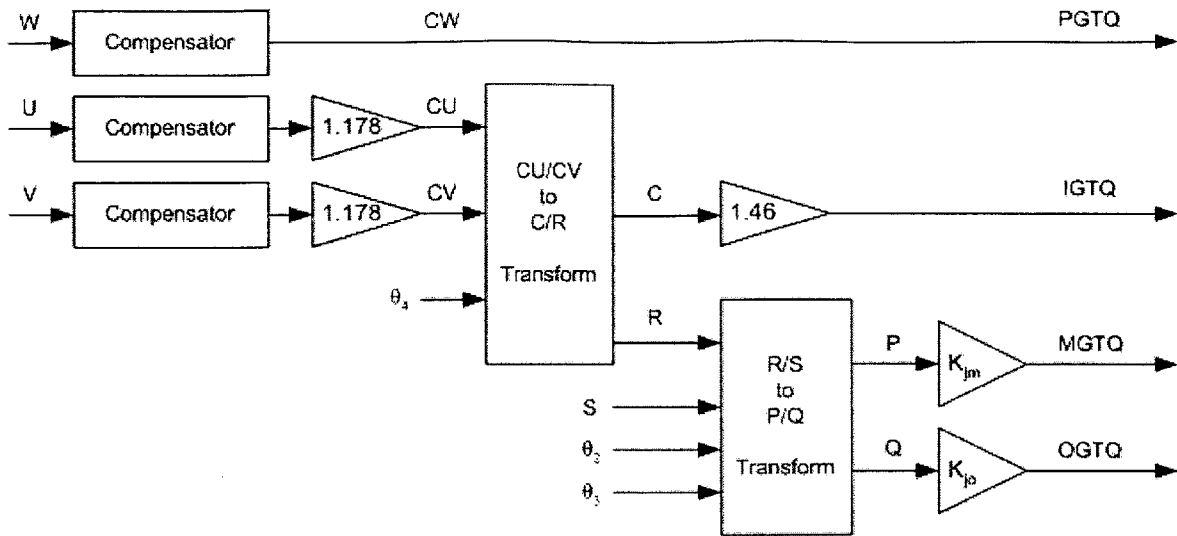
Figure 3.2.9 - Block diagram of the multi-axis gyro error compensator.

The controller in Figure 3.2.9 above has two added complexities beyond the single-axis controller in section 3.2.1. First, the multi-axis controller must map three gyro errors onto four gimbal axes. It should be apparent from Figure 2.1.1 that, depending on gimbal configuration, the gyro errors map to different gimbal axes and hence need to be corrected by different torque motors. Second, it is desirable that the multi-axis controller maintain a uniform response regardless of the axis of gyro errors or the configuration of the gimbals. This allows for easy evaluation of controller performance.

In order to enable the two goals presented above, the following additions are made to the single-axis compensator. Some of these additions are static gains, and others are dynamic gains.

As explained in section 3.2.1 above, the W gyro error is entirely controlled by the platform gimbal and cannot be directly controlled by any of the other gimbals. Thus, the same compensation which was used in the single-axis controller for the W gyro error, as shown in Figure 3.2.3, is also used in the multi-axis controller. In addition, the U and V gyro errors employ the same compensation as the W gyro error, with one addition. The U and V gyro errors are controlled by the inner, middle, or outer gimbals, depending upon gimbal configuration. As the inner, middle, and outer gimbals have different inertias, as

56

well as different torque motors, it is necessary to increase the gain in the U and V gyro error compensators by the following factor.

$$\frac{J_{eff}^{PG} / K_t^{PG}}{J_{eff}^{MG} / K_t^{MG}} = 1.178 \tag{3.2.3}$$

The gain in (3.2.3) above is a static gain which corrects for the larger inertias and torque constants in the middle gimbal, thus helping to maintain a uniform response by the compensators regardless of which axis reports a nonzero gyro error. The effective inertias are computed at all-attitude zero configuration and are given in (2.2.6) and (2.2.8).

At this point in the controller in Figure 3.2.9 there are three compensated errors, CU, CV, and CW, which must be mapped to four torque commands. As has already been discussed, the CW compensated error is mapped directly to the platform gimbal torque, $PGTQ$. This leaves two compensated errors to be mapped to three gimbal torques.

To accomplish this, a dynamic transformation of the CU and CV compensated errors is performed. It is desired to impart angular accelerations to the gimbals using the torque motors. Thus, it is easier to think of the transformation in terms of accelerations, rather than torques. To this end, from (A.18) and (A.20) and neglecting the $\overline{Q}_c$ term as before in section 2.3, the following is obtained.

$$\begin{bmatrix} \dot{\varpi}_{4y} \\ \dot{\varpi}_{4z} \end{bmatrix} = \begin{bmatrix} c\theta_2 s\theta_3 s\theta_4 & -c\theta_3 s\theta_4 & c\theta_4 & 0 \\ -c\theta_2 s\theta_3 c\theta_4 & c\theta_3 c\theta_4 & s\theta_4 & 0 \end{bmatrix} \cdot \begin{bmatrix} \dot{\varpi}_{1x} \\ \dot{\varpi}_{2x} \\ \dot{\varpi}_{3x} \\ \dot{\varpi}_{4x} \end{bmatrix} \tag{3.2.4}$$

In (3.2.4) above, understanding the desired accelerations to be equivalent to the torques applied by the motors, the following definition is made.

$$\begin{bmatrix} CU \\ CV \end{bmatrix} = \begin{bmatrix} \dot{\varpi}_{4y} \\ \dot{\varpi}_{4z} \end{bmatrix}$$ (3.2.5)

Equation (3.2.4) can be arranged into the following.

$$\begin{bmatrix} CU \\ CV \end{bmatrix} = \begin{bmatrix} c\theta_4 & -s\theta_4 \\ s\theta_4 & c\theta_4 \end{bmatrix} \cdot \begin{bmatrix} \dot{\varpi}_{3x} \\ c\theta_3\dot{\varpi}_{2x} - c\theta_2 s\theta_3\dot{\varpi}_{1x} \end{bmatrix}$$ (3.2.6)

In (3.2.6), the following compensated errors are defined below.

$$\begin{bmatrix} C \\ R \end{bmatrix} = \begin{bmatrix} \dot{\varpi}_{3x} \\ c\theta_3\dot{\varpi}_{2x} - c\theta_2 s\theta_3\dot{\varpi}_{1x} \end{bmatrix}$$ (3.2.7)

Now, substituting (3.2.7) into (3.2.6) and solving for C and R by taking an inverse, the following is obtained.

$$\begin{bmatrix} C \\ R \end{bmatrix} = \begin{bmatrix} c\theta_4 & s\theta_4 \\ -s\theta_4 & c\theta_4 \end{bmatrix} \cdot \begin{bmatrix} CU \\ CV \end{bmatrix}$$ (3.2.8)

The transformation in (3.2.8) above is referenced in Figure 3.2.9. The geometric interpretation of (3.2.8) can be observed from Figure 2.1.1. With a platform angle of 0 degrees, the C compensated error is equivalent to CU and R is equivalent to CV. With a platform angle of 90 degrees, the C compensated error is equivalent to CV and R is equivalent to $-CV$. In between 0 and 90 degrees, C and R are combinations of CU and CV.

With the transformation accomplished, the C compensated error is now equivalent to the inner gimbal torque $IGTQ$. However, one further correction is needed. From the gain in (3.2.3) above, the CU and CV compensated errors have been corrected for the effective inertia and torque constant of the middle gimbal at all-attitude zero. The C compensated

error must now be further corrected for the inner inertia and torque constant. This is accomplished with the following gain in the C compensated error path.

$$\frac{J_{eff}^{IG}/K_t^{IG}}{J_{eff}^{MG}/K_t^{MG}} = 1.46 \qquad (3.2.9)$$

The static gain in (3.2.9) above multiplies the C compensated error yielding the inner gimbal torque command $IGTQ$. The effective inertias are calculated from (2.2.6) and (2.2.7).

With platform and inner torque commands calculated, the final step for the platform controller is to map the R compensated gyro error to the outer and middle torque commands $OGTQ$ and $MGTQ$. At this point it should also be mentioned that, aside from the R compensated gyro error, in Figure 3.2.9 above there is also a redundant compensated error S. This error comes by way of the GLA controller and must be included in the outer and middle torque commands. The calculation of this redundant compensated error will be discussed subsequently in section 3.3.

In order to ensure the GLA commands do not interfere with maintaining zero gyro errors, orthogonality between the R compensated error and the S redundant error must be maintained. This is accomplished using the following dynamic transformation. In (3.2.7) above, the following definition of R is made.

$$R = c\theta_3 \dot{\omega}_{2x} - c\theta_2 s\theta_3 \dot{\omega}_{1x} \qquad (3.2.10)$$

Again, understanding the accelerations to be equivalent to the commanded torques, the following terms from (3.2.10) are defined.

$$\begin{bmatrix} P \\ Q \end{bmatrix} = \begin{bmatrix} \dot{\omega}_{2x} \\ \dot{\omega}_{1x} \end{bmatrix} \qquad (3.2.11)$$

In order to be in the null space of R, the S redundant error is given in the definition below, which also includes the R compensated error.

$$\begin{bmatrix} R \\ S \end{bmatrix} = \begin{bmatrix} c\theta_3 & -c\theta_2 s\theta_3 \\ c\theta_2 s\theta_3 & c\theta_3 \end{bmatrix} \cdot \begin{bmatrix} P \\ Q \end{bmatrix} \qquad (3.2.12)$$

As before, the solution for P and Q is found by taking an inverse, yielding the following result.

$$\begin{bmatrix} P \\ Q \end{bmatrix} = \frac{1}{c\theta_3^2 + c\theta_2^2 s\theta_3^2} \cdot \begin{bmatrix} c\theta_3 & c\theta_2 s\theta_3 \\ -c\theta_2 s\theta_3 & c\theta_3 \end{bmatrix} \cdot \begin{bmatrix} R \\ S \end{bmatrix} \qquad (3.2.13)$$

For simplicity, the first term in (3.2.13) is neglected. As will be shown below, the neglecting of this gain term has only minor implications. Thus, the following is the transformation shown in Figure 3.2.9.

$$\begin{bmatrix} P \\ Q \end{bmatrix} = \begin{bmatrix} c\theta_3 & c\theta_2 s\theta_3 \\ -c\theta_2 s\theta_3 & c\theta_3 \end{bmatrix} \cdot \begin{bmatrix} R \\ S \end{bmatrix} \qquad (3.2.14)$$

Here in (3.2.14), P and Q are functions of the middle and inner gimbal angles and must be corrected for gimbal inertias.

Thus far, only the effective inertias at all-attitude zero have been considered. However, in calculating the outer and middle torque commands, the corrections for the inertias will be dynamic, utilizing the current gimbal configuration. This dynamic correction is necessary due to significant non-zero, off-diagonal inertia terms in the system mass matrix of (2.3.6). The dynamic correction gains are as follows.

$$K_{jm} = \frac{J_{xx}^2 + J_{yy}^3 + J_{zz}^4 \cdot (c\theta_3)^2}{J_{eff}^{MG}} \qquad (3.2.15)$$

$$K_{jo} = \frac{K_t^{MG}}{K_t^{OG}} \cdot \frac{J_{xx}^1 + J_{yy}^2 + J_{zz}^3 \cdot (c\theta_2)^2 + J_{xx}^4 \cdot (c\theta_2)^2 \cdot (s\theta_3)^2}{J_{eff}^{MG}}$$ (3.2.16)

Again, the effective inertia is given in (2.2.6). The compensated errors P and Q are multiplied by the dynamic gains in (3.2.15) and (3.2.16) yielding the outer and middle torque commands.

Following are results of step inputs for the multi-axis gyro controller.
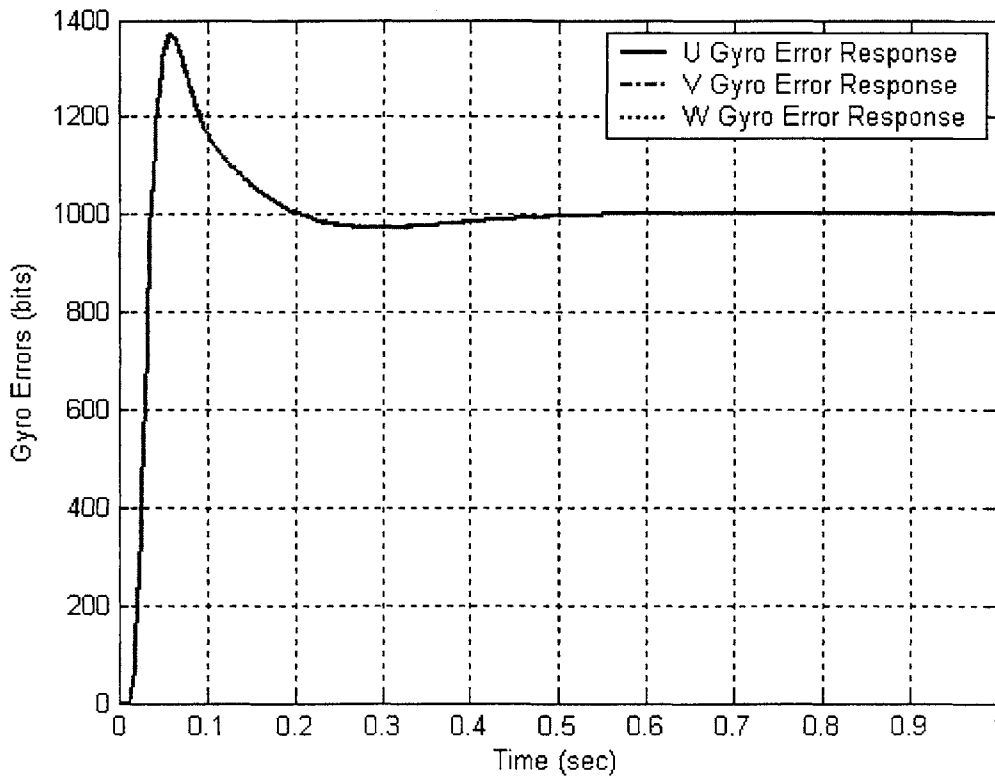
Figure 3.2.10 - A 1000 bit step response for the multi-axis gyro controller with gimbal angles [0 0 0 0].

Above, Figure 3.2.10 shows a response which is very similar to that of the single-axis controller in Figure 3.2.4. Especially evident in Figure 3.2.10 is the matched response of all three gyro errors. An equivalent response is observed when varying the outer, middle,

and platform gimbal angles. The only configuration leading to different responses is inner angle dependent. This is shown below.
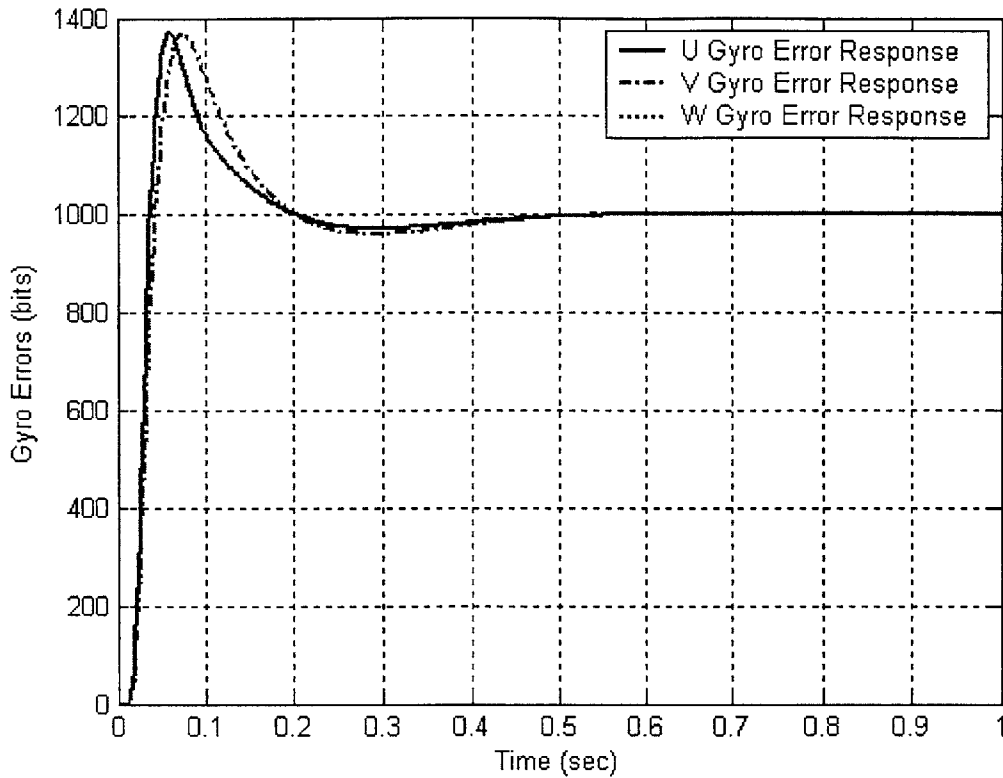
Figure 3.2.11 - A 1000 bit step response for the multi-axis gyro controller with gimbal angles [0 0 45 0].

In Figure 3.2.11, although the response of the V gyro error is different from the U and W, the three responses are very close and all within the specifications given in Table 3-1. The difference in the response is due to the neglect of the gain term in (3.2.13) as explained previously. This term is a maximum with the inner gimbal angle at 45 degrees hence, the response of Figure 3.2.11 is the worst-case scenario. As the difference in the responses of the errors in Figure 3.2.11 is very small, and as all the responses meet the response requirements, neglecting the term in (3.2.13) is deemed acceptable.

3.3 Gimbal Lock Avoidance

The classical controller employs a separate single-input, single-output control loop to prevent gimbal lock. This GLA loop necessitates defining a monotonically increasing, scalar error metric with a maximum when both the middle and inner angles are equal to 90 degrees. This is as follows.

$$\lambda = \sin(\theta_2) \cdot \sin(\theta_3)$$ (3.3.1)

Lambda is a convenient way to express how geometrically close the system is to gimbal lock in a quantitative way. As lambda approaches one, the torque motor axes converge toward alignment in a single plane as can be observed in Figure 2.1.1. Thus, as lambda approaches one, the system approaches gimbal lock, but as long as lambda remains small, the system remains controllable.

To null the lambda error, the platform controller first calculates lambda using gimbal angle measurements and then computes a compensated error known as the redundant error. The redundant command is limited to ensure that the redundant torque requirements do not infringe on the gyro error torque requirements. In block diagram form, this is as follows.
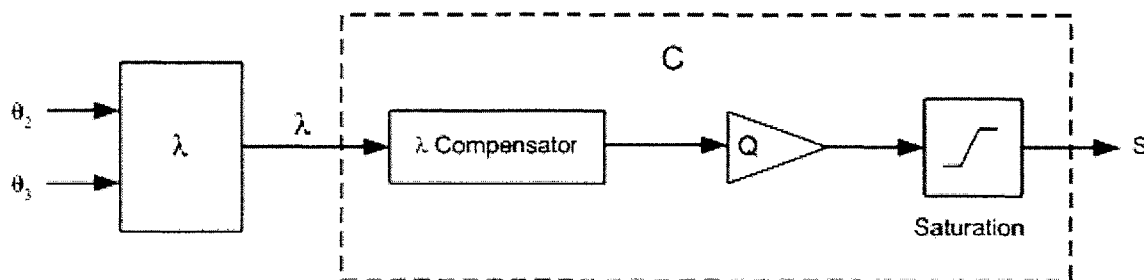
Figure 3.3.1 - Block diagram of the lambda error compensator.

In Figure 3.3.1, the calculation of lambda is straight forward, as given in (3.3.1). The angles are obtained from the resolvers as described in section 2.2. In order to help avoid

63

interference with the gyro control loops, the lambda compensator runs at a relatively slower rate of 100 Hz and is as follows.

$$\lambda(z) = 0.796875 \cdot \left[\frac{z^2 - 0.9}{z^2 + 0.2z + 0.01} \right]$$
(3.3.2)

The Q modulation gain following the lambda compensation is either a 1 or a -1 depending on the gimbal angles. In cases where the sine of the middle gimbal is greater than the sine of the inner gimbal, Q is equal to 1. When the sine of the inner gimbal is greater than the sine of the middle gimbal, Q is equal to -1. There is also some hysteresis in Q to ensure that Q does not flop back and forth rapidly when the sine of the middle angle is close to the sine of the inner angle.

Finally, by design, the compensated lambda error is saturated at about 60% of the full-scale torque available. This is to ensure that the torque requirements on the motor due to the lambda errors are not so large as to prevent torque from being available to null gyro errors. The saturated lambda error is called S in Figure 3.3.1. This S is the same as is referenced in Figure 3.2.9 which is added to the R compensated gyro error while maintaining orthogonality. Thus, the total compensator C in Figure 3.2.8 incorporates both the multi-axis controller in Figure 3.2.9, as well as the lambda compensator in Figure 3.3.1

Chapter 4

A Pseudo-Optimal Control Approach

4.1 The Linear Quadratic Regulator

The classical design of the platform controller performs two main functions namely, gyro error nulling and lambda error nulling. This is accomplished using four separate compensators, one for each gyro error and one for the lambda error. Each of these compensators is designed to meet specific time and frequency response characteristics. While this theory of designing to meet requirements is certainly valid, it can leave open much room for improvement. Hence, in modern optimal control theory, it is often the case that, as an alternative to time and frequency requirements, a cost function is defined and then minimized, thus providing a mathematically optimal solution offering the best possible performance characteristics.

As is discussed in section 3.1, with four gimbals it is theoretically possible to maintain small lambda error for a large class of input case motions. In the case of the optimal control scheme, rather than computing a lambda error and then using a compensator as is done in the classical controller, the optimal controller will compute the gimbals angles necessary for zero lambda error for a given platform orientation. Then, the gimbals will be commanded to these angles in an optimal fashion thus creating near-zero lambda error while maintaining the platform orientation.

As this problem is essentially one of regulation, an obvious choice for an optimal controller is a Linear Quadratic Regulator, or LQR. The theory behind LQR control is well known and will only be discussed briefly.
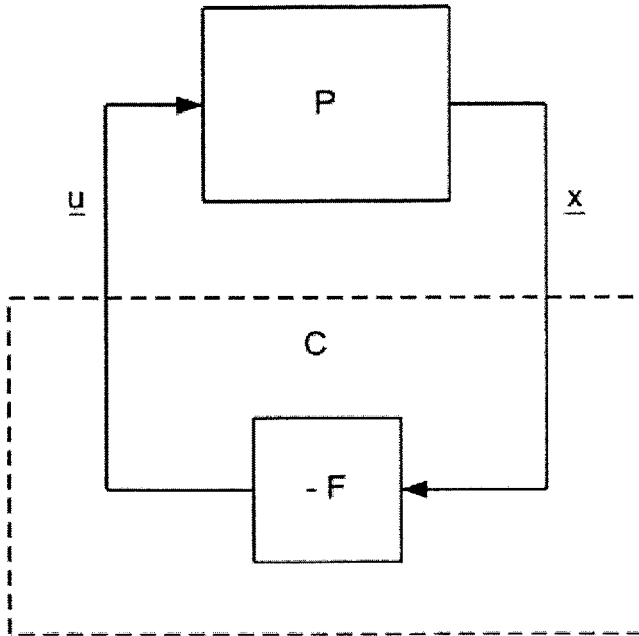
Figure 4.1.1 - Block diagram of a regulatory system.

Figure 4.1.1 shows a block diagram for a regulatory system. The goal of this system is to drive the system states, $\underline{x}$, to zero using the negative feedback gain $-F$. The task of the LQR then, is to choose the gain F in such a way that the system states will reach zero in an optimal manner. To facilitate this, the following discrete cost function is defined.

$$J = \frac{1}{2}\sum_{k=0}^{N-1}\left[\underline{x}^{T}(k)Q(k)\underline{x}(k) + \underline{u}^{T}(k)R(k)\underline{u}(k)\right] \tag{4.1.1}$$

The cost function in (4.1.1) uses a quadratic weighting of the states, $\underline{x}$, versus the control effort, $\underline{u}$. A cost function such as this has two requirements. First, the system dynamics must be linear so that the $\underline{x}$ and $\underline{u}$ vectors can be formed. In the case of the four gimbal system, it is possible to linearize the system as was outlined in section 2.4. Second, (4.1.1) requires access to the complete state vector $\underline{x}$. For the four gimbal system, this

means measures of all gimbal angles and absolute angular velocities must be available. The gimbal position measurements are available from the gimbal resolvers, and the absolute rates are available by back differencing the position measurements to get the relative rates and then using (2.3.14) to get the absolute rates.

Note the following from Figure 4.1.1.

$$\underline{u} = -F\underline{x} \qquad\qquad (4.1.2)$$

So, by minimizing the cost function, J, subject to the dynamics of the system, the F which will optimally drive the states to zero can be obtained. For more on the subject of LQR see, for example, [3].

4.2 Reducing the Order of the System

The linearized perturbation model of the four gimbal system described in (2.4.11) has eight states, four inputs, and six disturbances. The six disturbances are neglected, as the aim of the controller will be to reduce the effects of the disturbances as much as possible. The four inputs are the four gimbal motor torques. However, in the classical design, the lambda controller calculates only one torque which is then resolved between the outer and middle torque motors. Thus, although the four gimbal system has four inputs, the lambda controller will utilize only two inputs. Thus, following is the reduction of the linearized perturbation system to two inputs, instead of four.

As the platform gimbal angle, θ_4, is not present in any of the terms found in Appendix B, it is completely uncoupled, so it is removed without consequence along with the platform gimbal angular velocity, ϖ_{4x}. Unfortunately, this is not the case with θ_3, as the inner gimbal angle shows up in the $B_{1,2}$ term and elsewhere. However, even if the inner angle is removed as a system state, the resolver measurement of the angle is still available.

Thus, the inner angle can become a known parameter of the system, rather than a state. In this way, the four gimbal system is reduced to two gimbals and two torque inputs.

By removing inner and platform angles, inner and platform angular velocities, and inner and platform motor torques, the following linear, time-varying system is achieved.

$$\underline{\delta\dot{x}}(t) = A_4(t)\underline{\delta x}(t) + B_4(t)\underline{\delta u}(t) \tag{4.2.1}$$

Here, the following definitions for A_4 and B_4 apply.

$$A_4(t) = \begin{bmatrix} 0 & 0 & A_{1,5} & A_{1,6} \\ 0 & 0 & A_{2,5} & A_{2,6} \\ A_{5,1} & 0 & 0 & 0 \\ 0 & A_{6,2} & A_{6,5} & 0 \end{bmatrix} \tag{4.2.2}$$

$$B_4(t) = \begin{bmatrix} B_{1,1} & B_{1,2} \\ B_{2,1} & B_{2,2} \\ 0 & 0 \\ 0 & 0 \end{bmatrix} \tag{4.2.3}$$

The numbering from (2.4.12) and (2.4.13) is maintained. The terms in (4.2.2) and (4.2.3) are now functions of states, inputs and the parameter θ_3. As the terms are symbolically identical to those in (2.4.12) and (2.4.13), the expressions for each of the terms in A_4 and B_4 can be found in Appendix B. To evaluate the matrices, nominal values for states and inputs as well as for θ_3 must be chosen. In this way, the time varying matrices in (4.2.2) and (4.2.3) become constant matrices.

4.3 Calculating the Optimal Gains

4.3.1 Solving the Riccatti Equation

With nominal conditions chosen, it is possible to calculate the matrices in (4.2.2) and (4.2.3), which define the linearized two gimbal system dynamics. Because the controller will be implemented on a digital computer, the linearized two gimbal system is discretized. This is accomplished in the following manner [5].

$$A_d = I_{n \times n} + A \cdot \Delta t + \frac{A^2 \cdot \Delta t^2}{2} + \frac{A^3 \cdot \Delta t^3}{6} + \cdots + \frac{A^i \cdot \Delta t^i}{i!} + \cdots \qquad (4.3.1)$$

$$B_d = B \cdot \Delta t + \frac{AB \cdot \Delta t^2}{2} + \frac{A^2 B \cdot \Delta t^3}{6} + \cdots + \frac{A^{i-1} B \cdot \Delta t^i}{i!} + \cdots \qquad (4.3.2)$$

In the above series, Δt is the sample time. As the optimal controller, just as the classical GLA controller, will run at 100 Hz, the sample time is 0.01 seconds. For more information about discretization, see [6].

It has been well established that for the cost function in (4.1.1), the optimal gain is given by F, defined as follows [4].

$$F_{ss} = \left(B_d^T P_{ss} B_d + R \right)^{-1} B_d^T P_{ss} A_d \qquad (4.3.3)$$

In addition, the infinite horizon solution for P_{ss} is defined by the Algebraic Riccatti Equation as follows [4].

$$A_d^T P_{ss} A_d - A_d^T P_{ss} B_d \left(B_d^T P_{ss} B_d + R \right)^{-1} B_d^T P_{ss} A_d + Q = 0 \qquad (4.3.4)$$

A solution to the set of equations in (4.3.3) and (4.3.4), for which constant Q and R weighting matrices have been assumed, can be found using a computer algorithm, such as the "dlqr" command in Matlab [7]. For more information about solving the Algebraic Riccatti Equation, see for example [3].

4.3.2 Choosing the LQR Weightings

The Q and R terms in the cost function in (4.1.1) are relative weightings of state errors versus control effort. These terms obviously play a role in the calculation of the optimal gain F using (4.3.3) and (4.3.4). Expensive control, or large R relative to Q, yields a controller gain with low control effort requirements but which potentially allows for large deviations in state. On the other hand, cheap control, or small R relative to Q, yields a controller gain which maintains small state errors, but which potentially requires large amounts of control effort [5]. In choosing the Q and R weightings it should be remembered that Q must be symmetric and positive semi-definite and R must be symmetric and strictly positive definite, as infinite control effort is not physically realizable [4].

In the subsequent discussion, two different methods for choosing Q and R weightings are considered. The first, which is called the dial method, utilizes a single gain ρ in the R matrix, with the Q matrix equal to identity. This is as follows.

$$Q = \begin{bmatrix} 1 & 0 & 0 & 0 \\ 0 & 1 & 0 & 0 \\ 0 & 0 & 1 & 0 \\ 0 & 0 & 0 & 1 \end{bmatrix} \quad (4.3.5)$$

$$R = \begin{bmatrix} \rho & 0 \\ 0 & \rho \end{bmatrix} \quad (4.3.6)$$

Perhaps an easier way to understand the dial method is to see how it modifies the cost function. With the weighting given in (4.3.5) and (4.3.6), the cost function in (4.1.1) can be rewritten as follows.

$$J = \frac{1}{2}\sum_{k=0}^{N-1}\left[\underline{x}^T(k)\underline{x}(k) + \rho\underline{u}^T(k)\underline{u}(k)\right]$$

(4.3.7)

In (4.3.7) it is easy to see the classifications of expensive and cheap control. A large ρ means the control term will have a greater impact on the cost function, hence expensive control. Conversely, a small ρ means the state term will have a greater impact on the cost function and hence cheap control.

A second method for choosing Q and R incorporates the relative importance of the various states. With the dial method, no matter what the value of ρ is, all four states have identical weightings. With the relative state method, the weightings of the states relative to each other can be changed. In the case of the four states in the two gimbal system, there are two velocity states and two position states. Hence, the velocities can be weighted relative to the positions by choosing a Q and R as follows.

$$\underline{Q} = \begin{bmatrix} \alpha & 0 & 0 & 0 \\ 0 & \alpha & 0 & 0 \\ 0 & 0 & \beta & 0 \\ 0 & 0 & 0 & \beta \end{bmatrix}$$

(4.3.8)

$$R = \begin{bmatrix} 1 & 0 \\ 0 & 1 \end{bmatrix}$$

(4.3.9)

Here in (4.3.8), a large α relative to β indicates the velocity states are more important and a large β relative to α indicates the position states are more important.

4.3.3 Loop Shaping

To help visualize the effects of differing Q and R weightings, the following principles from loop shaping are utilized. According to Zhou [8], the object of loop shaping is to find a controller which shapes a loop transfer function such that the loop gains are within specified boundaries. This can be visualized as follows.
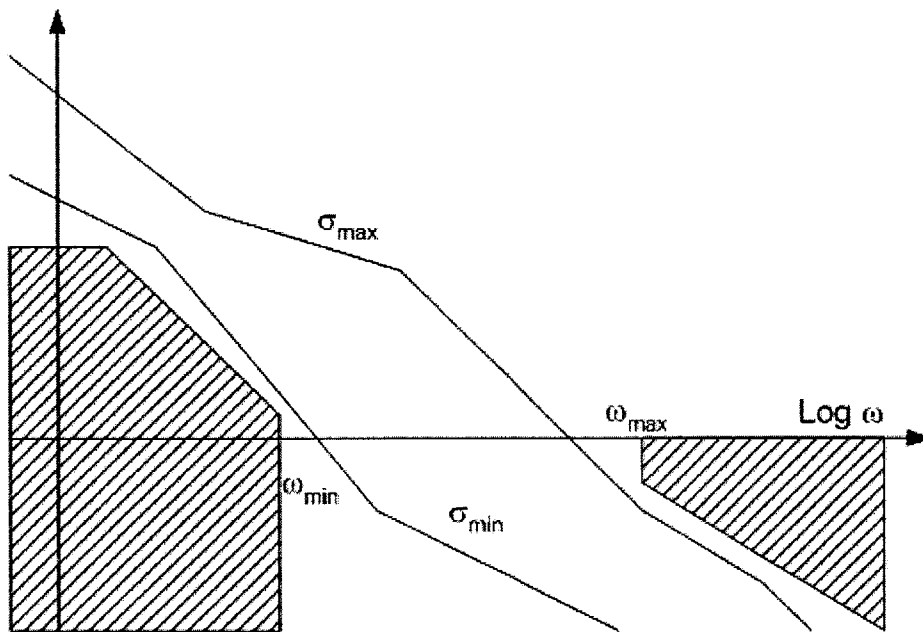
Figure 4.3.1 - Loop shaping boundaries.

In Figure 4.3.1 above, the lowest loop gain must be above the boundary specifying the performance requirements at low frequencies [8]. Similarly, the highest loop gain must be below the boundary specifying robustness requirements at high frequencies. For multi-input/multi-output (MIMO) systems, the singular values are used for the loop gains.

For the LQR system, the following control loop is established.
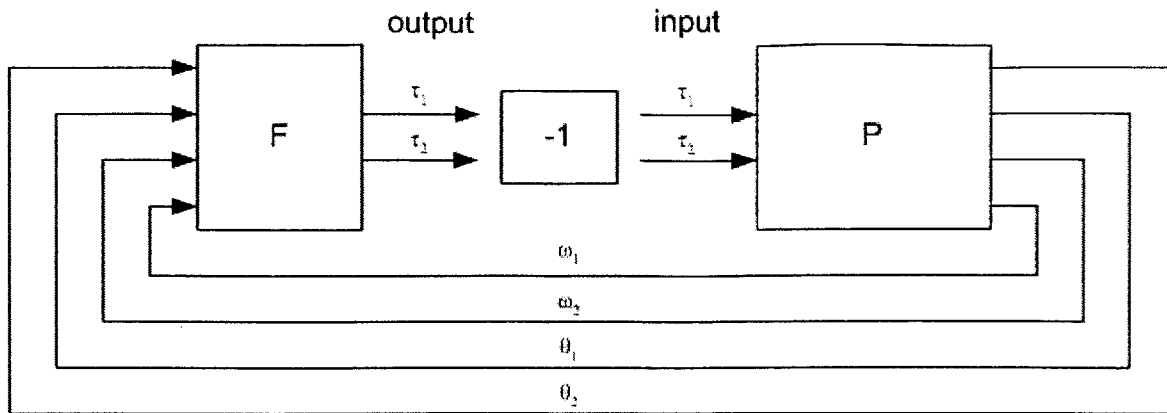
Figure 4.3.2 - Block Diagram of the open-loop LQR with linearized plant for loop shaping.

In Figure 4.3.2 above, the plant P contains the linearized dynamics given in (4.2.1). The controller F is the gain matrix computed from (4.3.3) and (4.3.4) above. The loop is opened before the plant. Obviously, the loop in Figure 4.3.2 does not include any of the gyro compensators; however, as the subsequent discussion will apply only to the choosing of the weightings for the lambda controller, the gyro loops will not be considered.

In the traditional loop shaping, the object is to use a controller with a transfer function in order to shape the loop. Obviously, the LQR design affords only a gain F, not a complete transfer function. However, by plotting the singular values of the MIMO system in Figure 4.3.2 above for various Q and R weightings, the effects of the weightings on performance can be visualized more clearly.

In the plots which follow, the singular values for the loop given in Figure 4.3.2 are plotted for various values of weighting gains and nominal conditions. The nominal gimbal angles are given in degrees.
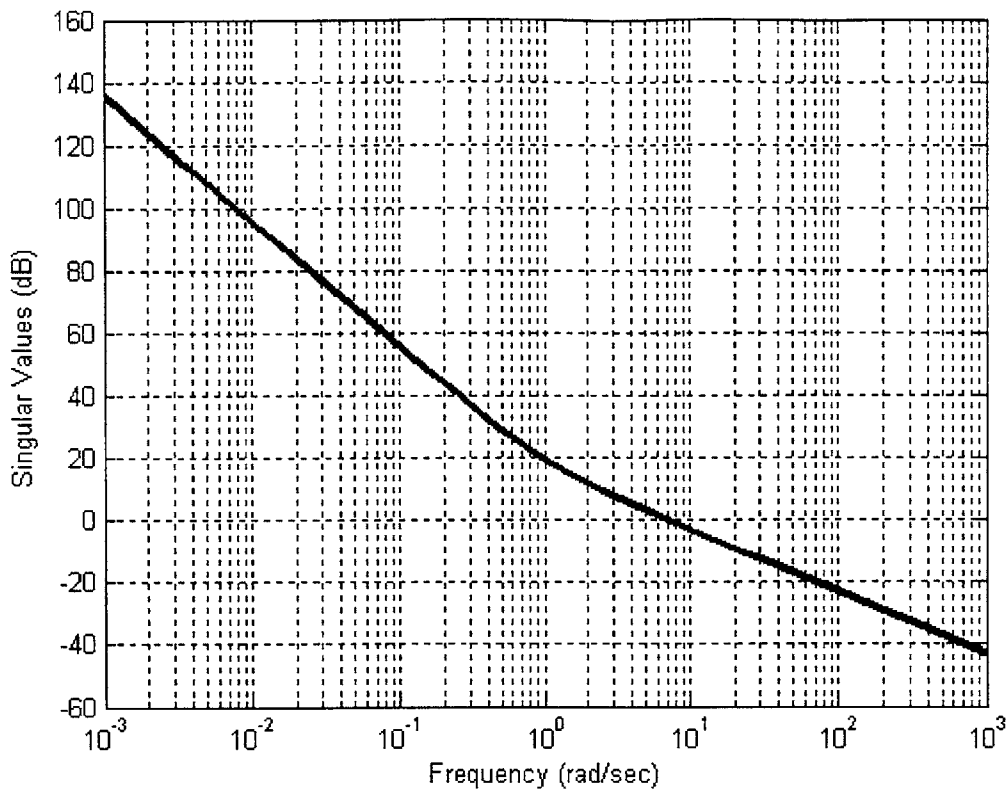
Figure 4.3.3 – Singular values for ρ of 1 and nominal gimbal angles [0 0 0 0].

Figure 4.3.3 shows the singular values with a ρ of one at the all-attitude zero nominal gimbal configuration. The two singular values lie on top of one another in the figure. This figure will be used as a benchmark for comparison as the weightings are changed.

A couple of interesting points can be made by looking at Figure 4.3.3. First, at low frequencies the singular values fall off at a rate of -40 dB per decade of frequency. As the plant is essentially a double integrator, this is consistent with the plant dynamics. Thus, at low frequencies, the loop singular values are dominated by the plant.

As the frequency increases, the slope of the singular values changes to -20 dB per decade. This is consistent with the response expected from a first order, low-pass filter [9]. Thus, Figure 4.3.3 above shows that, at low frequencies, the loop is dominated by the plant dynamics and then at high frequencies, the controller takes over.

74

Singular Values (dB)

160
140
120
100
80
60
40
20
0
-20
-40
-60

10^{-3} 10^{-2} 10^{-1} 10^{0} 10^{1} 10^{2} 10^{3}

Frequency (rad/sec)
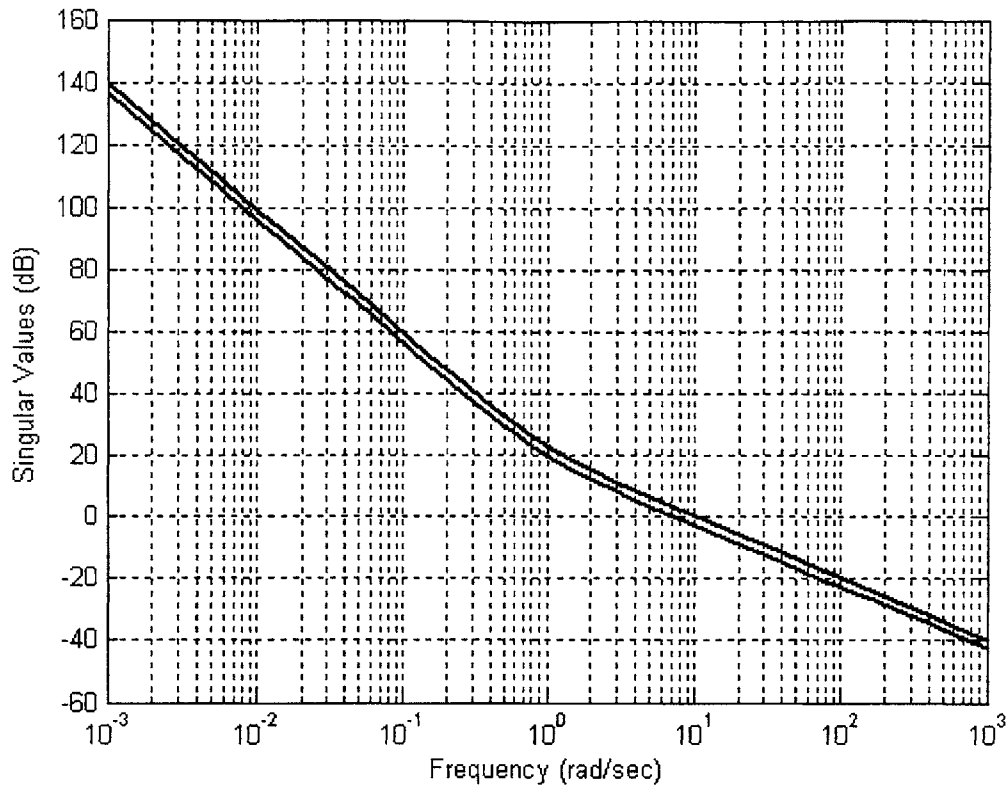
Figure 4.3.4 - Singular values for p of 1 and nominal gimbal angles [0 -60 -70 0].

Figure 4.3.4 shows the consequence of adjusting the nominal conditions. The values of the nominal angles were chosen for the same reason as was explained in section 2.4.2, namely they are the angles which produce the most cross-coupling in the dynamics. However, as can be seen in Figure 4.3.4, even for this worst-case nominal gimbal angle condition, the singular values are still very close together. Thus, for the subsequent plots, the nominal condition will be the all-attitude zero configuration.

Next, the effects of the dial method will be explored.
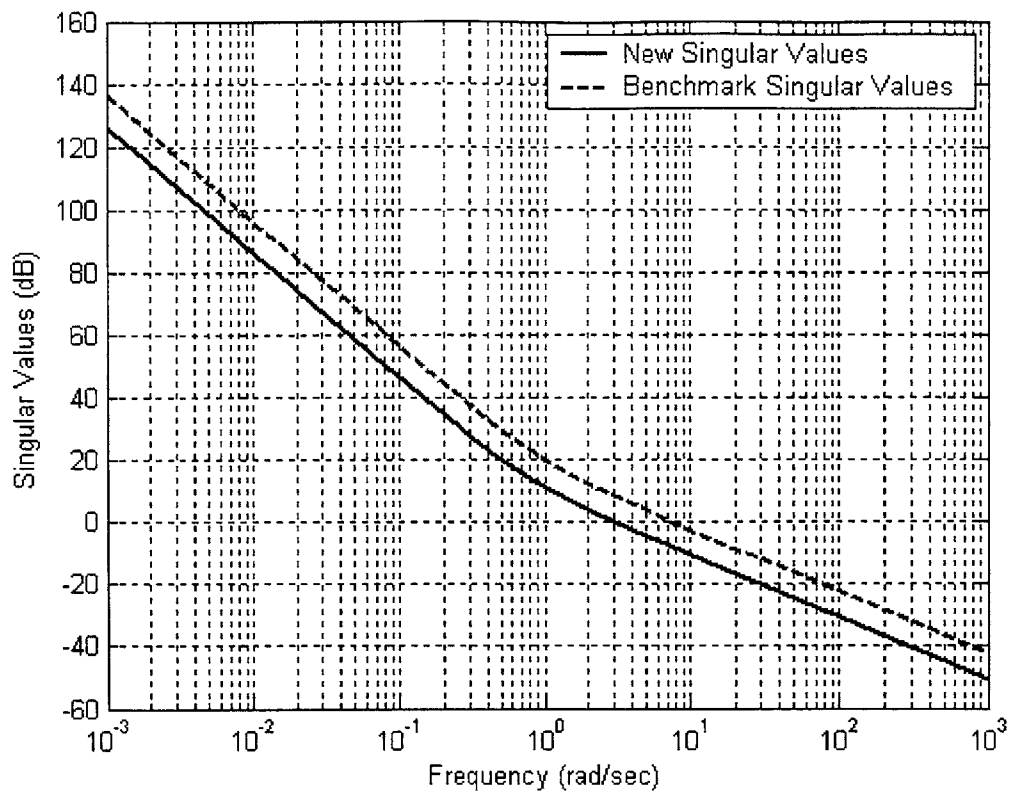
Figure 4.3.5 - Singular values for ρ of 10 and nominal gimbal angles at all-attitude zero.

Here in Figure 4.3.5, the singular value curves maintain the same shape but are uniformly lower in the case of expensive control. This is consistent with the concept that expensive control will yield worse system performance at low frequencies.

76
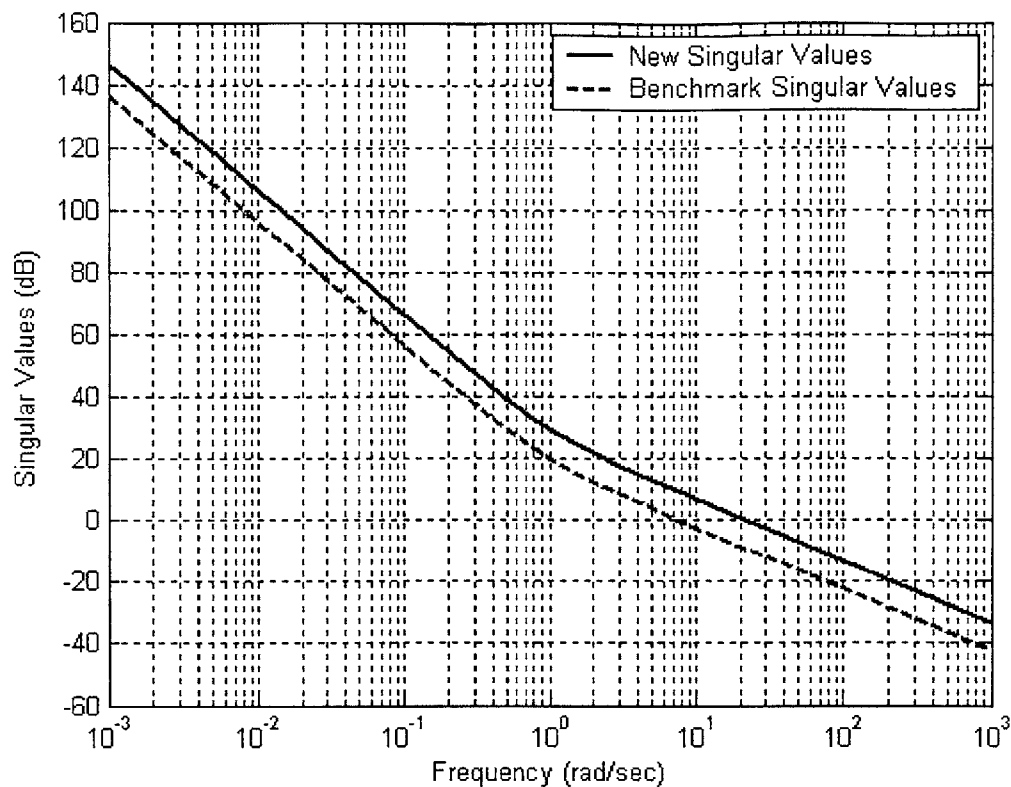
Figure 4.3.6 - Singular values for ρ of 0.1 and nominal gimbal angles at all-attitude zero.

In Figure 4.3.6 for cheap control, better low frequency performance is obtained. At this point it should be obvious that in the case of the dial method, no real loop shaping can occur. Because the singular value curves move uniformly up and down, the values of ρ which correspond to better low frequency performance also create worse high frequency attenuation, and vice versa. Therefore, in order to adjust the shape of the curves, the relative states method for choosing Q and R is investigated.
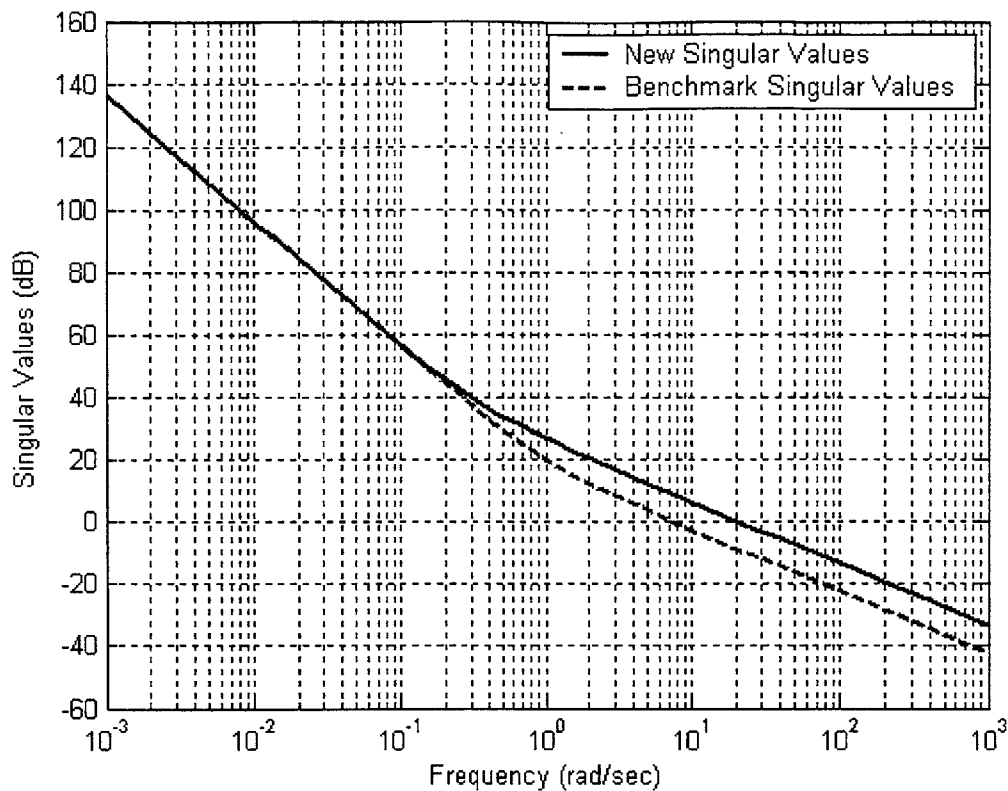
Figure 4.3.7 - Singular values for α of 10 and β of 1 with nominal gimbal angles at all-attitude zero.

In Figure 4.3.7 for a larger weighting on the angular rates, the singular values at high frequency are increased, with the slope remaining the same. At low frequency, the singular values are unchanged from the benchmark. Increasing the weighting on the states is equivalent to decreasing the weighting on the control; hence Figure 4.3.7 can be compared with the cheap control example in Figure 4.3.6.
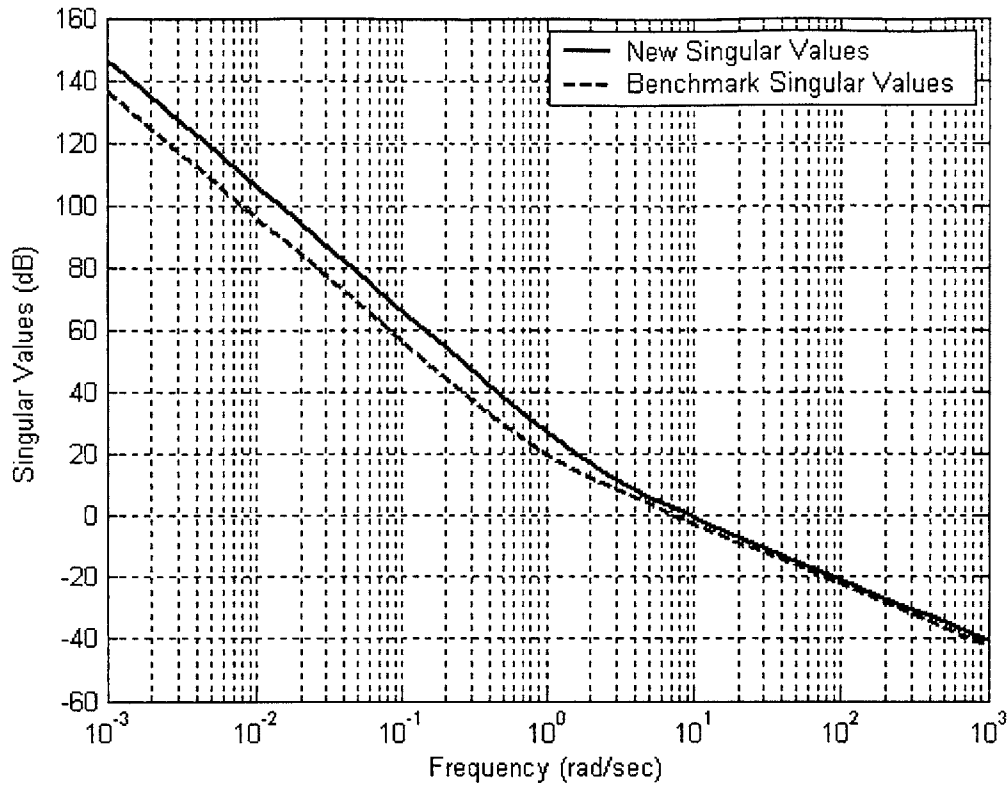
Figure 4.3.8 – Singular values for α of 1 and β of 10 with nominal gimbal angles at all-attitude zero.

In contrast to Figure 4.3.7, in Figure 4.3.8 the singular values at low frequency are increased. Even so, the slope remains the same. At high frequency, the singular values are unchanged from the benchmark. This is for a larger weighting on the angles and can also be compared to the cheap control example of Figure 4.3.6.
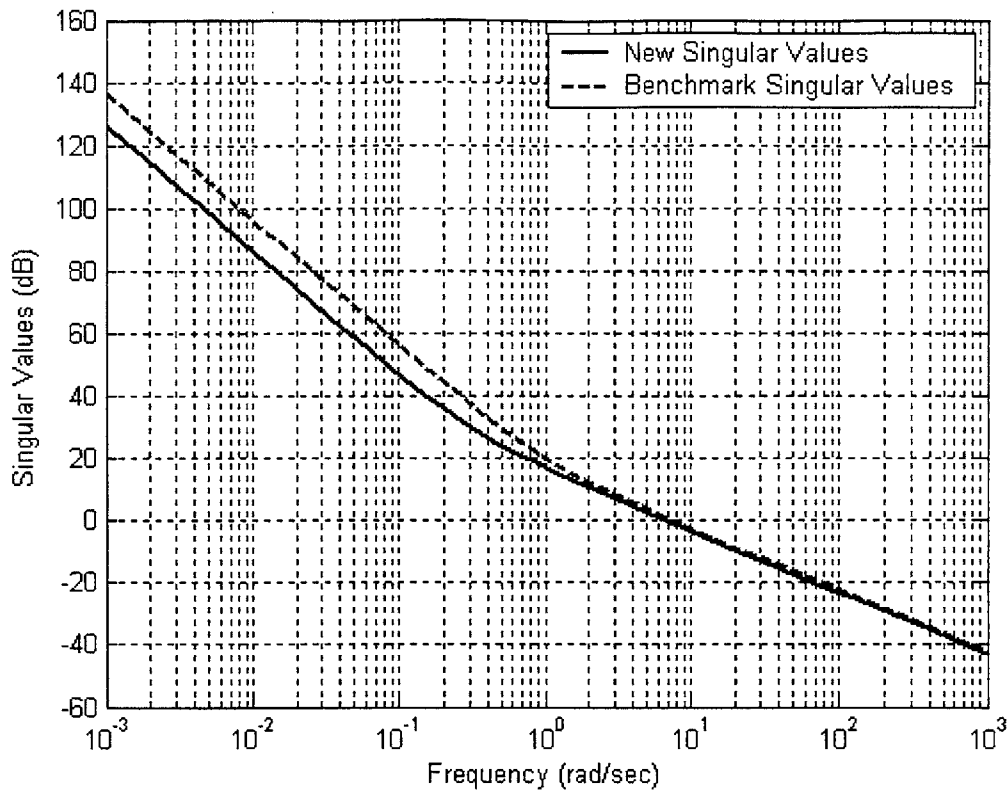
Figure 4.3.9 - Singular values for α of 1 and β of 0.1 with nominal gimbal angles at all-attitude zero.

Finally, in Figure 4.3.9, the weightings on the angles are decreased with respect to the angular rates and the control. This result can be compared with the expensive control result in Figure 4.3.5.

As has been demonstrated for the relative state plots above, loop shaping could be used to adjust the singular values so that they remain outside of some design limits, such as those given in Figure 4.3.1. As the lambda controller must eventually be combined with the gyro controllers, which are not modeled in the loop used in Figure 4.3.2, even with appropriate design constraints there is no guarantee the performance observed above would carry over to the complete platform controller. Nevertheless, by observing how the weightings affect the two gimbal system, insight into expected performance can be gained.

For the controller which is implemented as described below, a ρ of 10 is found to yield adequate performance and hence is used throughout the subsequent design.

4.4 Implementing the Pseudo-Optimal Controller

It is intended to replace the lambda compensator in the classical controller shown in Figure 3.3.1 with an LQR controller. Although the LQR controller is essentially only a gain, implementing this controller is more complex than it may first appear. The following is a description of the steps necessary to implement the LQR lambda controller into the complete platform controller framework.

4.4.1 The LQR Lambda Controller

Following is a block diagram overview of the LQR lambda controller.
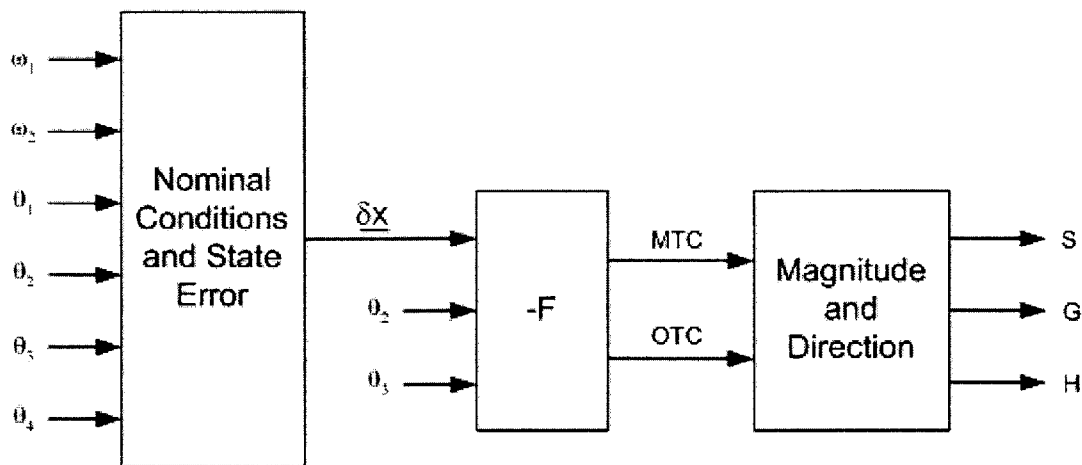
Figure 4.4.1 - Block diagram of the LQR lambda controller.

It is intended that the controller in Figure 4.4.1 above will generate the S signal shown in Figure 3.2.9. Hence, Figure 4.4.1 is intended to replace the controller in Figure 3.3.1. The inputs to the LQR controller consist of the two angle and two angular rate states, as well as two other angles which are treated not as states but as parameters. The outputs of

81

the controller are S, which is equivalent to the S produced by the classical lambda controller, and G and H, which will be needed when adding the S to the gyro control torques.

It should be mentioned that, unlike for the classical controller, the angle and rate inputs for the LQR controller are not obtained from the resolvers in this implementation. Instead, for simplicity, the values come directly from the mathematical plant model. If the LQR controller were implemented in a real system, it would be necessary to use the resolver values for the angles and a back difference of the angles for the rates.

The sections which follow detail some of the block components found in Figure 4.4.1.

4.4.2 Calculating the State Error

The linearized perturbation model of equation (4.2.1) represents the dynamics of the system linearized about nominal conditions. The states of this system are actually deviations of the total states away from the nominal conditions as defined in (2.4.6) and (2.4.7). Effectively, the linearized perturbation regulator is not a standard regulator as in Figure 4.1.1, but instead as below.
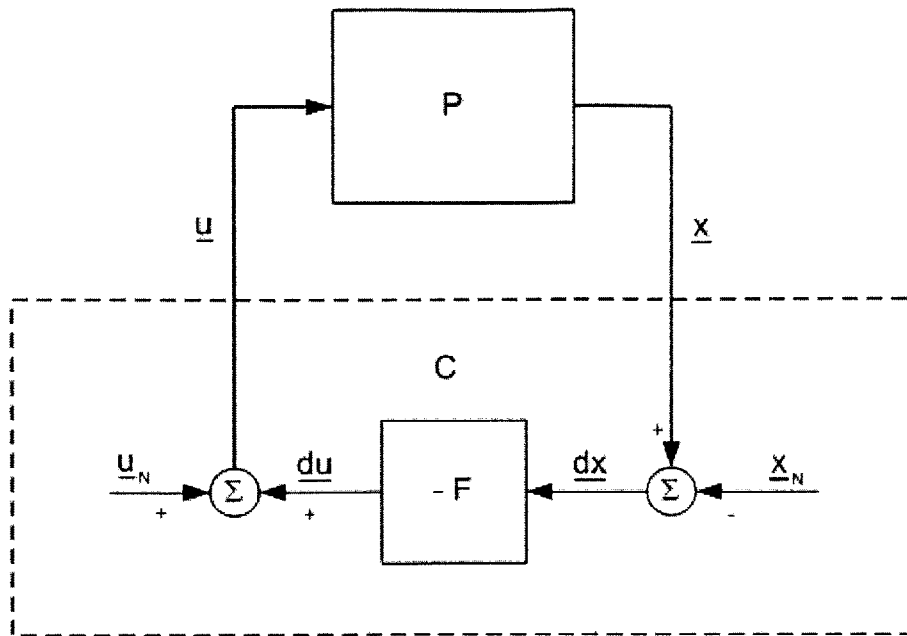
Figure 4.4.2 - Block diagram of the perturbation model under regulation.

As seen in Figure 4.4.2 above, the controller must measure the states, $\underline{x}$, difference them from the calculated nominal states $\underline{x}_N$, and then use this state error, $\delta\underline{x}$, as the input to the controller. Similarly, the control error, $\delta\underline{u}$, must be added to the nominal input to obtain the input $\underline{u}$.

4.4.3 Calculating the Nominal Conditions

As mentioned above, one of the most critical tasks for the controller is calculating nominal conditions for the system. First, the nominal control inputs must be addressed. Here, the process is simplified by the fact that, for zero case motion disturbances, no control input is necessary. Hence, the nominal control inputs, $\underline{u}_N$, are at all times zero.

To calculate the nominal state conditions, the process is significantly more complex. For any platform orientation, there exist four gimbal configurations such that lambda is zero. These configurations occur when the middle or inner gimbal angle is equal to either zero or π. The challenge is to choose the configuration to which the gimbals could most easily

be driven. It is assumed that the configuration to which the system should be driven is the configuration which is closest to the current gimbal orientations.

The determination of the closest gimbal configuration yielding a lambda of zero is approached in a series of steps, a flow diagram of which follows.
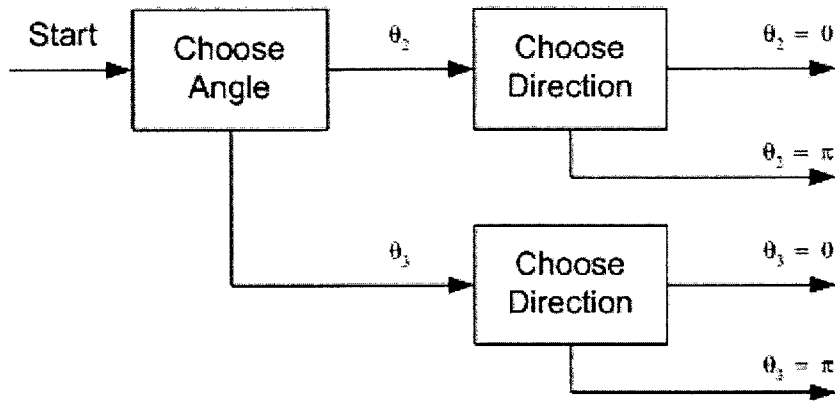
Figure 4.4.3 - Flow diagram for choosing the nominal gimbal angle for zero lambda.

The logic which chooses the gimbal configuration is as follows. First, the sine of the middle and inner angles are compared. If the absolute value of the sine of the middle angle is larger than that of the inner angle, then the inner angle sine will be driven to zero. Conversely, if the inner angle sine is larger, then the middle angle sine will be nulled.

With the decision between the middle and inner angles made, the controller must then decide whether the sine of the chosen angle should go to zero by driving the angle to zero or to π. For this, the 2π modulus of the gimbal angle, θ_2 or θ_3, is taken such that the result is an angle between $-\pi$ and π. If the absolute value of this resultant angle is closer to zero than to π, the angle is driven to zero, otherwise, the angle is driven to π. In totality, this logic yields both the gimbal angle which will be controlled and the direction in which it will be driven by choosing one of four possible gimbal configurations, all of which yield a lambda value of zero.

Once the value of one angle has been chosen, the remaining three gimbal angles can be calculated by making the assumption that the platform orientation remains constant. This is discussed in further detail in Appendix C. It should be remembered that, although four angles can be calculated analytically, only two of these will be used in the implementation of the controller. As was discussed in section 4.2, the inner gimbal angle and the platform gimbal angle are essentially uncoupled from the system and are not used as states in the reduced order model of equation (4.2.1). Hence, the nominal values of these angles are not needed.

With the nominal gimbal angles, $\underline{\theta}_N$, calculated, it is now possible to compute the nominal gimbal angle rates. It is recalled from section 2.3 that the rates, $\underline{\varpi}$, are absolute angular rates, whereas the gimbal angles themselves are relative angles. From (2.3.14), the following definition of the gimbal angle rates applies.

$$\begin{bmatrix} \dot{\theta}_1 \\ \dot{\theta}_2 \end{bmatrix} \equiv \begin{bmatrix} \varpi_{cz} \\ \varpi_{1z} \end{bmatrix} - \begin{bmatrix} \varpi_{1x} \\ \varpi_{2x} \end{bmatrix} \tag{4.4.1}$$

Assuming zero case motion disturbances, the ϖ_{iz} terms go to zero, and using a first order approximation for the derivatives, this expression for the nominal inertial rates is obtained.

$$\begin{bmatrix} \varpi_{1x}^N \\ \varpi_{2x}^N \end{bmatrix} = \begin{bmatrix} \dfrac{\theta_1(k) - \theta_1(k+1)}{\Delta t} \\ \dfrac{\theta_2(k) - \theta_2(k+1)}{\Delta t} \end{bmatrix} \tag{4.4.2}$$

In (4.4.2) above, the $\theta_i(k)$ terms are the current measured gimbal angles. The $\theta_i(k+1)$ terms are the computed nominal gimbal angles. Essentially, these are the angles to which the system should be driven.

The time constant, or Δt, in (4.4.2) is a design parameter. This parameter is defined as follows.

$$\dot{\theta}_G = 1/\Delta t \qquad\qquad (4.4.3)$$

The parameter defined in (4.4.3) above is called the theta dot gain. Essentially, it determines how fast the LQR lambda controller should try to drive the errors to zero, or, in other words, how important the angular rate perturbation states are to controller performance. As this gain is a design parameter, different values for the gain can be tried with the theta dot gain leading to the best system performance used. Differing theta dot gains and the process of choosing an appropriate one will be demonstrated when presenting the results of the LQR control design.

With the nominal values computed, the LQR controller now looks as follows.
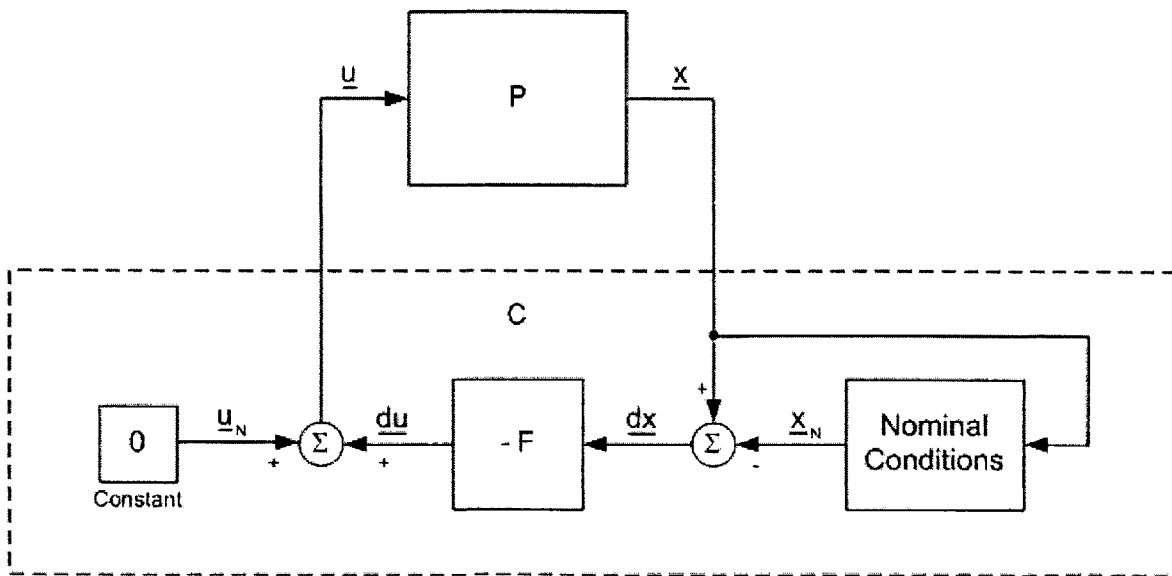
Figure 4.4.4 - Block diagram incorporating nominal states and inputs for the perturbation model under regulation.

Above, Figure 4.4.4 shows a simplified diagram for the implementation of the LQR lambda controller. Note that knowledge of the two gimbal angle states and two gimbal angle parameters is all that is needed to compute the nominal conditions.

4.4.4 Calculating the F Matrix

With the nominal conditions and the perturbed states calculated, the next step is to calculate the gain matrix F. In section 4.3.1, the solution for this matrix is given. However, this solution depends on the system dynamics in (4.2.1). As these are linearized dynamics, they are only valid while the states remain close to the nominal conditions for which the A_4 and B_4 matrices are calculated. Thus, the proper method for calculating F would be to calculate the nominal conditions first, then use these nominal conditions and the inner gimbal angle as a parameter to calculate the A_4 and B_4 matrices, after which the F matrix could be calculated.

Unfortunately, this method of computing the optimal gain is not practical for real-time implementation. In particular, the number of calculations required to find P in (4.3.4) is significant, increasing the time delay in the system and potentially offsetting performance improvements gained by using an optimal controller. Instead, it is desirable to calculate the F matrix a priori. This calculation of gain off-line leads to a new problem with calculating the nominal conditions. As explained previously, the nominal conditions are a function of current platform and gimbal angle orientation, and thus are time-varying.

To overcome this situation, a number of different F matrices are computed for a variety of different nominal conditions. These different F matrices are then stored in a table. In the real-time system, an F matrix is chosen based on the table value which is closest to the current nominal conditions. This then avoids the time delay problems of computing the F matrix in the real-time system.

To reduce as much as possible the number of different F matrices to be calculated and stored, the following simplifications are made. First, the nominal gimbal inertial rates, $\underline{\varpi}$, are taken to be zero. This turns out to be a good approximation, as the design limits

of the system call for a fairly small maximum input motion of less than 45 degrees per second.

Second, the nominal outer gimbal angle is taken to be zero. As was discussed in section 2.4.2, the choice of nominal outer gimbal angle does not affect the dynamics and thus can remain zero. This leaves the middle gimbal angle as the only state which will have a bearing on the F matrix. However, as discussed above in section 4.2, aside from the nominal states, a parameter must be used to calculate the A_4 and B_4 matrices in (4.2.2) and (4.2.3). This parameter is the inner gimbal angle and thus, two angles will affect the F matrix. It just so happens that these angles are also the angles considered by the classical lambda controller.

To calculate the F matrices, the continuous variables of middle and inner gimbal angles are discretized with a spacing of eight degrees. This is based on the testing of the linearized perturbation model explained in section 2.4.2. Fortunately, the gimbal angles are periodic and can only take values in the following range.

$$- \pi \leq \theta_i \leq \pi \qquad (4.4.4)$$

Thus, each angle is discretized over this range, and the A_4 and B_4 matrices are computed for each possible set of angles. Then, the F matrix is computed using each of these sets of A_4 and B_4 matrices. Finally, these F matrices are saved in a look-up table which is used in the real-time LQR lambda controller. The function of the $-F$ block in Figure 4.4.1 is to take the measured middle and inner gimbal angles, look up the F matrix in the table which is closest to these angles, and then do a matrix multiplication of the perturbed states with the chosen F matrix.

The LQR controller implemented in the fashion described above is not truly an optimal controller because the F matrix utilized at any point is time is only an approximation of the optimal F. The F utilized has been calculated a priori based on nominal conditions

which can be up to four degrees different from the current nominal conditions calculated by the controller. For this reason, the LQR controller is called pseudo-optimal.

4.4.5 Determining the Torque Command Magnitude and Direction

The outputs of the F block in Figure 4.4.1 are two torque commands, one for the outer gimbal and one for the middle gimbal. Ideally, these torque commands would be added to the commands produced from the gyro error compensators. However, as was discussed in section 3.2.2, it is important to keep the gyro commands orthogonal to the lambda commands. This orthogonality is maintained in the classical controller through the use of equation (3.2.14). However, this equation calls for only a single lambda torque, not an individual torque for each gimbal.

The purpose of the magnitude and direction block in Figure 4.4.1 is to create a single torque command, S, which can be added to the R compensated error through the use of (3.2.14). Thus, the magnitude of the total torque command is found as follows.

$$S = \sqrt{OTC^2 + MTC^2}$$
(4.4.5)

The S command from (4.4.5) above could then be added to the R compensated error using (3.2.14). However, this S command only preserves the magnitude of the LQR lambda commands, not the direction. In order to preserve the direction, the signs of the commands are also needed. These are found as follows.

$$G = \text{sgn}(MTC)$$
(4.4.6)

$$H = \text{sgn}(OTC)$$
(4.4.7)

The two signs in (4.4.6) and (4.4.7), and the S torque command from (4.4.5), are reported by the magnitude and direction block in Figure 4.4.1.

4.4.6 Torque Resolution

With the magnitude and direction of the LQR lambda compensator torque reported, the final task is adding this torque to those produced by the gyro error compensators. This process is very similar to that outlined in section 3.2.2. The one exception is that the LQR commands do not need to be multiplied by the dynamic inertia correction, as the LQR lambda controller has already considered the effects of the changing inertias by selecting the F based on gimbal angles. Thus, the following equations describe how to add the LQR lambda torque to the gyro error compensation torques.

$$MGTQ = c\theta_3 K_{jm} R + \text{sgn}(c\theta_2 s\theta_3)c\theta_2 s\theta_3 GS \qquad (4.4.8)$$

$$OGTQ = c\theta_2 s\theta_3 K_{jo} R + \text{sgn}(c\theta_3)c\theta_3 HS \qquad (4.4.9)$$

In (4.4.8) and (4.4.9) above, the dynamic inertia corrections are given just as before by (3.2.15) and (3.2.16). The G and H are either positive or negative ones given by (4.4.6) and (4.4.7). Also, the S is calculated from (4.4.5) above. Finally, the signs of the trigonometric terms are included to ensure the torque motors drive the gimbals in the proper direction to null the lambda error.

Chapter 5

Results

5.1 Missile Maneuvers and Metrics

To test the performance of the classical and LQR controllers, they are implemented in Matlab software as two separate models in Simulink. These models of the system include the compensators as described in Chapter 3 and Chapter 4 respectively, as well as the nonlinear plant equations described in (2.3.11) and (2.3.15) which are common to both. By establishing initial gimbal positions and defining the case motion trajectory input, these models will predict the response of the system to the each of the platform controllers.

In order to be able to compare the two controllers, it is necessary to define some input motions, initial conditions, and metrics which will be common to both models. These are outlined in the following sections.

5.1.1 The Test Scenarios

In defining the case trajectory input, pitch-only motion is considered. Any maneuver created using yaw motion can be equivalently recreated using pitch motion with different initial gimbal angles. Thus, yaw motion is not examined. Also, although a missile need

not be roll controlled, roll components are assumed to be negligible for this design and thus, roll input is also neglected.

Two separate scenarios are considered. In the first scenario, initial gimbal angles are selected and the case is accelerated about the pitch axis at the maximum angular rate, given in section 2.1, of 3 radians per second squared. This acceleration continues until the maximum rate of 45 degrees per second is reached. At this point, the case continues to pitch at the maximum rate until the simulation is stopped. This is called the coast scenario.

In the coast case, such continuous pitch motion is not anticipated in flight, but is merely established as a test condition. In any case, if the simulation were allowed to continue for a long period of time, the periodicity of gimbal motions would become apparent. Thus, it is only necessary to capture one of these periods of motion to understand the missile performance for the coast scenario. It is observed that, under the above described angular acceleration environment, 5 seconds is an adequate time frame for observation of a single period of gimbal motion.

The second scenario starts just as the first, with acceleration to the maximum rate. However in this scenario, the case is decelerated back to zero after a period of coasting. This introduces another variable, namely the time at which to begin the deceleration. However, by decelerating at strategic moments, more stressful GLA maneuvers can be created. This scenario is known as the deceleration scenario.

The initial gimbal angles are chosen in order to demonstrate the performance of the controller in preventing gimbal lock. To this end, the system is initialized as close as possible to gimbal lock, but with a lambda of zero. Two separate scenarios accomplish this goal.

$$\underline{\theta}_{IC} = \begin{bmatrix} x & 90 & 0 & 0 \end{bmatrix}$$

(5.1.1)

$$\underline{\theta}_{IC} = \begin{bmatrix} x & 0 & 90 & 0 \end{bmatrix}$$

<div align="right">(5.1.2)</div>

In the first configuration in (5.1.1), the middle gimbal angle starts at 90 degrees with the inner gimbal at zero. This is known as the null-inner configuration. In the second case in (5.1.2), the inner gimbal angle starts at 90 degrees with the middle angle at zero. This is known as the null-middle configuration. Both of these configurations are considered. The x in (5.1.1) and (5.1.2) represents that the outer gimbal angle is varied to produce a variety of gimbal motions, some leading more directly to gimbal lock than others. Also, although these configurations are designed to null the inner and middle gimbal components of lambda respectively, it is possible that the case motion trajectory may lead to a switch in the controlled gimbal during a particular maneuver.

5.1.2 The Metrics

In comparing the results of the classical control approach to those of the optimal approach, it is necessary to establish logical, fixed criteria on which to base the comparison. Three separate but related criteria are considered.

First, and perhaps most logical, is lambda error. Lambda, as defined in (3.3.1) is calculated during the various maneuvers discussed above. The peak value of this error over the time interval of the maneuver, whether positive or negative, is recorded. The absolute value of this peak error then gives a measure of how close the gimbals come to gimbal lock. As the controller is designed to prevent gimbal lock, this is a critical measure of system performance.

As discussed in section 3.1, the platform controller has two purposes, to prevent gimbal lock, and to keep platform motion to a minimum. As the lambda error only reveals controller performance in preventing gimbal lock and not in minimizing platform motion, clearly another error measure is needed. For this, gyro error is used.

It can be recalled from section 3.2.2 that there are three orthogonal gyro measurements. To convert these three signals into a single error measurement, the Root Sum of Squares or RSS value of the signals is taken at each instant in time for which the gyro error measurements are available. This produces a single, always positive error measurement, the maximum value of which indicates the maximum deviation of the platform from its inertial reference.

Finally, although the maximum RSS of the gyro errors reveals the largest platform deviation, it glaringly neglects the duration of the deviation. As discussed in section 1.1, integrals of measurements from the accelerometers mounted to the platform will be used to calculate velocity and position for navigation. Thus, for each instant where the platform is misaligned with inertial space, the accelerometer data is effectively integrated in the wrong direction. This means a small magnitude but long duration gyro error transient may actually be worse than a large magnitude but short duration transient. So, yet another error measurement is needed for a complete representation of system performance.

Acceleration error is the error in the acceleration measurement due to platform misalignment, and velocity error is its integral. Acceleration error is computed by transforming the linear missile acceleration in the missile frame to the platform frame. This is accomplished using the transpose of (C.1) as follows.

$$\underline{a}_{UP} = T^{UP}_{XM} \cdot \underline{a}_{XM} \qquad (5.1.3)$$

Further, the acceleration is transformed to the inertial frame.

$$\underline{a}_{UI} = T^{UI}_{UP} \cdot T^{UP}_{XM} \cdot \underline{a}_{XM} \qquad (5.1.4)$$

In (5.1.4) above, the transformation from the UVW platform frame to the UVW inertial frame can be expressed as follows.

$$T_{UP}^{UI} = \begin{bmatrix} 1 & -W_{gyro} & V_{gyro} \\ W_{gyro} & 1 & -U_{gyro} \\ -V_{gyro} & U_{gyro} & 1 \end{bmatrix} \tag{5.1.5}$$

In the case where the U, V, and W gyro errors are non-zero, (5.1.5) is not an orthogonal transformation. However, for small angles, it is a good first-order approximation.

Acceleration error is simply the difference between the two transformations in (5.1.3) and (5.1.4). In the case where the platform is perfectly aligned with the inertial frame, the error is zero; otherwise, the acceleration error captures the platform misalignment.

$$\underline{a}_e = \underline{a}_{UI} - \underline{a}_{UP} \tag{5.1.6}$$

Substituting (5.1.3) and (5.1.4) into (5.1.6) above and simplifying, the following is reached.

$$\underline{a}_e = [T_{UP}^{UI} - I] \cdot T_{XM}^{UP} \cdot \underline{a}_{XM} \tag{5.1.7}$$

The bracketed difference in (5.1.7) yields a skew-symmetric matrix which is used to calculate the acceleration error as follows.

$$\underline{a}_e = \begin{bmatrix} 0 & -W_{gyro} & V_{gyro} \\ W_{gyro} & 0 & -U_{gyro} \\ -V_{gyro} & U_{gyro} & 0 \end{bmatrix} \cdot T_{XM}^{UP} \cdot \underline{a}_{XM} \tag{5.1.8}$$

Equation (5.1.8) is a first order approximation of the acceleration error. The integral of this over time is the velocity error. The RSS of the steady-state values of the velocity error yields a single value of error. It is important that the steady-state velocity error be used because it accounts for the total error to be incurred by the accelerometers and hence

95

the total navigational error caused by a missile maneuver. Although velocity error can be calculated at any point in time, the steady-state value is available only with zero gyro errors and zero input case motion. Thus, velocity error is only reported in the case of the deceleration scenario.

Velocity error is useful as it reveals the difference between actual missile velocity and predicted missile velocity due to a particular platform error transient. Overall missile accuracy is most affected by velocity error, so this is a critical quantity to keep small [1]. Also, while the acceleration error will naturally return to zero over time as the platform realigns itself with its inertial reference, eliminating accumulated velocity error would require complex missile maneuvers or complicated compensation equations. This is a further reason to maintain small velocity errors in the first place.

Although velocity error is directly related to gyro error, large RSS gyro error does not necessarily lead to large velocity error. As discussed above, maximum RSS gyro error neglects the time duration of the gyro error transients. Velocity error captures both the magnitude and duration of the errors.

It should be noted that for all of the subsequent plots showing velocity error, a linear acceleration of 5g or 161 feet per second squared along the roll axis of the missile was used.

Finally, although not considered a metric, the absolute values of the largest torques for the outer and middle gimbal during some of the worst deceleration maneuvers are also presented. The maximum total torques and the maximum redundant torques are included. Although these torque maxima are not necessarily indicative of system performance, they help to understand at what capacity the motors are working during a given maneuver. This information can be used to ascertain when the controller is working at its limit, and where the controller has room for improvement. Thus, the torque maxima are reported.

5.1.3 The Search Technique

To compare results from the classical controller to those from the LQR controller, steady-state RSS velocity error will be used. To this end, it is desirable to determine the absolute maximum RSS velocity error allowed by each controller. However, this is a highly difficult task.

The search space contains two continuous variables, initial outer gimbal angle and deceleration time, over which a search must be conducted. For simplicity, the search constitutes two separate steps. First, eliminating the deceleration time by using the coast scenario, the initial outer gimbal leading to the maximum RSS gyro errors is determined. Gyro errors are used in this step because velocity errors are only available for the deceleration scenario and gyro errors are more closely related to velocity errors than are lambda errors. Second, fixing the initial outer gimbal angle at the value determined in the first step, the deceleration time causing the largest steady-state RSS velocity error is determined.

For the first step, the continuous variable of initial outer gimbal angle is discretized over an interval with a specified coarseness, called the grid spacing. Next, the coast scenario is run for each value of outer gimbal angle in the interval. The maximum RSS gyro error from each run is plotted versus the initial outer gimbal angle. This plot is then searched for local maxima. With a local maximum located, the outer gimbal angle is discretized over an interval encompassing the maximum with a grid spacing an order of magnitude smaller than the previous grid spacing. This process is repeated until such time as no local maxima are found, or a sufficiently small grid spacing of 0.001 degrees is reached. In the case where multiple local maxima are found on the same interval, the largest local maximum is used.

For the second step, the initial outer gimbal angle found in the first step is used. The deceleration time is then discretized and the deceleration scenario is run for each value of time. This step then proceeds just as the first step, with successively smaller grid

spacings reaching a final grid spacing of 0.01 seconds. The velocity error produced by the worst-case initial gimbal angle and deceleration time is considered to be the global maximum velocity error.

It should be noted that it is not possible to prove that the value of velocity error obtained this way is the global maximum. The technique outlined above will only yield a global maximum when the error plots are smooth, which is not the case for this system. In fact, many sharp peaks have been observed. This lack of smoothness means that the largest local maximum may not be the global maximum, as the global maximum might fall between the values on the grid no matter how fine the spacing. However, with the very fine final grid spacing employed, there is high confidence that the global maximum obtained is at least very close to the true global maximum.

5.1.4 The Plots

The plots in the sections that follow will be one of two main varieties. First, two-quadrant plots will be presented, showing maximum RSS gyro errors and peak lambda errors versus initial outer gimbal angle for angles in the ± 90 degree range. A four-quadrant plot would be for angles in the ± 180 degree range. However, due to symmetry in the system, the response in the 90 to 180 degree range would simply be the mirror image of the 0 to 90 degree response and likewise -180 to -90 would mirror -90 to 0. Thus, the smaller two-quadrant plots are used.

Two-quadrant plots for both the null-inner and null-middle configurations are presented. Also, in the case of the LQR controller, two-quadrant plots for multiple values of theta dot gain are shown. These plots tend to be time intensive to produce, as many computer simulations are required to achieve a significant number of data points. To reduce as much as possible the amount of time required to run these simulations, all two-quadrant plots utilized the coast scenario, thus eliminating the deceleration time variable. Also,

without decelerating the system back to zero angular velocity, velocity error will not be reported.

In addition to two-quadrant plots, several single-maneuver plots are presented below. These plots show examples of velocity, gyro, and lambda error transients, as well as gimbal angle motions, during a single coast or deceleration maneuver for a given initial gimbal angle configuration. In all cases, the initial gimbal angles are given in degrees. Single-maneuver plots of some of the worst-case examples found by the searching technique outlined in section 5.1.3 are presented.

5.2 The Classical Control Approach

Following are the results for the classical control approach. Plots for lambda errors and gyro errors, and tables for velocity errors and torque commands are included.

5.2.1 Lambda Errors

The first set of plots is of lambda errors. Recall that lambda has no units which is apparent from its definition in (3.3.1).
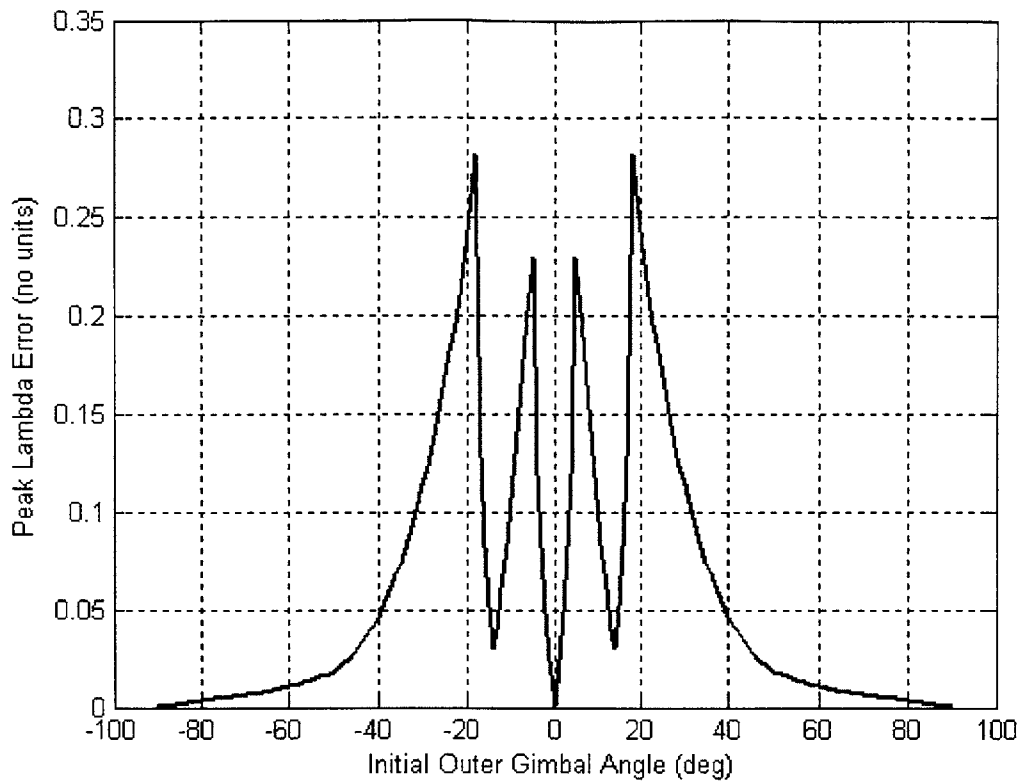
Figure 5.2.1 - Two-quadrant plot of peak lambda errors for the null-inner configuration.

The largest values of lambda in Figure 5.2.1 above, while not approaching a gimbal lock value of 1, are greater than 0.25. The figure is symmetric about zero, with lambda errors peaking between -20 and 20 degrees and falling off as they approach -90 or 90 degrees. The symmetry is to be expected, as the gimbals are spherical.

In Figure 5.2.1, the largest values occur during missile maneuvers requiring large gimbal motions. To demonstrate this, the following single maneuver plots are presented.
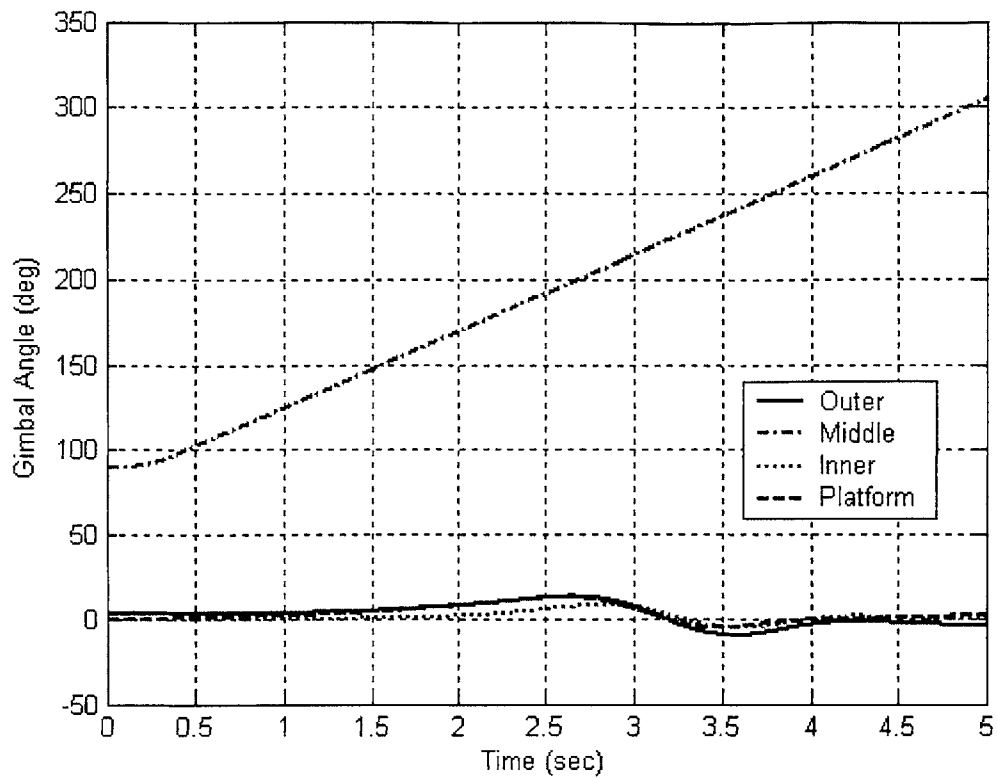
Figure 5.2.2 - Single-maneuver plot of gimbal angle transients with initial gimbal angles [3 90 0 0].

The single-maneuver plot in Figure 5.2.2 shows the null-inner configuration with an initial outer gimbal angle of 3 degrees. It can be seen in this case that the middle gimbal angle follows the input pitch motion and the remaining three gimbals move only slightly.
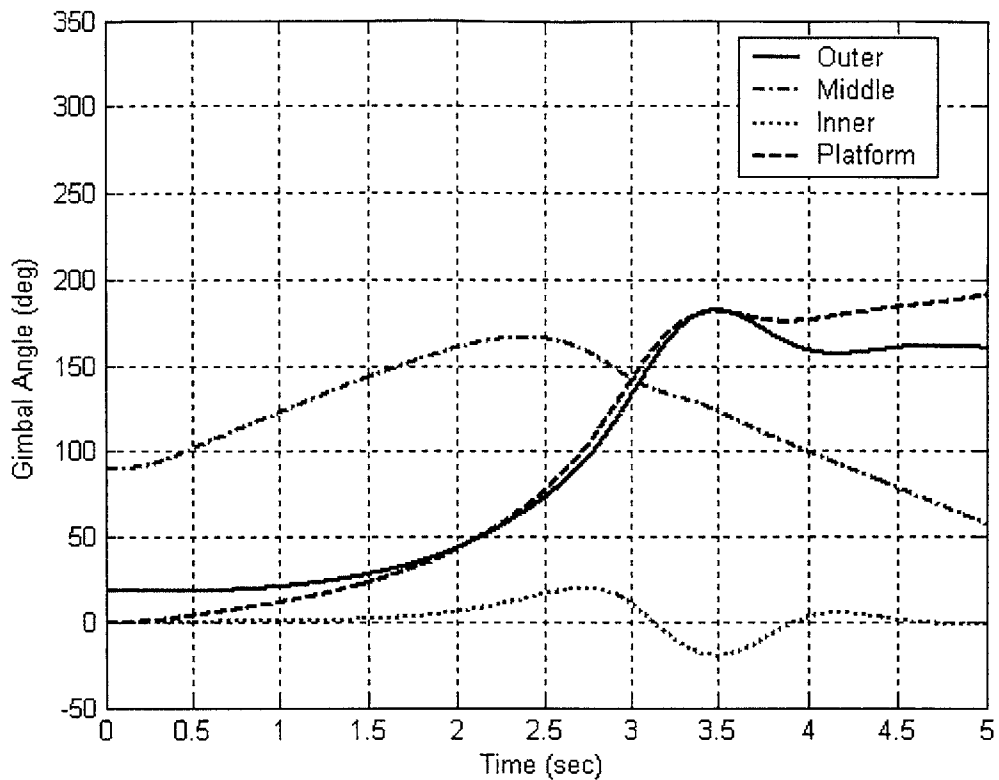
Figure 5.2.3 - Single-maneuver plot of gimbal angle transients with initial gimbal angles [18 90 0 0].

Contrast Figure 5.2.2 above with Figure 5.2.3. Here, for the null-inner configuration and an initial outer gimbal angle of 18 degrees, the outer and platform gimbals must move significantly in a short period of time. This large gimbal motion leads to large lambda errors and, as will be seen below, large gyro errors and hence the sharp peaks found in Figure 5.2.1 above.
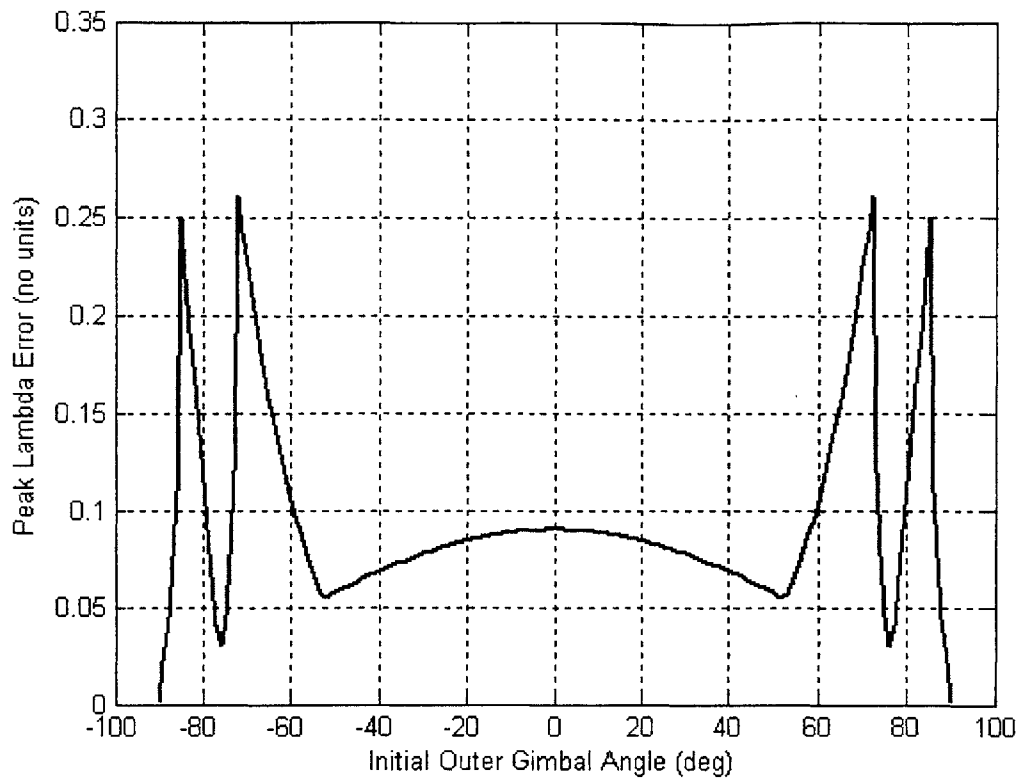
Figure 5.2.4 - Two-quadrant plot of peak lambda errors for the null-middle configuration.

Notice in Figure 5.2.4 that for the null-middle configuration the lambda errors, while still symmetric about zero, now peak between -70 and -90 degrees and 70 and 90 degrees. In the case of the null-middle configurations, the necessarily large gimbal motions as explained in Figure 5.2.3 above are now shifted to ± 90 degrees from zero degrees. It is also the case that, when comparing the null-middle configuration to the null-inner configuration in Figure 5.2.1, the overall maximum lambda errors are similar in magnitude.

5.2.2 Gyro Errors

The second set of plots is of gyro errors. These two-quadrant plots are also for the null-inner and null-middle configurations. The RSS gyro errors are given in units of bits. From (2.2.14), it can be recalled that the conversion from radians to bits is as follows.

$$1 \ gyro \ bit = 1.75 \times 10^{-6} \ radians \qquad\qquad (5.2.1)$$

See section 2.2.3 for more discussion about gyro bits.
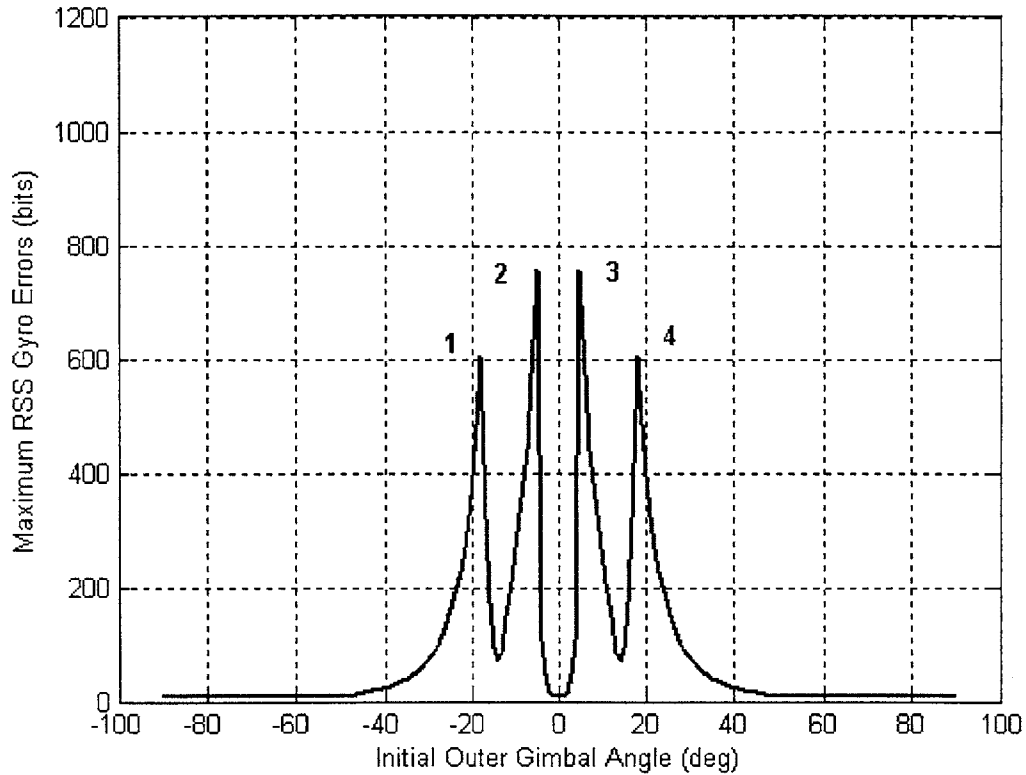
Figure 5.2.5 - Two-quadrant plot of maximum RSS gyro errors for the null-inner configuration.

In Figure 5.2.5 above, the symmetry about zero is again present. Also, the initial outer angles leading to the largest maximum RSS gyro errors are remarkably similar to those leading to the worst peak lambda errors. This is likely due to the fact that as lambda error increases, the platform loses controllability to the point that at the gimbal lock condition of lambda error equal to one, the platform is uncontrollable. Thus, as lambda error increases, larger platform motions and hence larger gyro errors are possible.
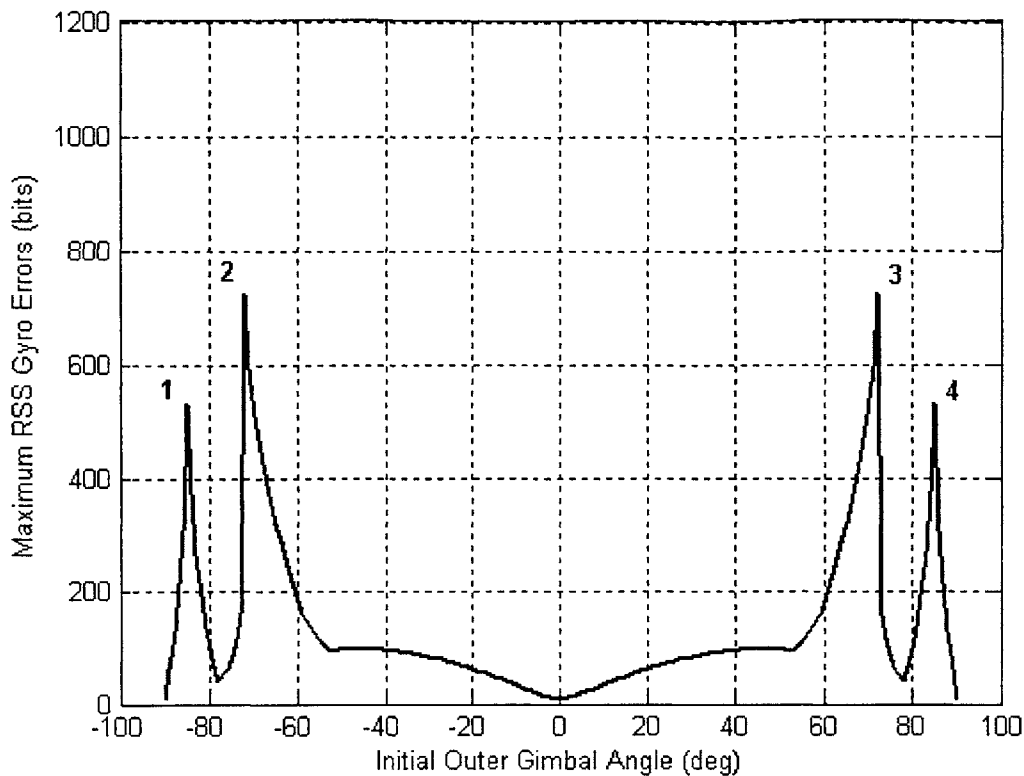
Figure 5.2.6 - Two-quadrant plot of maximum RSS gyro errors for the null-middle configuration.

Once again, in Figure 5.2.6, the maxima appear to be at the same locations as for the lambda error plot in Figure 5.2.4. However, the area between -45 and 45 degrees is of interest. Here, in the lambda error plot a hill is observed, but in the gyro error plot there is a valley. This is likely due to the fact that, for the small lambda errors observed over this interval, the controller maintained small gyro errors rather than compromising the gyro errors to further reduce the lambda errors. This is an excellent example of the fact that, while large lambda errors allow for the possibility of large gyro errors as discussed above, the observation of large lambda errors does not guarantee large gyro errors.

5.2.3 Velocity Errors and Peak Torques

With the coast scenarios complete, attention is turned to the deceleration scenarios. Recall from section 5.1.4 that the two-quadrant plots above utilize only the coast

scenario, neglecting the deceleration. As described in section 5.1.3, maximum values of steady-state RSS velocity errors are found by searching the local maxima, labeled in Figure 5.2.5 and Figure 5.2.6 above, and including the deceleration time. The following tables present results from this searching. Velocity errors are given in units of feet per second in the table and in the plots which follow.

Table 5-1 Velocity errors for the classical controller in the null-inner configuration

Maximum	Initial OG Angle (deg)	Deceleration Time (sec)	Steady-State Velocity Error (ft/sec)	Maximum RSS Gyro Error (bits)	Peak Lambda (no units)
1	-17.786	3.97	0.0159	638.0	0.2865
2	-4.856	3.56	0.0106	803.4	0.2329
3	4.856	3.56	0.0106	803.4	0.2329
4	17.785	3.97	0.0159	638.7	0.2866

Table 5-2 Velocity errors for the classical controller in the null-middle configuration

Maximum	Initial OG Angle (deg)	Deceleration Time (sec)	Steady-State Velocity Error (ft/sec)	Maximum RSS Gyro Error (bits)	Peak Lambda (no units)
1	-85.072	3.65	0.0068	783.3	0.1981
2	-72.104	3.48	0.0093	847.3	0.2630
3	72.104	3.49	0.0093	848.1	0.2630
4	85.074	3.64	0.0068	783.6	0.1981

Table 5-1 and Table 5-2 above contain the worst-case velocity errors discovered for the classical control design with the null-inner and null-middle configurations respectively. The maxima numbers correspond to the labels in Figure 5.2.5 and Figure 5.2.6. As was mentioned in section 5.1.3, none of these cases can be considered the absolute global maximum. Instead, they will be used primarily for comparison with the LQR control design. It is also interesting to observe that in the cases in Table 5-1, the largest gyro errors do not correspond to the largest velocity errors as was discussed in section 5.1.2.

Table 5-3 Peak torques for the classical controller in the null-inner configuration

Maximum	Initial OG Angle (deg)	Deceleration Time (sec)	Peak OGTQ (bits)	Peak MGTQ (bits)	Peak OTC (bits)	Peak MTC (bits)
1	-17.786	3.97	1485.3	712.5	3120.7	624.8
2	-4.856	3.56	1211.5	1729.9	1722.3	2302.6
3	4.856	3.56	1214.1	1729.7	1723.6	2301.9
4	17.785	3.97	1486.0	707.2	3120.2	625.2

Table 5-4 Peak torques for the classical controller in the null-middle configuration

Maximum	Initial OG Angle (deg)	Deceleration Time (sec)	Peak OGTQ (bits)	Peak MGTQ (bits)	Peak OTC (bits)	Peak MTC (bits)
1	-85.072	3.65	1074.7	1481.7	1850.7	2001.2
2	-72.104	3.48	1358.5	1744.8	1984.7	2316.9
3	72.104	3.49	1359.2	1744.6	1983.2	2317.1
4	85.074	3.64	1074.9	1481.3	1851.5	2000.8

Table 5-3 and Table 5-4 above give the values for peak torques in motor torque bits for the same maneuvers as outlined in Table 5-1 and Table 5-2. Both the total torques and the redundant torques are given, separated into the outer and middle torque motor components. In general, the cases with higher gyro errors also have higher torque commands as a consequence of attempting to eliminate the gyro error. Also, it should be noted that, as discussed in section 2.2.2, the torque motors have a range of ± 11,029 bits, so all of the torque commands in Table 5-3 and Table 5-4 are well below the saturation point of the motors.

Presented below are three single-maneuver plots from maximum three in Table 5-1 above. These plots show the velocity, gyro, and lambda error transients over the five

second interval of the deceleration maneuver. Similar plots, although not presented here, were produced for the remaining maxima.
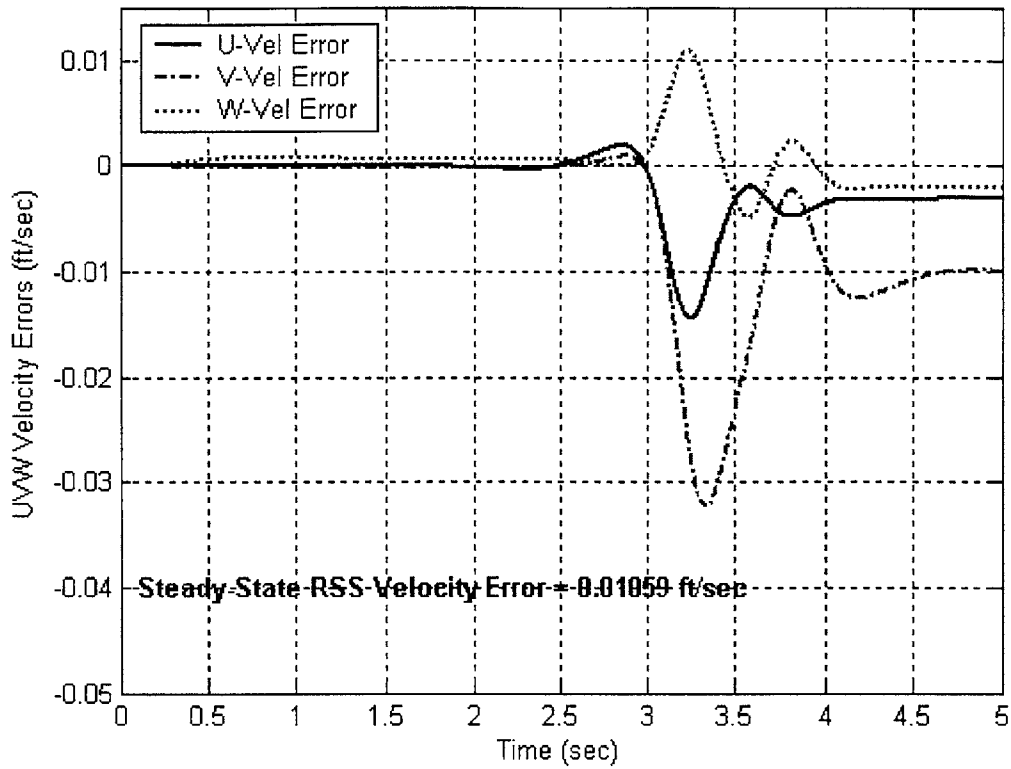
Figure 5.2.7 - Single-maneuver plot of velocity error transient with initial gimbal angles [4.856 90 0 0].
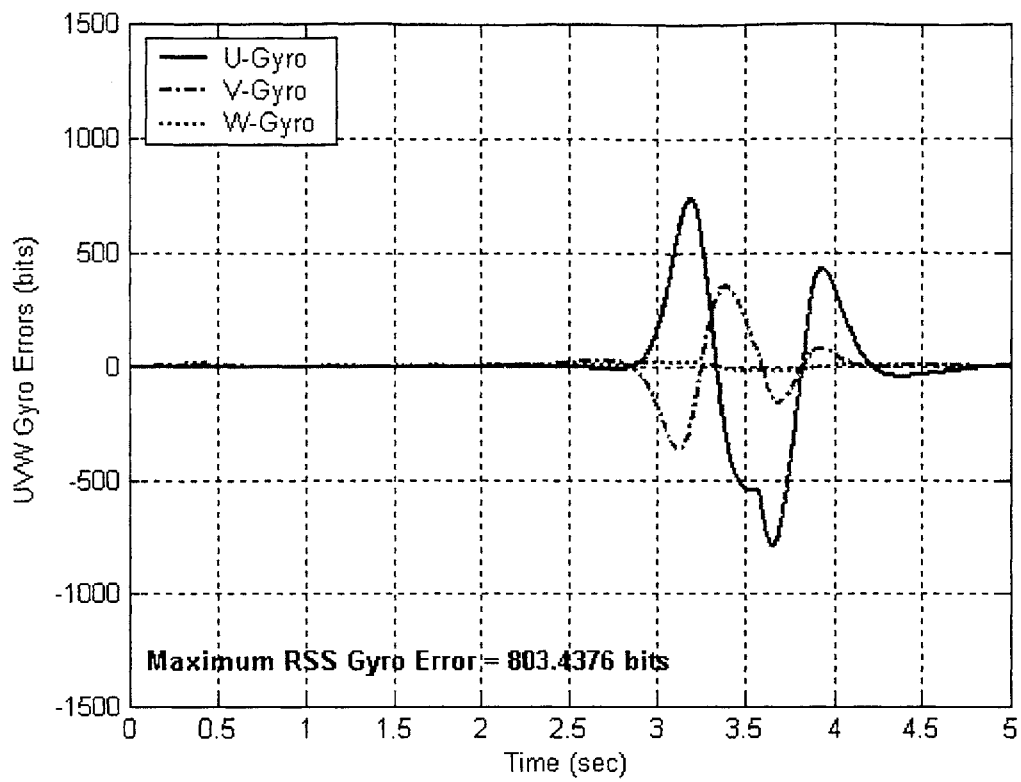
Figure 5.2.8 - Single-maneuver plot of gyro error transient with initial gimbal angles [4.856 90 0 0].
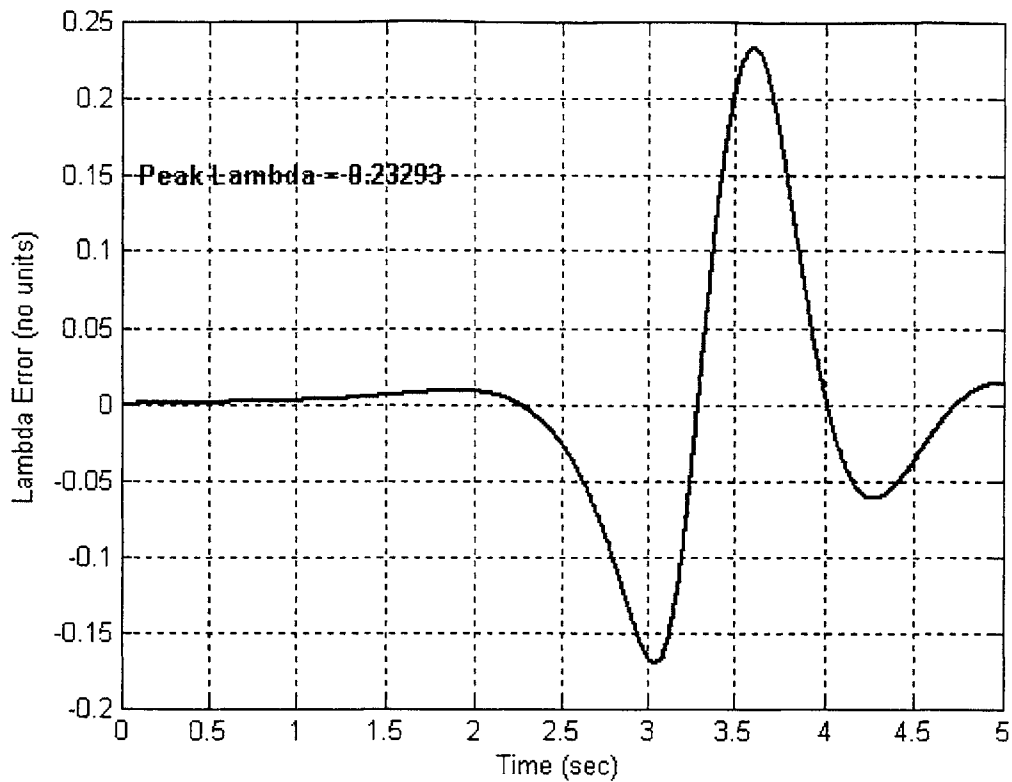
Figure 5.2.9 - Single-maneuver plot of lambda error transient with initial gimbal angles [4.856 90 0 0].

5.3 The Pseudo-Optimal Control Approach

The results for the pseudo-optimal control approach are presented below. Once again, plots for lambda errors and gyro errors, and tables for velocity errors and torque commands are included. In addition, plots representing different values of theta dot gain, a design parameter discussed in section 4.4.3 and given by (4.4.3), are shown. A discussion of how to choose the theta dot gain is also included.

5.3.1 Lambda Errors

The first plots presented are of the lambda errors. Two-quadrant plots for both the null-inner and null-middle configurations are below.
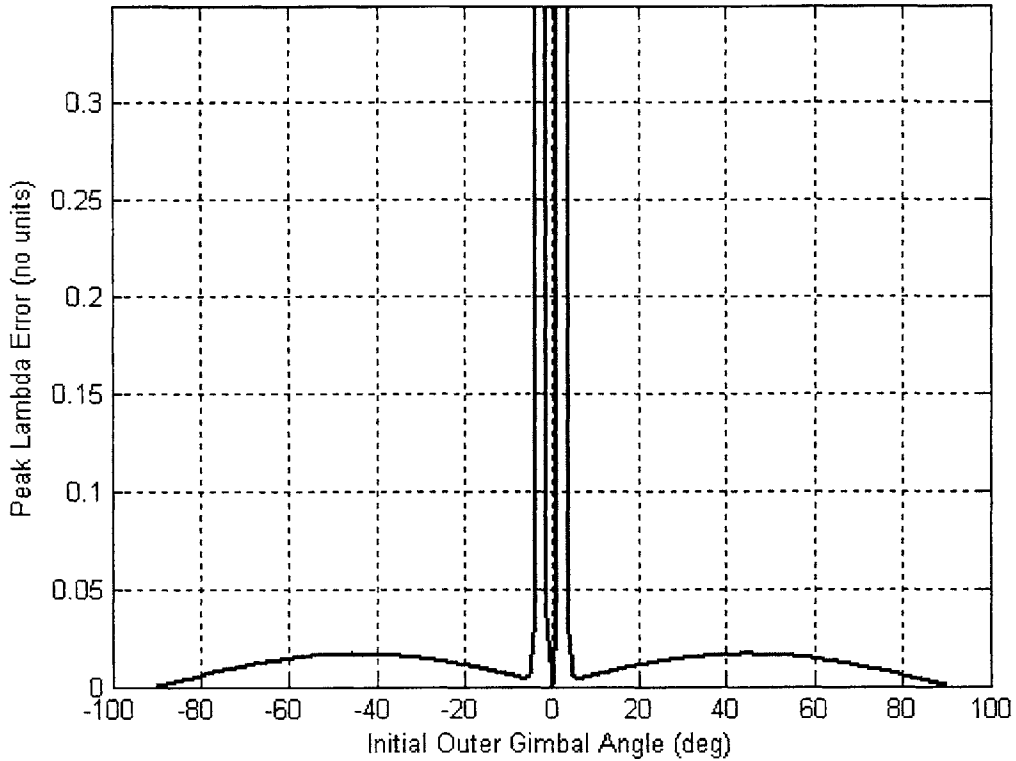
Figure 5.3.1 - Two-quadrant plot of peak lambda errors for the null-inner configuration with a theta dot gain of 25.

Figure 5.3.1 can be compared with the classical controller performance in Figure 5.2.1. Here, the LQR controller is better in the majority of cases, with the exception of initial outer gimbal angles in the ± 5 degree range, where the lambda error exceeds the maximum value in the figure. It is interesting to note that both the classical and LQR controllers have difficulty with initial outer gimbal angles close to zero.
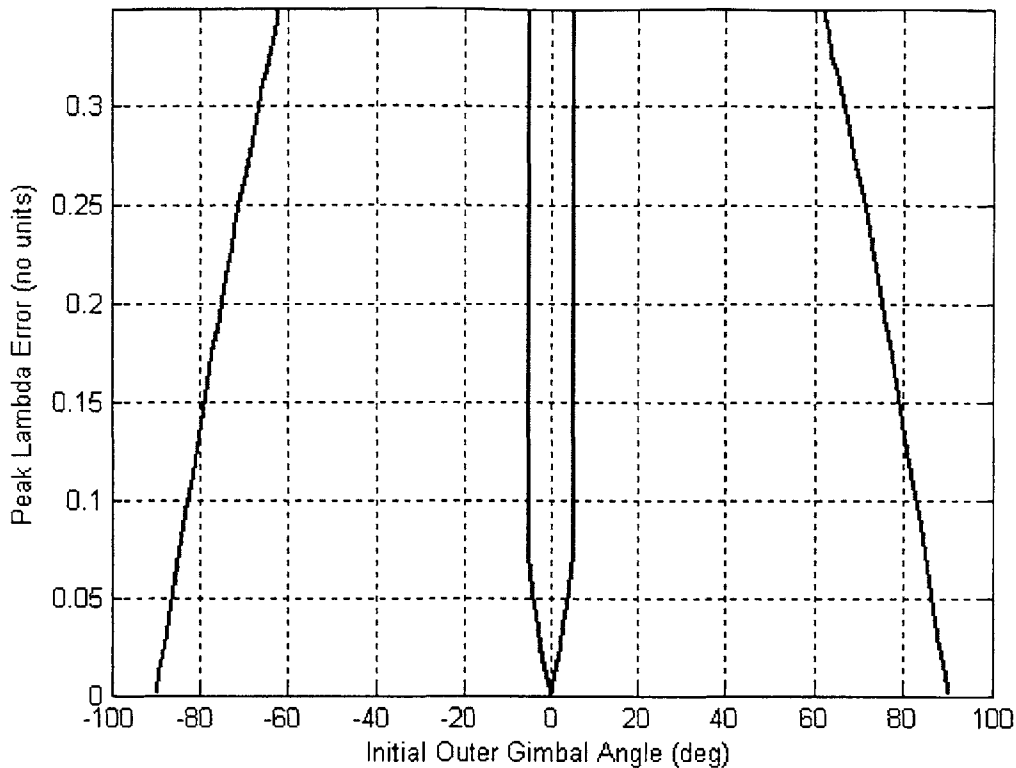
Figure 5.3.2 - Two-quadrant plot of peak lambda errors for the null-inner configuration with a theta dot gain of 0.001.

As an alternative, consider Figure 5.3.2, which can also be compared to the classical controller in Figure 5.2.1. With a very small value for the theta dot gain, the rate errors are essentially neglected in the optimal controller. Here, the effect is that in nearly every case, the optimal controller in Figure 5.3.2 performs very poorly in comparison with the classical controller in Figure 5.2.1 with the main exception being the initial outer gimbal angles in the range of ± 5 degrees. Very fortunately, this acceptable performance range corresponds nicely with the unacceptable range in Figure 5.3.1 above. This naturally suggests a solution would be to combine the two controllers into a single controller with a switching theta dot gain.

Figure 5.3.3 - Two-quadrant plot of peak lambda errors for the null-inner configuration with a switching theta dot gain.

Figure 5.3.3 shows the results of switching the theta dot gain based on the initial outer gimbal angle. When comparing this with Figure 5.2.1, it is apparent that the LQR controller either equals or reduces the lambda error in nearly every case. This is an encouraging result, as one of the aims of the optimal control design is to minimize the peak lambda error.

Despite these positive results, there are some further questions pertaining to this LQR controller which employs a changing theta dot gain. The first question is how to determine when to use each of the different theta dot gains. At first, the answer seems simple, as explained in the figures above. For initial outer gimbal angles between ± 5 degrees, a theta dot gain of 0.001 should be used. For other outer gimbal angles, a gain of 25 should be used. However, the problem here is how to determine the initial outer gimbal angle a priori.

In the case of the fixed maneuvers tested and presented here, the initial outer gimbal angle is an input to the system and is chosen by the user. However, in an actual missile flight lasting much longer than five seconds and possibly containing several maneuvers, the initial conditions at the start of a maneuver are unclear. Because of this, it is necessary to look at single-maneuver plots showing the gimbal motion for two of the different scenarios listed above to help explain a better method for choosing the theta dot gain.
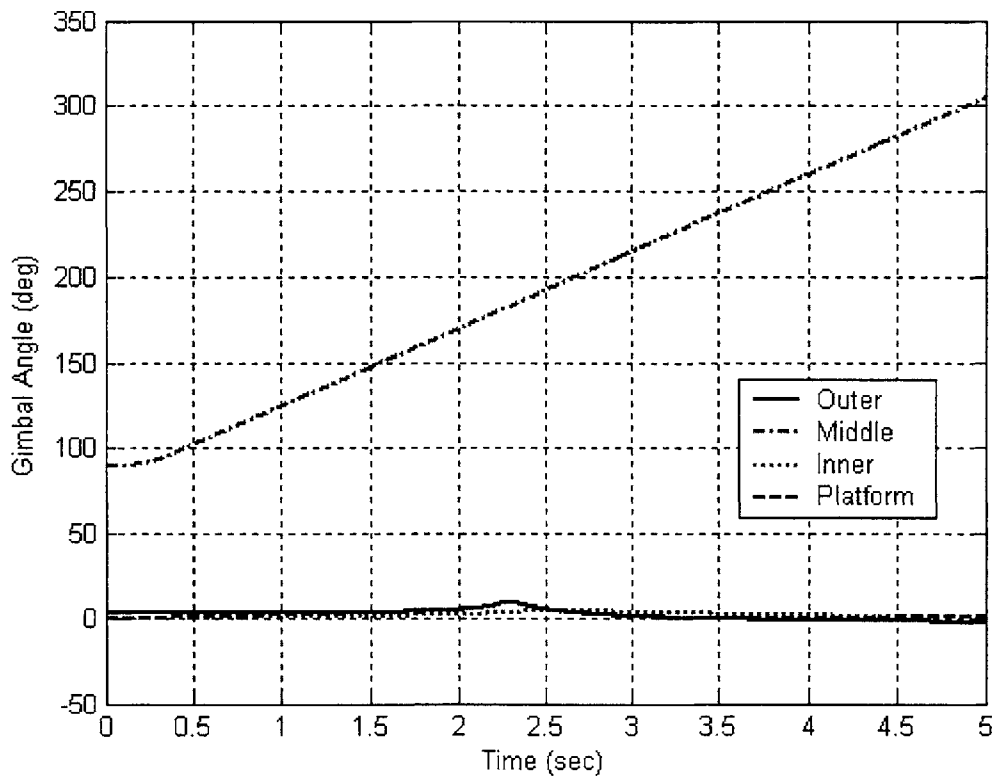
Figure 5.3.4 - Single-maneuver plot of gimbal angle transients with initial gimbal angles [3 90 0 0].

Figure 5.3.4 shows the gimbal motions typical of a maneuver where the initial outer gimbal angle is close to zero. Notice the majority of the pitch motion is captured by the middle gimbal angle, with the remaining three angles only displaying a very slight motion. This is for the case where the theta dot gain is 0.001. Also note that, when

compared to the classical controller in Figure 5.2.2, the LQR controller prevents noticeably more of the motion by the outer, inner, and platform gimbals.
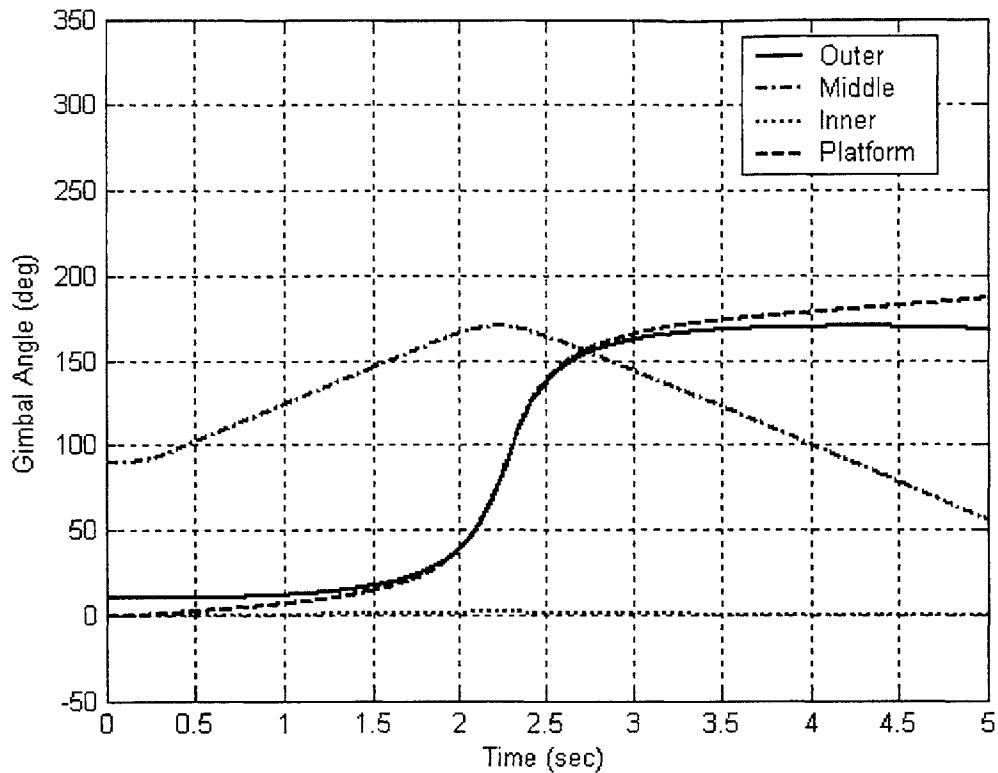
Figure 5.3.5 - Single-maneuver plot of gimbal angle transients with initial gimbal angles [10 90 0 0].

Figure 5.3.5 above can be contrasted with Figure 5.3.4. In Figure 5.3.5, while the middle gimbal still accounts for the majority of the pitch motion, the outer and platform gimbals move extensively in a short period of time. This counter-rotation of gimbals allows for near zero lambda error throughout the maneuver. This is for the case where the theta dot gain is 25. A similar maneuver for the classical controller, found in Figure 5.2.3, once again shows the superiority of the LQR controller.

In contrasting Figure 5.3.4 and Figure 5.3.5, the main difference is the amount of motion the outer and platform gimbals endure during a small time frame. The conclusion is that for cases where the outer gimbal must make a large motion in a short period of time, the

rate as well as the position is important, and hence a large theta dot gain is necessary. For cases where the outer gimbal makes a very small motion, the rate is not critical, and hence a small theta dot gain. By choosing a theta dot gain based on the size of the outer gimbal motion required, instead of simply the initial condition, a controller which is valid over a wider range of conditions can be produced.

As with the classical controller, the null-middle configuration is also considered. These plots follow.
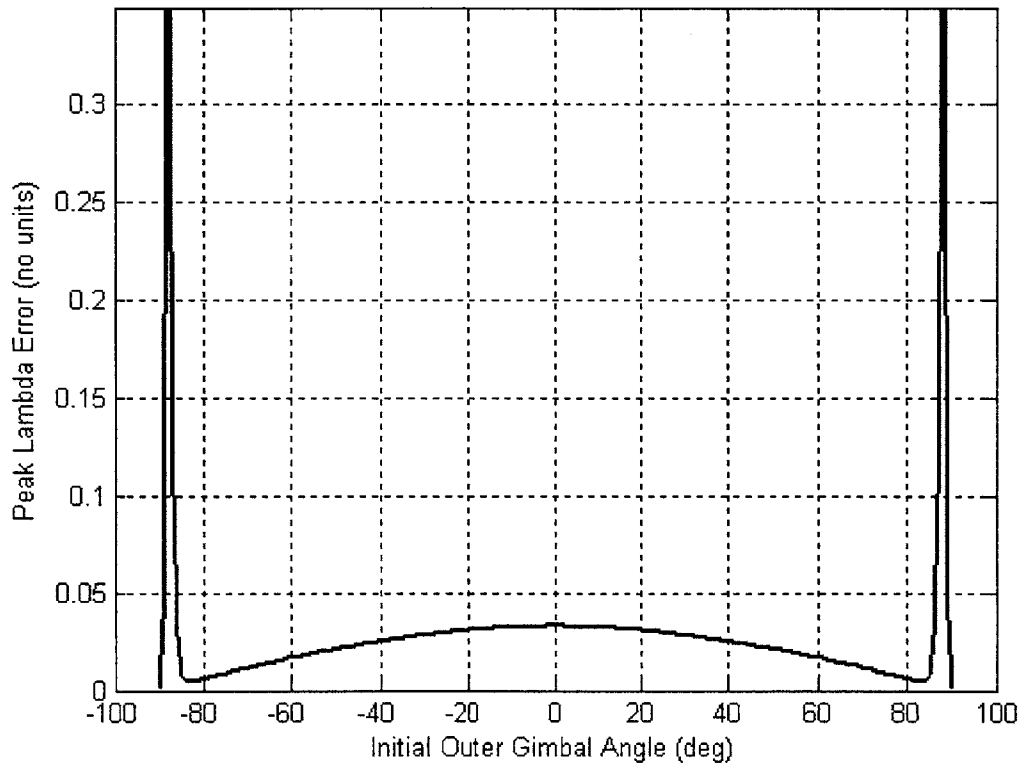
Figure 5.3.6 - Two-quadrant plot of peak lambda errors for the null-middle configuration with a theta dot gain of 25.

Figure 5.3.6 above can be compared with the classical controller in Figure 5.2.4. Here, with the inner angle starting at 90 degrees, the LQR controller has superior performance everywhere except in the -90 to -85 and 85 to 90 degree ranges. It is interesting to note that Figure 5.3.6 above appears very similar to Figure 5.3.1 with the poor performance

areas shifted by 90 degrees, just as in the case of the classical controller. In a similar fashion to the null-inner case, an attempt is made at eliminating these large peak lambda errors by varying the theta dot gain.
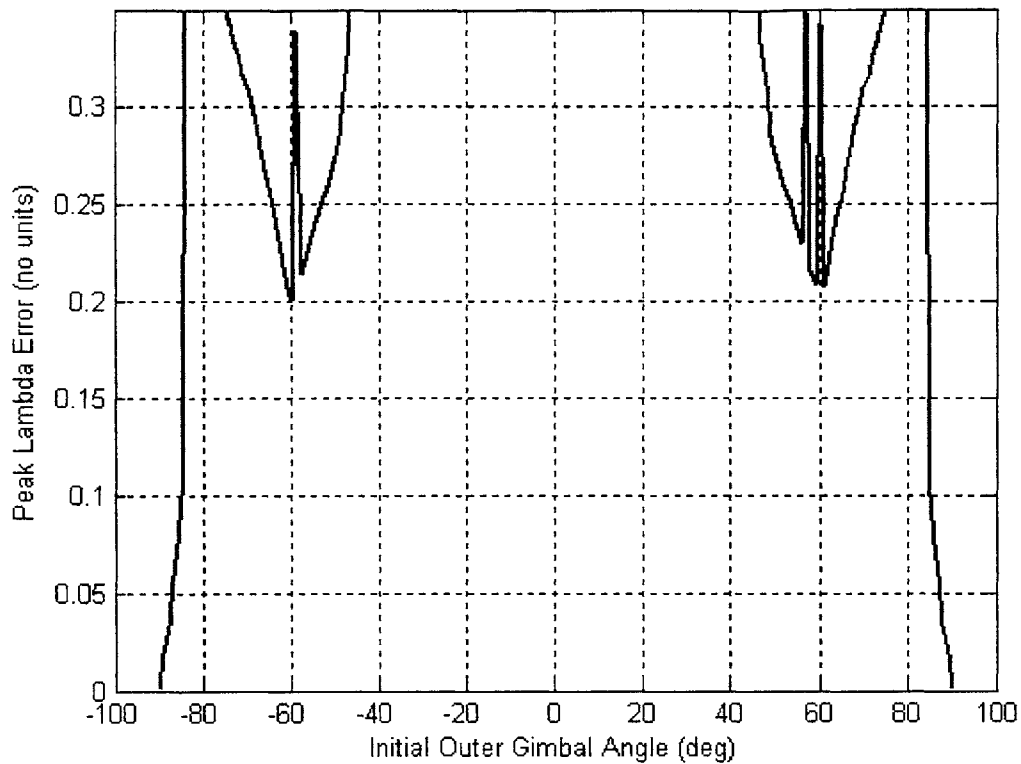
Figure 5.3.7 - Two-quadrant plot of peak lambda errors for the null-middle configuration with a theta dot gain of 0.001.

Figure 5.3.7 above is strictly worse that the classical controller in Figure 5.2.4, with the exception of the -90 to -85 and 85 to 90 degree ranges. Again, these correspond nicely with the areas of poor performance in Figure 5.3.6, so a controller utilizing a switching theta dot gain is again employed.
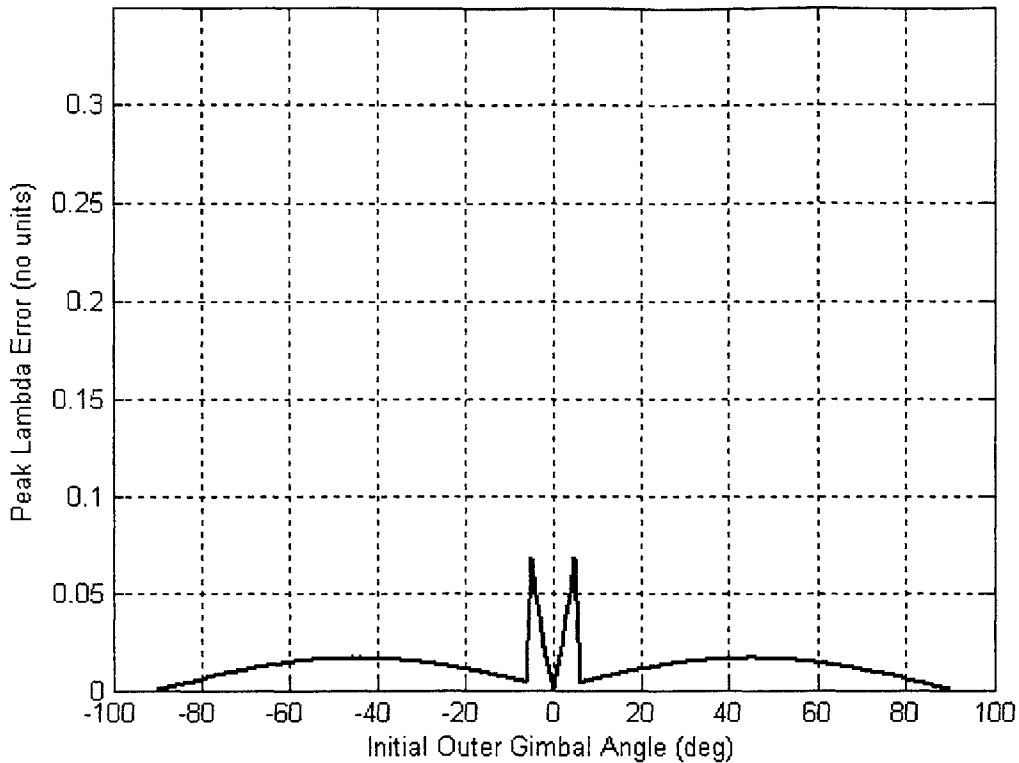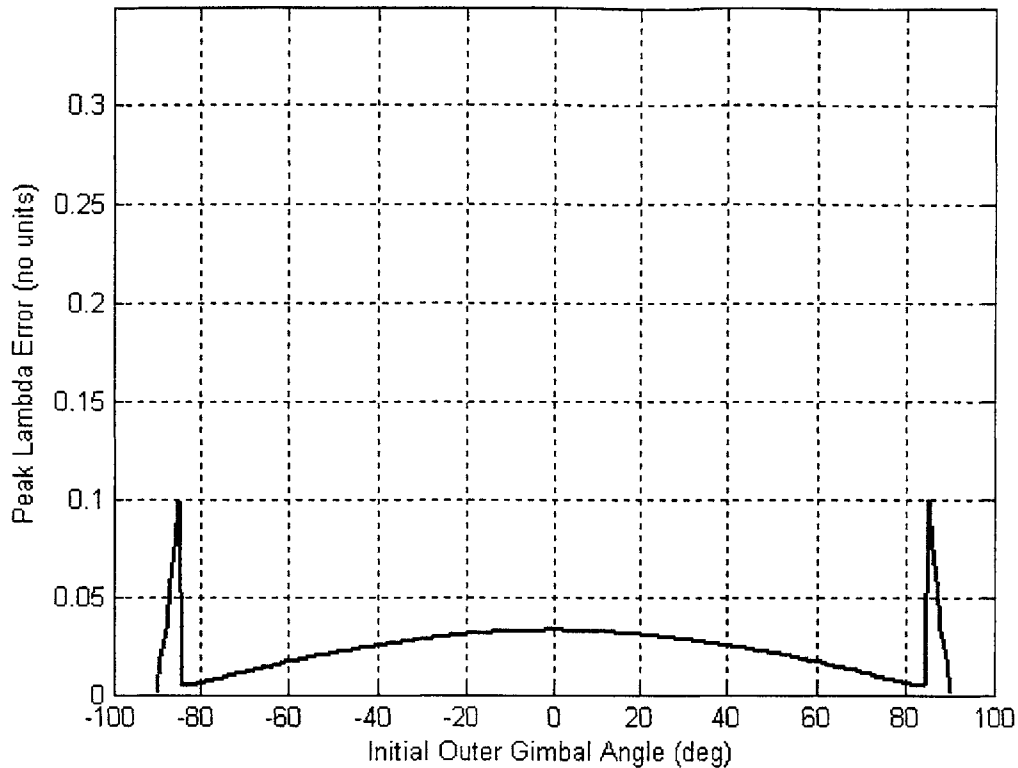
Figure 5.3.8 - Two-quadrant plot of peak lambda errors for the null-middle configuration with a switching theta dot gain.

Figure 5.3.8 shows very comparable results to Figure 5.3.3 and much smaller lambda errors than the classical controller in Figure 5.2.4. In Figure 5.3.8 above, the same technique is used as in Figure 5.3.3 for the case with an initial middle gimbal angle of 90; namely, for initial outer gimbal angles in the -90 to -85 and 85 to 90 degree ranges, a theta dot of 0.001 is used and for initial outer gimbal angles in the ± 85 degree range, a theta dot of 25 is used. Also, the same theory for the magnitude of gimbal motion as is discussed above holds true.

5.3.2 Gyro Errors

Peak RSS gyro errors are plotted versus initial outer gimbal angle, just as was done for the classical controller. Again, both the null-inner and null-middle configurations are

118

considered, and the coast maneuver is used throughout. Two-quadrant plots for two different values of theta dot gain are again presented.
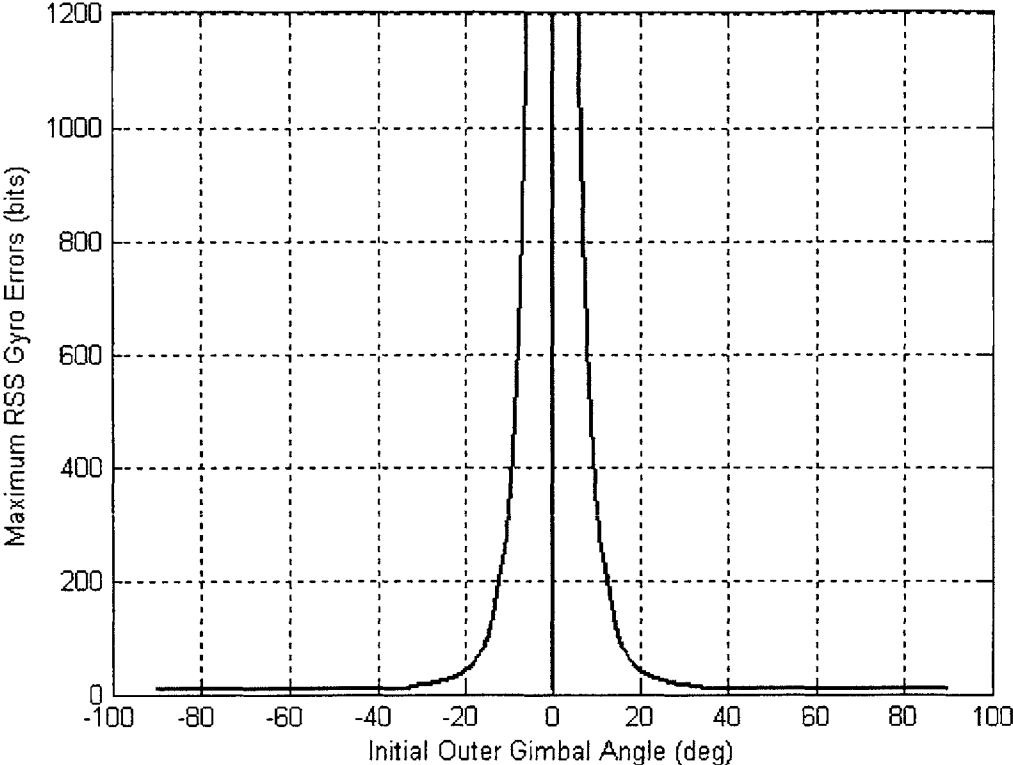
Figure 5.3.9 - Two-quadrant plot of maximum RSS gyro errors for the null-inner configuration with a theta dot gain of 25.

Consistent with the lambda errors in Figure 5.3.1, the worst gyro errors in Figure 5.3.9 above occur with initial outer gimbal angles in the ± 5 degree range.
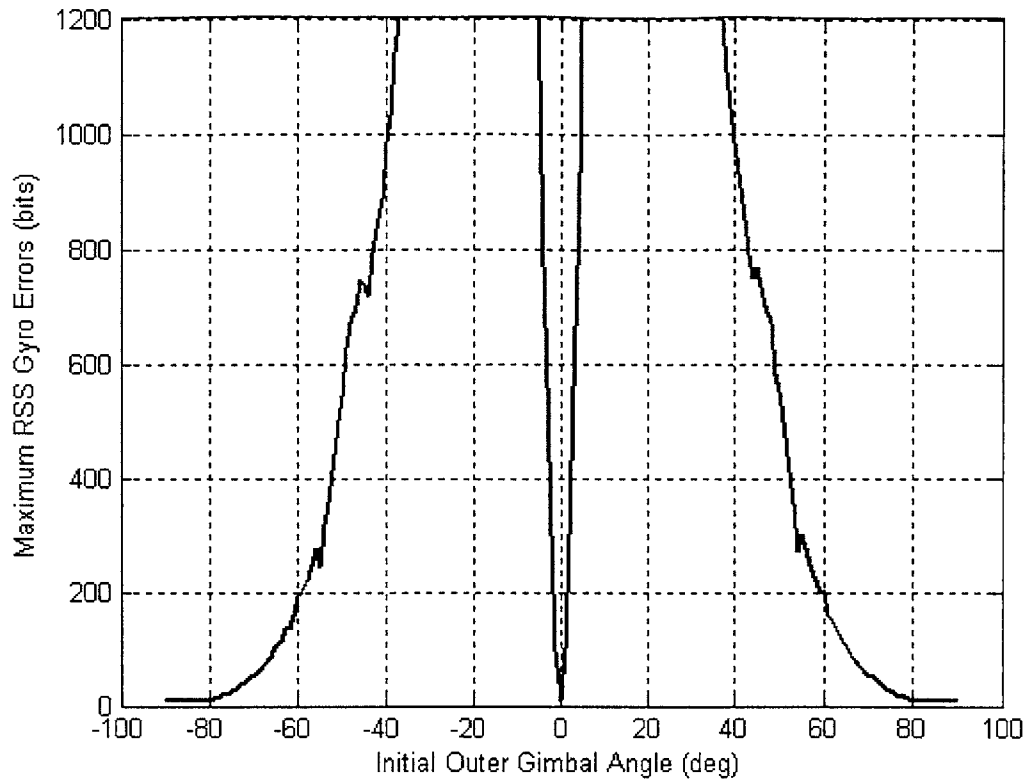
Figure 5.3.10 - Two-quadrant plot of maximum RSS gyro errors for the null-inner configuration with a theta dot gain of 0.001.

As before in Figure 5.3.2, the small theta dot gain improves performance in the ± 5 degree range as seen in Figure 5.3.10 above. Once again, this supports the idea of a changing theta dot gain, the results of which are presented below.
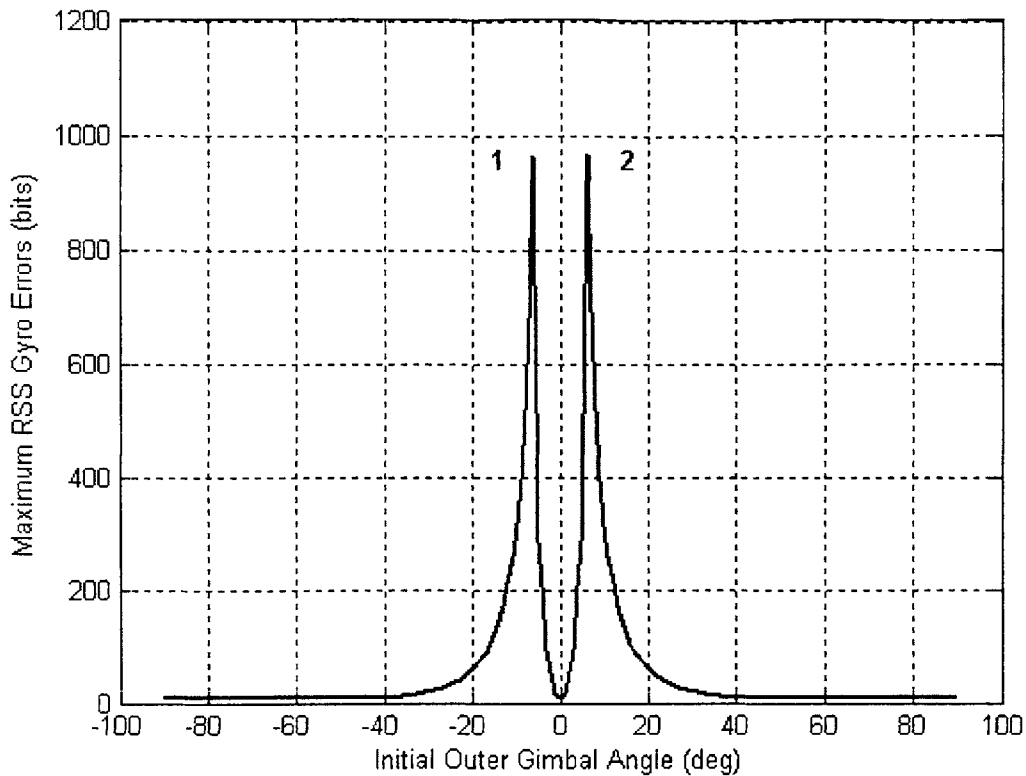
Figure 5.3.11 - Two-quadrant plot of maximum RSS gyro errors for the null-inner configuration with a switching theta dot gain.

In comparing Figure 5.3.11 above with the classical controller performance in Figure 5.2.5, favorable results are seen. Although the maxima in the LQR controller are higher, their number is reduced from four to two. Furthermore, the range of outer gimbal angles leading to large gyro errors is reduced from ± 20 degrees to ± 5 degrees. This represents substantial improvement in controller performance, especially when coupled with the greatly reduced lambda error already exhibited.

Finally, results are presented for the null-middle configuration.
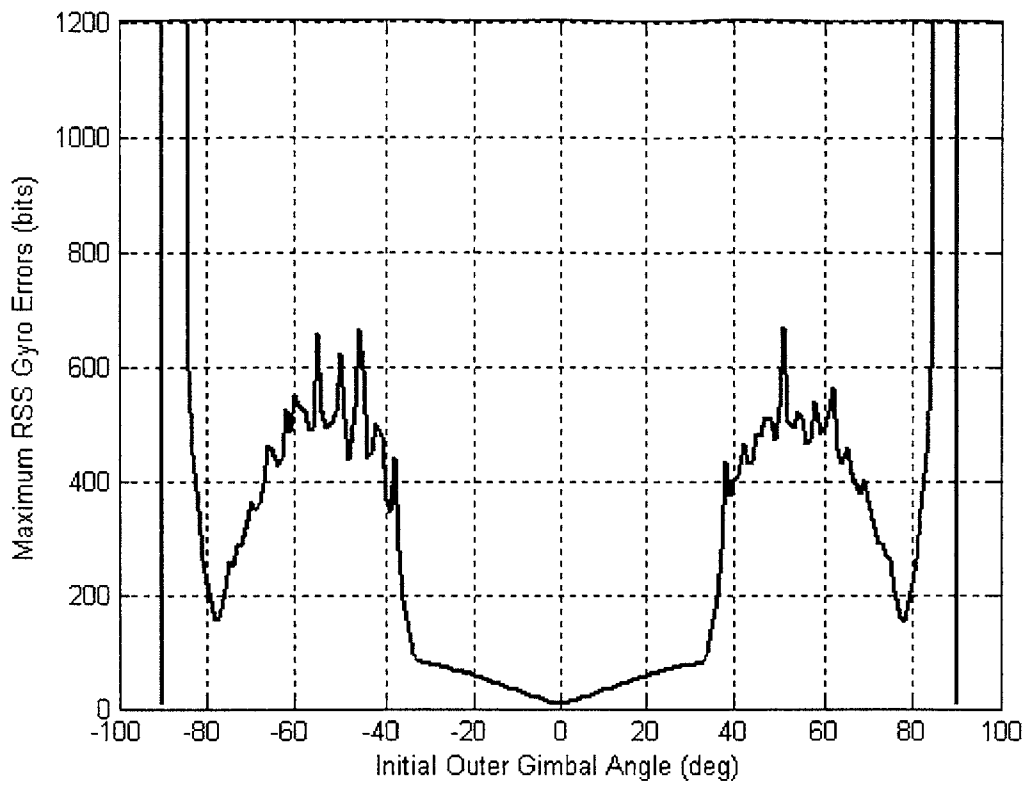
Figure 5.3.12 - Two-quadrant plot of maximum RSS gyro errors for the null-middle configuration with a theta dot gain of 25.

Above, Figure 5.3.12 shows gyro errors for a large theta dot gain. The maximum RSS gyro errors in the -90 to -85 and 85 to 90 degree ranges are particularly large.
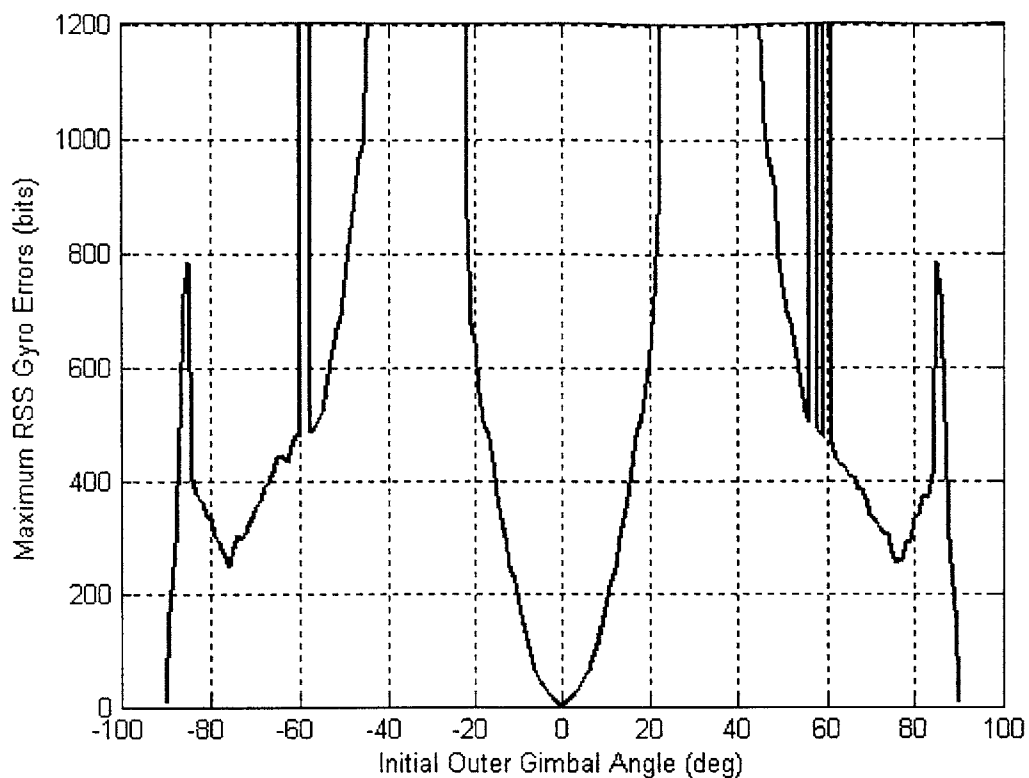
Figure 5.3.13 - Two-quadrant plot of maximum RSS gyro errors for the null-middle configuration with a theta dot gain of 0.001.

With a small theta dot gain in Figure 5.3.13, it can be seen that in the -90 to -85 and 85 to 90 degree ranges, a small theta dot gain performs better. Once again, this supports the idea of using two separate theta dot gains and switching between them.
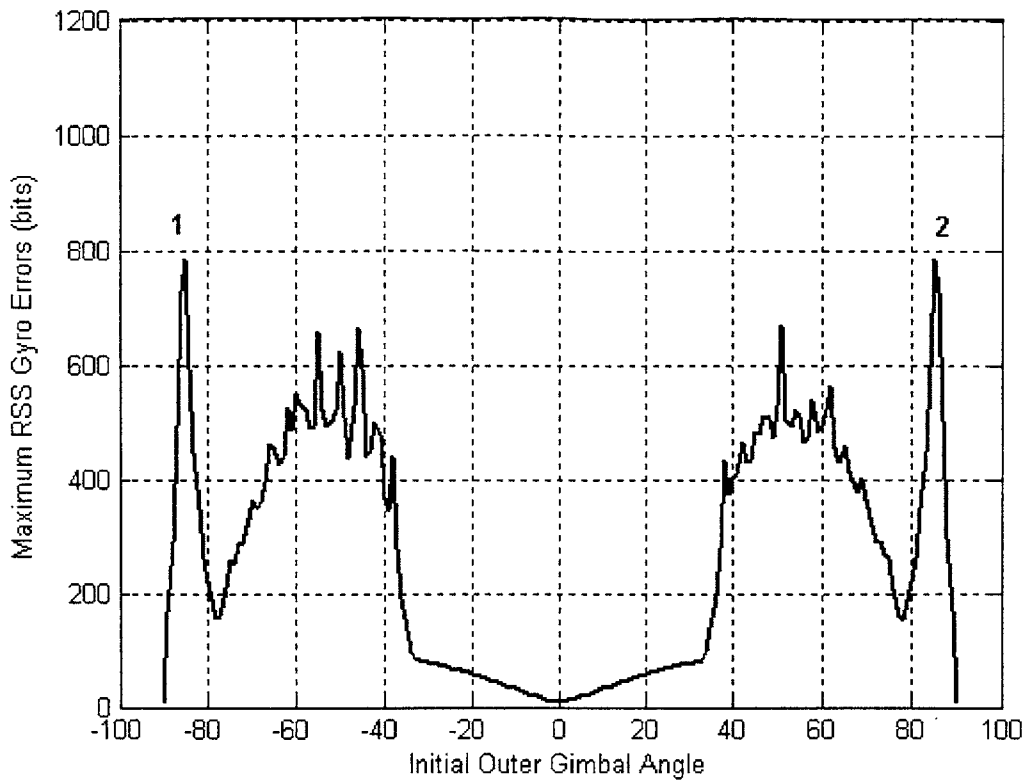
Figure 5.3.14 - Two-quadrant plot of maximum RSS gyro errors for the null-middle configuration with a switching theta dot gain.

In Figure 5.3.14 above, it can be seen that for initial outer gimbal angles in the ± 35 degree range, the response is similar to the classical controller in Figure 5.2.6. Elsewhere, the LQR controller is slightly inferior in some instances and superior in others. As can be observed from section 5.2.2, the null-middle configuration appears to be more difficult for the classical controller, so it is not altogether unexpected that the LQR controller will have inferior performance here as well.

5.3.3 Velocity Errors

With the coast scenarios complete for the LQR controller, attention is again turned to the deceleration scenarios. As explained in section 5.1.4, the two-quadrant plots above neglect the deceleration. The following tables present the results obtained by searching

for the maximum velocity errors, as described in section 5.1.3, for the maxima labeled in Figure 5.3.11 and Figure 5.3.14.

Table 5-5 Velocity errors for the LQR controller in the null-inner configuration

Maximum	Initial OG Angle (deg)	Deceleration Time (sec)	Steady-State Velocity Error (ft/sec)	Maximum RSS Gyro Error (bits)	Peak Lambda (no units)
1	-5.001	2.51	0.0041	1389.1	0.0051
2	5.001	2.51	0.0041	1389.2	0.0051

Table 5-6 Velocity errors for the LQR controller in the null-middle configuration

Maximum	Initial OG Angle (deg)	Deceleration Time (sec)	Steady-State Velocity Error (ft/sec)	Maximum RSS Gyro Error (bits)	Peak Lambda (no units)
1	-84.999	2.74	0.0075	1841.2	0.0074
2	84.999	2.74	0.0075	1820.2	0.0074

Table 5-5 and Table 5-6 show the maximum RSS gyro errors along with the maximum steady-state velocity errors and peak lambda errors obtained with the search technique described in section 5.1.3. The results are very favorable when compared with the classical controller in Table 5-1 and Table 5-2. The number of local RSS gyro error maxima have been reduced from four to two, as is apparent in Figure 5.3.11 and Figure 5.3.14. Although the gyro errors in Table 5-5 and Table 5-6 are higher than for the classical controller, the steady-state velocity errors have been greatly improved. In fact, the velocity errors in the null-inner case have been reduced to approximately one-fourth of the value of the largest velocity errors from the classical controller. This is a significant improvement, as keeping the velocity errors as small as possible is one of the goals of the optimal controller. Thus, the higher gyro errors generated by the LQR controller can be tolerated, as long as the velocity errors are smaller.

The lambda errors for the LQR controller in Table 5-5 represent a vast improvement when compared with the classical controller in Table 5-1. In fact, the lambda errors produced by the classical controller are more than 50 times larger than those for the LQR controller. This is also encouraging, as a second goal of the optimal controller is to minimize the lambda error. Thus, the main goals of the LQR controller have been accomplished.

Table 5-7 Peak torques for the LQR controller in the null-inner configuration

Maximum	Initial OG Angle (deg)	Deceleration Time (sec)	Peak OGTQ (bits)	Peak MGTQ (bits)	Peak OTC (bits)	Peak MTC (bits)
1	-5.001	2.51	11029.0	1301.7	11029.0	455.0
2	5.001	2.51	11029.0	1303.1	11029.0	454.6

Table 5-8 Peak torques for the LQR controller in the null-middle configuration

Maximum	Initial OG Angle (deg)	Deceleration Time (sec)	Peak OGTQ (bits)	Peak MGTQ (bits)	Peak OTC (bits)	Peak MTC (bits)
1	-84.999	2.74	11029.0	2464.8	11029.0	3700.9
2	84.999	2.74	11029.0	2465.4	11029.0	3683.4

In Table 5-7 and Table 5-8 above, the peak torque values are given. These values can be compared to the classical controller values in Table 5-3 and Table 5-4. It is immediately obvious that the peak outer motor torque commands generated by the LQR controller saturate the motor. This could potentially be a problem if the controller were to saturate the motors for very benign maneuvers. However, the maneuvers presented in Table 5-7 and Table 5-8 which saturate the motors are the worst-case maneuvers found and should be expected to create very large torque commands. Instead, it is surprising that the classical controller does not utilize more of the torque motor capacity to help in reducing the large lambda and velocity errors present in Table 5-1 and Table 5-2. Indeed, by

utilizing the full extent of the torque capacity, the LQR controller reduces the lambda and velocity errors significantly as seen in Table 5-5 and Table 5-6.

The following single-maneuver plots show the velocity, gyro and lambda error transients in the case of maximum two in Table 5-5. These figures can be compared to the classical controller in Figure 5.2.7, Figure 5.2.8, and Figure 5.2.9. Of interest are the much smaller lambda error and the narrower peak on the RSS gyro error, which leads to the smaller steady-state velocity error.
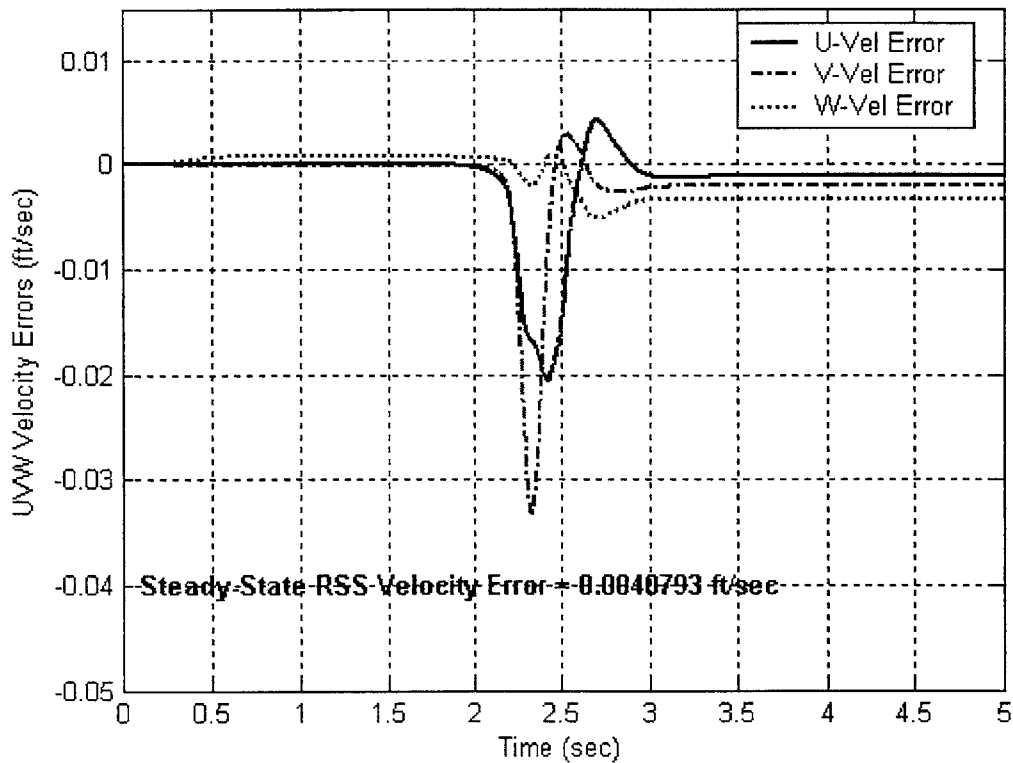
Figure 5.3.15 - Single-maneuver plot of velocity error transient with initial gimbal angles [5.001 90 0 0].
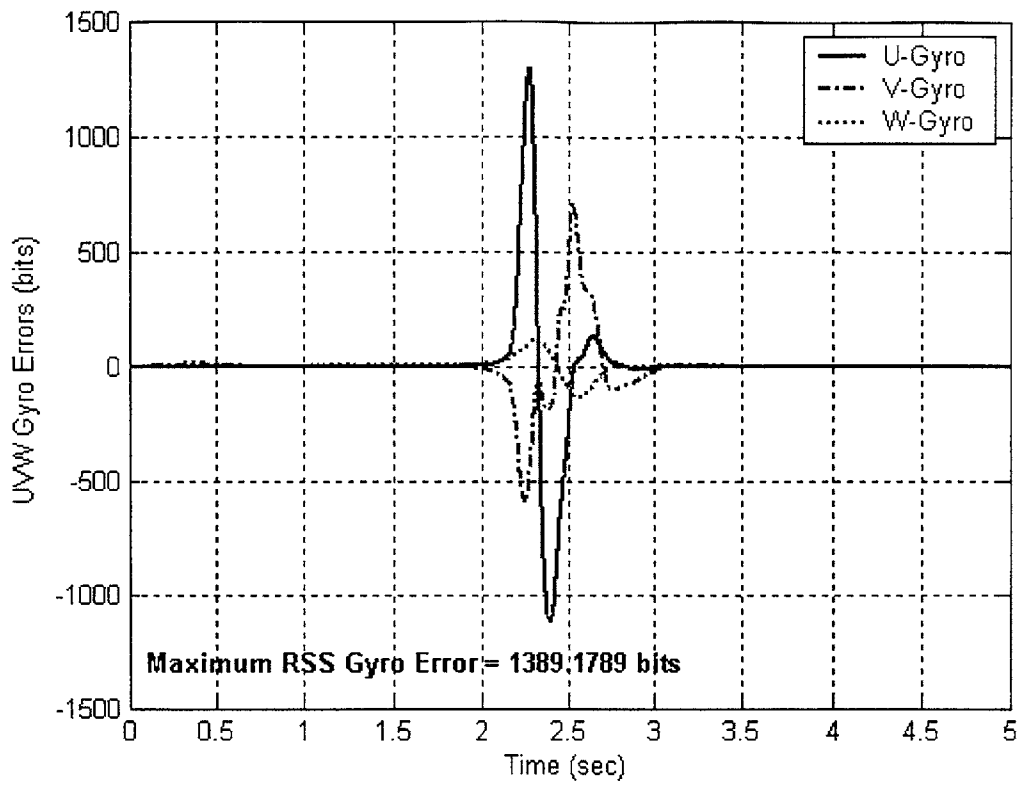
Figure 5.3.16 - Single-maneuver plot of gyro error transient with initial gimbal angles [5.001 90 0 0].
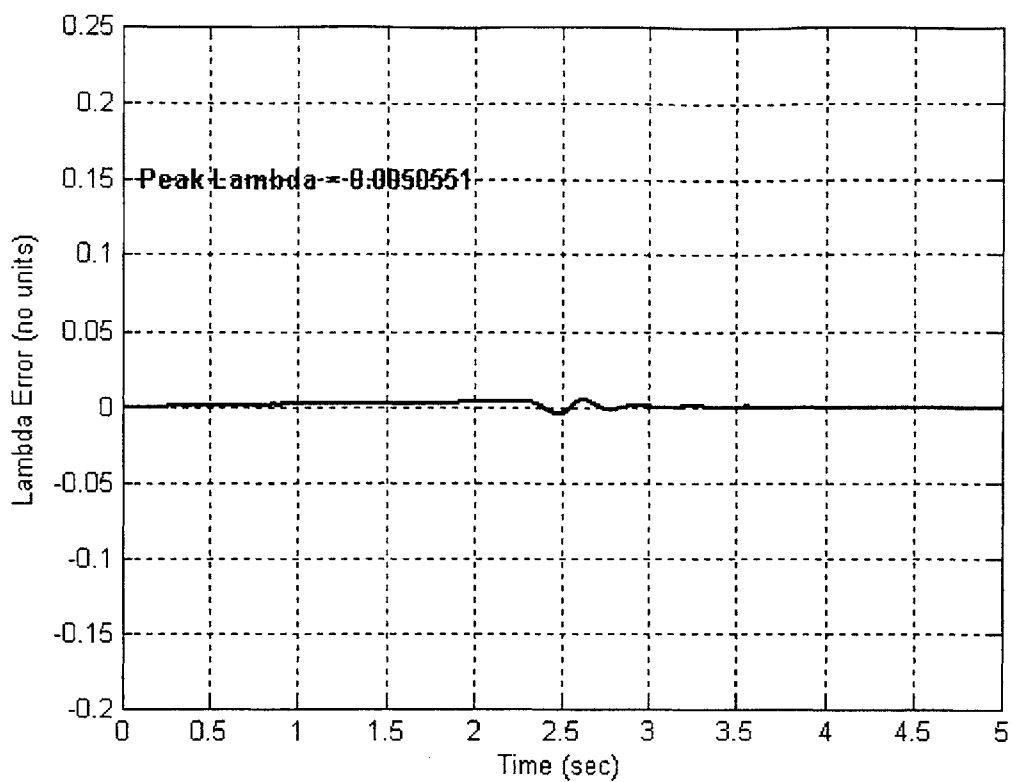
Figure 5.3.17 - Single-maneuver plot of lambda error transient with initial gimbal angles [5.001 90 0 0].

This page intentionally left blank.

Chapter 6

Conclusions and Future Work

6.1 Conclusions

When drawing conclusions based on the testing results presented in Chapter 5, it is first important to understand the limits on the scope of the conclusions which can be drawn. The parameters of the four gimbal system hardware components, modeled in software for the purposes of testing the controllers, by intention do not represent components of any real missile system. While the numerical values are chosen to be realistic, no conclusions as to the performance of any actual missile system should be drawn from the work herein presented. In addition, although values for metrics such as velocity errors and gyro errors have been given for the various controllers, these should in no way be interpreted as being indicative of any actual performance or accuracy characteristics of any real system, current or future. Indeed, the intent of this thesis is to demonstrate the superiority of the LQR control scheme as applied to the platform controller. To this end, the results of the two controllers are intended to be compared with one another, with the classical controller taken as the benchmark. It is in the relative performance of the controllers that the benefits of an LQR control scheme can be seen. By extension, it is believed that, should an LQR approach be implemented in a real gimbaled inertial navigation system, improvements of a similar order of magnitude would follow.

As demonstrated in Chapter 5, depending on the initial outer gimbal angle, the gimbal motion will vary greatly for a given case input motion scenario. Because this is the case,

it is necessary to consider many different initial conditions when evaluating controllers. Furthermore, it may not be the case that one controller is strictly better over every set of possible conditions. Consider the following example.
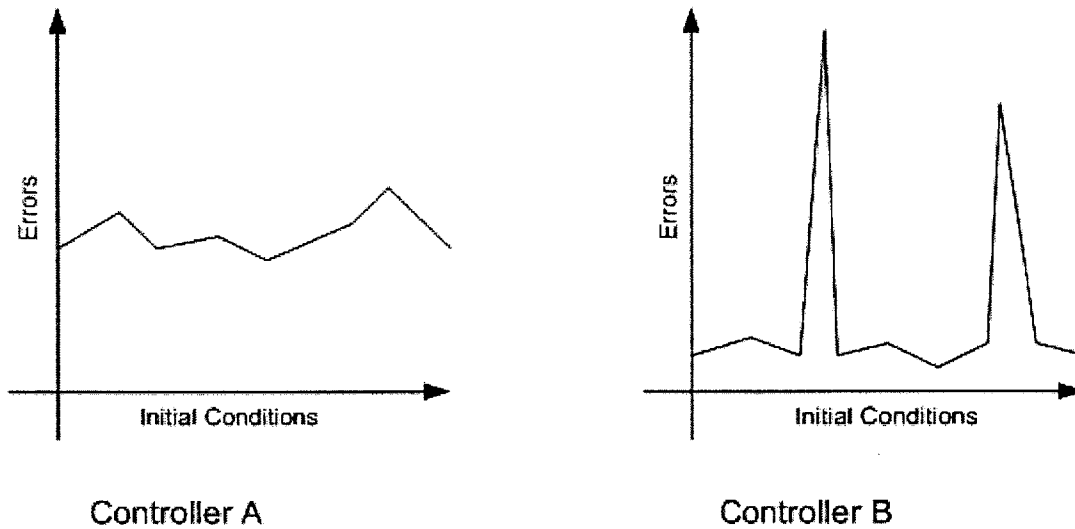
Figure 6.1.1 - Two controllers with contrasting error results.

In Figure 6.1.1 above, Controller A affords the smallest maximum error when considering all possible initial conditions. In contrast, for Controller B there exist some conditions leading to errors which are larger than for Controller A. However, Controller B is generally better over a large number of conditions.

Under circumstances such as are presented in Figure 6.1.1, two main options exist. First, it can be argued that Controller A which yields the minimum absolute error is superior. However, this leaves open the possibility that for a specific set of initial conditions, Controller A could actually be outperformed by Controller B.

Conversely, it is also possible to argue that Controller B, with worse performance for a few specific cases but which may, for example, have a smaller average maximum error over a large number of cases, is actually superior. This is due to the fact that, for a randomly chosen set of initial conditions, Controller B is very likely to perform better

than Controller A. However, in this case there exists the fact that, for certain initial conditions, Controller B will allow for very large errors.

It can be seen in Chapter 5 that a circumstance such as that outlined above exists in the case of the classical and LQR controllers. As a summary, results from the classical and LQR controllers given in Table 5-1, Table 5-2, Table 5-5, and Table 5-6 are condensed in the following table.

Table 6-1 Summary of velocity, gyro, and lambda errors

Control Scheme	Null Angle	Initial OG Angle (deg)	Steady-State Velocity Error (ft/sec)	Maximum RSS Gyro Error (bits)	Peak Lambda (no units)
Classical	θ_3	-17.786	0.0159	638.0	0.2865
Classical	θ_3	-4.856	0.0106	803.4	0.2329
Classical	θ_3	4.856	0.0106	803.4	0.2329
Classical	θ_3	17.785	0.0159	638.7	0.2866
Classical	θ_2	-85.072	0.0068	783.3	0.1981
Classical	θ_2	-72.104	0.0093	847.3	0.2630
Classical	θ_2	72.104	0.0093	848.1	0.2630
Classical	θ_2	85.074	0.0068	783.6	0.1981
LQR	θ_3	-5.001	0.0041	1389.1	0.0051
LQR	θ_3	5.001	0.0041	1389.2	0.0051
LQR	θ_2	-84.999	0.0075	1841.2	0.0074
LQR	θ_2	84.999	0.0075	1820.2	0.0074

Recall the following definition of lambda, which indicates proximity to gimbal lock, from (3.3.1).

$$\lambda = \sin(\theta_2) \cdot \sin(\theta_3)$$
(6.1.1)

In Table 6-1 above, several things can be observed. First, in the case of peak lambda errors, all the LQR errors are much smaller than the classical errors. In this instance, it is clear that the LQR controller outperforms the classical controller significantly. As one of the main goals of the platform controller is to minimize the lambda error, it is apparent that an LQR approach offers a great benefit in this area.

Second, in terms of velocity errors, Table 6-1 above reveals a situation similar to the one outlined in Figure 6.1.1. Generally, the LQR controller offers lower velocity errors; however, there are a few conditions for which the classical controller actually has smaller velocity errors. For these conditions, the velocity errors for the LQR controller, while larger, are actually very similar to those of the classical controller. Hence, it can be concluded that, due to the significant improvement in velocity errors over the majority of initial conditions and only slightly higher errors for a small number of conditions, the LQR controller outperforms the classical controller when considering velocity errors as well. As this is a second main goal of the platform controller, the LQR can be reasonably concluded to be superior.

Finally, it should be mentioned that, when considering gyro errors, it is obvious that the classical controller is superior. In fact, all the gyro errors in Table 6-1 are larger for the LQR controller. Although this may appear to contradict the statements above supporting the LQR controller as superior, larger gyro errors do not necessarily condemn the LQR approach. As velocity errors are the critical metric to consider for missile navigational purposes [1], the larger RSS gyro errors in the LQR controller can be tolerated as long as the velocity errors are improved.

From Table 6-1 above, it is interesting to observe that the maximum steady-state velocity errors in the case of the LQR controller are at the points of discontinuity, which are created by the switching theta dot gain. It is apparent that the switching theta dot gain plays a key role in determining the worst-case velocity error conditions in the LQR controller.

Table 6-2 Summary of peak torques

Control Scheme	Null Angle	Initial OG Angle (deg)	Peak OGTQ (bits)	Peak MGTQ (bits)	Peak OTC (bits)	Peak MTC (bits)
Classical	θ_3	-17.786	1485.3	712.5	3120.7	624.8
Classical	θ_3	-4.856	1211.5	1729.9	1722.3	2302.6
Classical	θ_3	4.856	1214.1	1729.7	1723.6	2301.9
Classical	θ_3	17.785	1486.0	707.2	3120.2	625.2
Classical	θ_2	-85.072	1074.7	1481.7	1850.7	2001.2
Classical	θ_2	-72.104	1358.5	1744.8	1984.7	2316.9
Classical	θ_2	72.104	1359.2	1744.6	1983.2	2317.1
Classical	θ_2	85.074	1074.9	1481.3	1851.5	2000.8
LQR	θ_3	-5.001	11029.0	1301.7	11029.0	455.0
LQR	θ_3	5.001	11029.0	1303.1	11029.0	454.6
LQR	θ_2	-84.999	11029.0	2464.8	11029.0	3700.9
LQR	θ_2	84.999	11029.0	2465.4	11029.0	3683.4

In Table 6-2 above, the peak torque commands of Table 5-3, Table 5-4, Table 5-7, and Table 5-8 are summarized. As the initial conditions leading to the largest velocity errors are presented in Table 6-2, it is surprising that the classical controller does not issue larger torque commands. It is likely that the reason the LQR controller does so much better in minimizing both velocity and lambda errors is due to the fact that the LQR controller makes better use of the available torque resources.

The results summarized above in Table 6-1 and Table 6-2 present a strong case that the LQR control design is superior to the classic design. Although the excellent performance characteristics of the LQR controller design have been well established [5], it is gratifying to see this superior performance realized in a complex, nonlinear system.

6.2 Future Work

Several areas pertaining to the pseudo-optimal control approach to platform control remain rich with possibilities for future work. The following suggestions are meant to outline the end of the current work and offer some areas for further investigation; they are by no means thoroughly inclusive.

First, a more extensive evaluation of the LQR controller presented in this thesis could be undertaken. This could include adding roll components to the input motion and attempting a more exhaustive numerical search for the worst-case velocity error conditions. To this end, it may be possible to design a controller, external to the platform controller, to control missile input case motion. This controller would monitor the lambda error and try to force input motions which would drive the gimbals towards gimbal lock. In this manner, a better understanding of the true global maximum velocity errors could be reached.

A second area for future work could involve slight modifications to the LQR controller. For example, a more complete model of the system, including the gyro error compensators, could be formed for loop shaping. In this manner, system performance requirements for the singular values might be defined and met by the loop shaping method. This could provide better choices for the LQR weightings.

In addition to loop shaping, the current LQR controller has been shown to be very sensitive to the theta dot gain. In fact, the discontinuities created by the switching theta dot gain account for the worst-case velocity errors in the LQR controller. A number of options might be considered to improve this.

It may be possible to improve controller performance by optimizing the switching theta dot gain. This could entail varying the gain and the point at which it is switched over a wide range of values and searching for the gains and switch points leading to the smallest velocity errors. Also, it may be possible to eliminate the theta dot gain altogether. This

would entail having time-varying LQR weighting matrices which would perform the same function as the switching theta dot gain.

Another way to improve the present controller could be in the calculation of the F gain matrix. It has been acknowledged that the LQR control scheme herein implemented is actually pseudo-optimal. This is due to the F matrices which are calculated a priori for a fixed number of nominal conditions and then stored in a look-up table for real-time execution. Instead, the true optimal approach would be to calculate the nominal conditions and then calculate the F matrix in real time. This area needs further investigation as it is unclear at this point whether the potential time delay due to the large number of calculations necessary for the F matrix would offset improvements by having a truly optimal LQR controller.

Finally, a third area for future work could comprise control schemes altogether different from LQR. Two are suggested below.

The four gimbal system treats the input case motion as a disturbance to the system. However, as a sound mathematical description of this disturbance has been given, it may be possible to implement a robust control technique. As the techniques of H-infinity and Mu-synthesis are becoming better understood and more frequently applied, these types of robust controllers may be investigated for use in the four gimbal system. Further, as these techniques generally demand a linear system, the linearized four gimbal system presented herein is ideal for further research in this area.

Alternatively, the loop shaping method could be explored in further detail. The methods of loop shaping described in this thesis are severely limited by the fact that only an LQR gain is present in the feedback loop. In the more traditional loop shaping, the feedback loop would contain a transfer function to shape the singular values in almost any manner desired. This method would allow for more freedom when meeting loop shaping performance requirements which could be defined as suggested above.

This page intentionally left blank.

Appendix A Equations of Motion

For a rigid gimbal of mass m_i and inertia matrix J^i, the angular momentum equation, in terms of velocity states, with all vector components expressed in a body-fixed, non-centroidal frame, expresses the inertial angular acceleration $\dot{\varpi}$ in terms of the net sum of all torques acting upon the gimbal as follows [10].

$$m_i[\bar{r}_i^c \times]T_0^i \dot{v} + J^i \dot{\varpi}_i = \sum \bar{\tau} - (\varpi_i \times J^i \varpi_i) \qquad (A.1)$$

Above and throughout, the over-bar notation indicates the vector is expressed in a rotating, body-fixed frame and a vector absent the over-bar is expressed in a non-rotating, inertial frame. Also, since linear acceleration is taken as a kinematic driving input to the gimbal system, only angular degrees-of-freedom will be considered.

In (A.1), $\dot{v}$ is conventionally understood to be the absolute translational acceleration of the reference point for inertia and torque or in other words, the origin of the respective gimbal frame, here specified in terms of an inertial frame time-derivative quantity and rotated into the applicable body-fixed frame. Similarly, the torque summation includes the moment of the gravitational force, mg, where $\bar{r}^c$ locates the center of gravity relative to the frame origin. In terms of non-gravitational specific force, S_f, (A.1) can be rewritten as follows.

$$m_i[\bar{r}_i^c \times]T_0^i (S_f + g) + J^i \dot{\varpi}_i = \{\sum \bar{\tau}^* + m_i[\bar{r}_i^c \times]T_0^i g\} - (\varpi_i \times J^i \varpi_i) \qquad (A.2)$$

Thus, the gravitational torque does not impart angular accelerations as it is precisely balanced by the acceleration effect of the reference point origin. But here and elsewhere the notation of (A.1) will be retained, with $\dot{v}$ optionally taken for specific force rather than absolute acceleration if the gravity contribution is similarly excluded from the torque

summation. In such a case, with $\bar{\tau}_i$ defined as the torque applied to gimbal i by gimbal i-I, then $\sum \bar{\tau} = \bar{\tau}_i - T^i_{i+1}\bar{\tau}_{i+1}$. Expanding (A.1) then yields the following equivalent expressions.

$$\begin{bmatrix} J^i_{xx} & J^i_{xy} & J^i_{xz} \\ & J^i_{yy} & J^i_{yz} \\ sym & & J^i_{zz} \end{bmatrix}\begin{bmatrix} \dot{\varpi}_{ix} \\ \dot{\varpi}_{iy} \\ \dot{\varpi}_{iz} \end{bmatrix} + \begin{bmatrix} 0 & c\theta_{i+1} & s\theta_{i+1} \\ 0 & -s\theta_{i+1} & c\theta_{i+1} \\ 1 & 0 & 0 \end{bmatrix}\begin{bmatrix} \tau^{mot}_{i+1} \\ \tau_{(i+1)y} \\ \tau_{(i+1)z} \end{bmatrix} = \begin{bmatrix} \tau^{mot}_i \\ \tau_{iy} \\ \tau_{iz} \end{bmatrix} + \begin{bmatrix} -\{(\varpi_i \times J^i \varpi_i)+(m\bar{r}^c_i \times T^i_0 \dot{v})\}_x \\ -\{(\varpi_i \times J^i \varpi_i)+(m\bar{r}^c_i \times T^i_0 \dot{v})\}_y \\ -\{(\varpi_i \times J^i \varpi_i)+(m\bar{r}^c_i \times T^i_0 \dot{v})\}_z \end{bmatrix} \quad (A.3)$$

$$\begin{bmatrix} J^i_{xx} & J^i_{xy} & J^i_{xz} \\ & J^i_{yy} & J^i_{yz} \\ sym & & J^i_{zz} \end{bmatrix}\begin{bmatrix} \dot{\varpi}_{ix} \\ \dot{\varpi}_{iy} \\ \dot{\varpi}_{iz} \end{bmatrix} + \begin{bmatrix} 0 & 0 & -c\theta_{i+1} & -s\theta_{i+1} \\ 1 & 0 & s\theta_{i+1} & -c\theta_{i+1} \\ 0 & 1 & 0 & 0 \end{bmatrix}\begin{bmatrix} -\tau_{iy} \\ -\tau_{iz} \\ -\tau_{(i+1)y} \\ -\tau_{(i+1)z} \end{bmatrix} = \begin{bmatrix} \tau^{mot}_i \\ 0 \\ -\tau^{mot}_{i+1} \end{bmatrix} + \begin{bmatrix} -\{(\varpi_i \times J^i \varpi_i)+(m\bar{r}^c_i \times T^i_0 \dot{v})\}_x \\ -\{(\varpi_i \times J^i \varpi_i)+(m\bar{r}^c_i \times T^i_0 \dot{v})\}_y \\ -\{(\varpi_i \times J^i \varpi_i)+(m\bar{r}^c_i \times T^i_0 \dot{v})\}_z \end{bmatrix} \quad (A.4)$$

Equation (A.4), when repeated for each gimbal, and assembled into a generalized system, can be put into the conventional multibody "descriptor" form as follows [11].

$$M\dot{\varpi} + C^T_{\varpi}\lambda = Q_e + Q_v \quad (A.5)$$

Here the constraint torques may be treated as Lagrange multipliers, with the right-hand-side terms designated as Q_e and Q_v to indicate external and velocity-dependent terms. C_{ϖ} is the Constraint Jacobian matrix determined from the kinematic expansion. For appropriate choices of independent and dependent coordinates, it may be partitioned according to $C^T_{\varpi} \equiv [C_{\varpi i} \quad C_{\varpi d}]^T$ [11].

The explicit solution to the generalized system, then, is directly expressible.

$$\dot{\varpi}_{ind} \equiv [\dot{\varpi}_{1x} \quad \dot{\varpi}_{2x} \quad \dot{\varpi}_{3x} \quad \dot{\varpi}_{4x}]^T = M_{sys}^{-1}[B^T P^T (Q_e + Q_v) - B^T(P^T MP)\overline{Q}_c] \quad (A.6)$$

The system inertia matrix is provided by $M_{sys} = B^T(P^T MP)B$ where the several gimbal inertia matrices are collected.

$$M = \begin{bmatrix} [J^1] & 0 & 0 & 0 \\ 0 & [J^2] & 0 & 0 \\ 0 & 0 & [J^3] & 0 \\ 0 & 0 & 0 & [J^4] \end{bmatrix} \tag{A.7}$$

$$Q_e = \begin{bmatrix} \left[\tau_1^{mot} \quad 0 \quad -\tau_2^{mot}\right]^T \\ \left[\tau_2^{mot} \quad 0 \quad -\tau_3^{mot}\right]^T \\ \left[\tau_3^{mot} \quad 0 \quad -\tau_4^{mot}\right]^T \\ \left[\tau_4^{mot} \quad 0 \quad 0\right]^T \end{bmatrix} \tag{A.8}$$

$$Q_v = \begin{bmatrix} -\left[(\varpi_1 \times J^1 \varpi_1) + (m_1 \bar{r}_1^c \times T_0^1 \dot{v})\right] \\ -\left[(\varpi_2 \times J^2 \varpi_2) + (m_2 \bar{r}_2^c \times T_0^2 \dot{v})\right] \\ -\left[(\varpi_3 \times J^3 \varpi_3) + (m_3 \bar{r}_3^c \times T_0^3 \dot{v})\right] \\ -\left[(\varpi_4 \times J^4 \varpi_4) + (m_4 \bar{r}_4^c \times T_0^4 \dot{v})\right] \end{bmatrix} \tag{A.9}$$

Note that the equal and opposite reactions of the external mechanical torque inputs appear in equation (A.8) in accordance with consecutive frame orientations shown in Figure 2.3.1. In (A.6), conceptually, P is a 12x12 independent/dependent coordinate partitioning matrix of ones and zeros such that the independent and dependent components are defined as follows.

$$\dot{\varpi}_{ind} \equiv [\dot{\varpi}_{1x} \ ... \ \dot{\varpi}_{4x}]^T \tag{A.10}$$

$$\dot{\varpi}_{dep} \equiv [\dot{\varpi}_{1y} \ \dot{\varpi}_{1z} \ ... \ \dot{\varpi}_{4y} \ \dot{\varpi}_{4z}]^T \tag{A.11}$$

Then, the P matrix will partition as below.

$$[\dot{\varpi}_{1x} \ \dot{\varpi}_{1y} \ \dot{\varpi}_{1z} \ ... \ \dot{\varpi}_{4x} \ \dot{\varpi}_{4y} \ \dot{\varpi}_{4z}]^T = P \begin{bmatrix} \dot{\varpi}_{ind} \\ \dot{\varpi}_{dep} \end{bmatrix} \tag{A.12}$$

The kinematic constraint equations provide the relation between the 4 independent x axis gimbal inertial angular accelerations and the 8 kinematically dependent gimbal inertial angular accelerations, or the y and z axis components for each of the 4 gimbals, through use of the reference frame transformation T_i^{i+1} from (2.3.1).

$$
\begin{bmatrix} \varpi_{(i+1)y} \\ \varpi_{(i+1)z} \end{bmatrix} = \begin{bmatrix} c\theta_{i+1} & -s\theta_{i+1} \\ s\theta_{i+1} & c\theta_{i+1} \end{bmatrix} \cdot \begin{bmatrix} \varpi_{ix} \\ \varpi_{iy} \end{bmatrix}
\tag{A.13}
$$

Thus, by differentiating (A.13) above for each of the gimbals, the following is obtained.

$$
C_{\varpi i} \dot{\varpi}_{ind} + C_{\varpi d} \dot{\varpi}_{dep} = Q_c \equiv
\begin{bmatrix}
\{ T_c^1 \dot{\varpi}_c + \dot{\theta}_1 (\frac{\partial}{\partial \theta_1} T_c^1) \varpi_c \}_y \\
\{ T_c^1 \dot{\varpi}_c + \dot{\theta}_1 (\frac{\partial}{\partial \theta_1} T_c^1) \varpi_c \}_z \\
\hline
\{ \dot{\theta}_2 (\frac{\partial}{\partial \theta_2} T_1^2) \varpi_1 \}_y \\
\{ \dot{\theta}_2 (\frac{\partial}{\partial \theta_2} T_1^2) \varpi_1 \}_z \\
\hline
\{ \dot{\theta}_3 (\frac{\partial}{\partial \theta_3} T_2^3) \varpi_2 \}_y \\
\{ \dot{\theta}_3 (\frac{\partial}{\partial \theta_3} T_2^3) \varpi_2 \}_z \\
\hline
\{ \dot{\theta}_4 (\frac{\partial}{\partial \theta_4} T_3^4) \varpi_3 \}_y \\
\{ \dot{\theta}_4 (\frac{\partial}{\partial \theta_4} T_3^4) \varpi_3 \}_z
\end{bmatrix}
\tag{A.14}
$$

In (A.14), the following definitions apply.

$$C_{\varpi i} = \begin{bmatrix} 0 & 0 & 0 & 0 \\ 0 & 0 & 0 & 0 \\ -c\theta_2 & 0 & 0 & 0 \\ -s\theta_2 & 0 & 0 & 0 \\ 0 & -c\theta_3 & 0 & 0 \\ 0 & -s\theta_3 & 0 & 0 \\ 0 & 0 & -c\theta_4 & 0 \\ 0 & 0 & -s\theta_4 & 0 \end{bmatrix} \tag{A.15}$$

$$C_{\varpi d} = \begin{bmatrix} 1 & 0 & 0 & 0 & 0 & 0 & 0 & 0 \\ 0 & 1 & 0 & 0 & 0 & 0 & 0 & 0 \\ s\theta_2 & 0 & 1 & 0 & 0 & 0 & 0 & 0 \\ -c\theta_2 & 0 & 0 & 1 & 0 & 0 & 0 & 0 \\ 0 & 0 & s\theta_3 & 0 & 1 & 0 & 0 & 0 \\ 0 & 0 & -c\theta_3 & 0 & 0 & 1 & 0 & 0 \\ 0 & 0 & 0 & 0 & s\theta_4 & 0 & 1 & 0 \\ 0 & 0 & 0 & 0 & -c\theta_4 & 0 & 0 & 1 \end{bmatrix} \tag{A.16}$$

Equation (A.14) can also be rearranged into the following.

$$\begin{bmatrix} \dot{\varpi}_{ind}^T & \dot{\varpi}_{dep}^T \end{bmatrix}^T = \begin{bmatrix} I_4 \\ -C_{\varpi d}^{-1} C_{\varpi i} \end{bmatrix} \dot{\varpi}_{ind} + \begin{bmatrix} 0_4 \\ C_{\varpi d}^{-1} Q_c \end{bmatrix} \tag{A.17}$$

$$\begin{bmatrix} \dot{\varpi}_{ind}^T & \dot{\varpi}_{dep}^T \end{bmatrix}^T = B\dot{\varpi}_{ind} + \overline{Q}_c \tag{A.18}$$

The gimbal angle convention is thus.

$$\dot{\theta}_i = \varpi_{(i-1)z} - \varpi_{ix} \tag{A.19}$$

In (A.17) and (A.18), the following definitions apply.

143

$$B = \begin{bmatrix} \multicolumn{4}{c}{I_4} \\ 0 & 0 & 0 & 0 \\ 0 & 0 & 0 & 0 \\ c\theta_2 & 0 & 0 & 0 \\ s\theta_2 & 0 & 0 & 0 \\ -s\theta_3 c\theta_2 & c\theta_3 & 0 & 0 \\ c\theta_3 c\theta_2 & s\theta_3 & 0 & 0 \\ s\theta_4 s\theta_3 c\theta_2 & -s\theta_4 c\theta_3 & c\theta_4 & 0 \\ -c\theta_4 s\theta_3 c\theta_2 & c\theta_4 c\theta_3 & s\theta_4 & 0 \end{bmatrix}$$

(A.20)

$$C_{ad}^{-1} = \begin{bmatrix} 1 & & & & & & & & \\ 0 & 1 & & & & \ddots & & & \\ -s\theta_2 & 0 & 1 & & & & 0 & & \\ c\theta_2 & 0 & 0 & 1 & & & & \ddots & \\ s\theta_3 s\theta_2 & 0 & -s\theta_3 & 0 & 1 & & & & \\ -c\theta_3 s\theta_2 & 0 & c\theta_3 & 0 & 0 & 1 & & & \\ -s\theta_4 s\theta_3 s\theta_2 & 0 & s\theta_4 s\theta_3 & 0 & -s\theta_4 & 0 & 1 & & \\ c\theta_4 s\theta_3 s\theta_2 & 0 & -c\theta_4 s\theta_3 & 0 & c\theta_4 & 0 & 0 & 1 \end{bmatrix}$$

(A.21)

$$\overline{Q}_c = \begin{bmatrix} 0_{4x1} \\ \begin{bmatrix} c\theta_1 & -s\theta_1 \\ s\theta_1 & c\theta_1 \end{bmatrix}\begin{bmatrix} \dot{\varpi}_{cx} \\ \dot{\varpi}_{cy} \end{bmatrix} + \dot{\theta}_1\begin{bmatrix} -s\theta_1 & -c\theta_1 \\ c\theta_1 & -s\theta_1 \end{bmatrix}\begin{bmatrix} \varpi_{cx} \\ \varpi_{cy} \end{bmatrix} \\ \begin{bmatrix} -s\theta_2 \\ c\theta_2 \end{bmatrix}\overline{Q}_c(5,1) + \dot{\theta}_2\begin{bmatrix} -s\theta_2 & -c\theta_2 \\ c\theta_2 & -s\theta_2 \end{bmatrix}\begin{bmatrix} \varpi_{1x} \\ \varpi_{1y} \end{bmatrix} \\ \begin{bmatrix} -s\theta_3 \\ c\theta_3 \end{bmatrix}\overline{Q}_c(7,1) + \dot{\theta}_3\begin{bmatrix} -s\theta_3 & -c\theta_3 \\ c\theta_3 & -s\theta_3 \end{bmatrix}\begin{bmatrix} \varpi_{2x} \\ \varpi_{2y} \end{bmatrix} \\ \begin{bmatrix} -s\theta_4 \\ c\theta_4 \end{bmatrix}\overline{Q}_c(9,1) + \dot{\theta}_4\begin{bmatrix} -s\theta_4 & -c\theta_4 \\ c\theta_4 & -s\theta_4 \end{bmatrix}\begin{bmatrix} \varpi_{3x} \\ \varpi_{3y} \end{bmatrix} \end{bmatrix}$$

(A.22)

Here, the lower 8 by 4 portion of the projection matrix B in equation (A.20) provides the mapping between the 4 rotational axes and the y and z axis components of each of the gimbals.

Finally, from (A.13) and the gimbal angle convention (A.19), a description of the gimbal angles is obtained.

$$
\begin{bmatrix} \dot{\theta}_1 \\ \dot{\theta}_2 \\ \dot{\theta}_3 \\ \dot{\theta}_4 \end{bmatrix} \equiv \begin{bmatrix} \varpi_{cz} \\ \varpi_{1z} \\ \varpi_{2z} \\ \varpi_{3z} \end{bmatrix} - \begin{bmatrix} \varpi_{1x} \\ \varpi_{2x} \\ \varpi_{3x} \\ \varpi_{4x} \end{bmatrix} = \begin{bmatrix} -1 & 0 & 0 & 0 \\ 0 & -1 & 0 & 0 \\ s\theta_2 & 0 & -1 & 0 \\ c\theta_3 c\theta_2 & s\theta_3 & 0 & -1 \end{bmatrix} \cdot \begin{bmatrix} \varpi_{1x} \\ \varpi_{2x} \\ \varpi_{3x} \\ \varpi_{4x} \end{bmatrix} + \begin{bmatrix} [0 & 0 & 1]\varpi_c \\ [s\theta_1 & c\theta_1 & 0]\varpi_c \\ c\theta_2[c\theta_1 & -s\theta_1 & 0]\varpi_c \\ -c\theta_3 s\theta_2[c\theta_1 & -s\theta_1 & 0]\varpi_c \end{bmatrix}
\qquad (A.23)
$$

For more information on the derivation of these equations see [10] and [11].

145

This page intentionally left blank.

Appendix B Partial Derivative Terms in the A, B, and G Matrices

The following are the terms in A, B, and G matrices of (2.4.12), (2.4.13), and (2.4.14). These terms are obtained by taking partial derivatives as expressed in (2.4.3), (2.4.4), and (2.4.5). None of the equations in Appendix B will be numbered as they are only presented here for information and will not be referenced elsewhere.

First, a few terms are defined to enable more concise notation.

$$c\theta_i = \cos(\theta_i)$$

$$s\theta_i = \sin(\theta_i)$$

$$c\theta_i^2 = \cos^2(\theta_i)$$

$$s\theta_i^2 = \sin^2(\theta_i)$$

Equations (2.3.7) to (2.3.10) representing inertia approximations, as well as (2.3.12), will be used throughout. These equations are repeated below.

$$J_{ox} \approx J_{xx}^1 + J_s^2 + c\theta_2^2 J_s^3 + c\theta_2^2 s\theta_3^2 J_s^4$$

$$J_{mx} \approx J_{xx}^2 + J_s^3 + c\theta_3^2 J_s^4$$

$$J_{ix} \approx J_{xx}^3 + J_s^4$$

$$J_s^{2,3,4} \approx \left(J_{xx}^{2,3,4} + J_{yy}^{2,3,4} + J_{zz}^{2,3,4} \right)\!\big/3$$

$$\Delta = [J_{xx}^1 + J_s^2 + c\theta_2^2 C + c\theta_2^2 s\theta_3^2 J_s^4] \cdot [J_{xx}^2 + J_s^3 + c\theta_3^2 J_s^4] - [c\theta_2^2 c\theta_3^2 s\theta_3^2 J_s^4 J_s^4]$$

Now, some preliminary terms are defined.

$$\tau_1^{ff} = [c\theta_1\dot{\varpi}_{cx} - s\theta_1\dot{\varpi}_{cy} - s\theta_1\varpi_{cx}\varpi_{cz} - c\theta_1\varpi_{cy}\varpi_{cz}] \cdot [-c\theta_2 s\theta_2] \cdot [s\theta_3^2 J_{yy}^3 + c\theta_3^2 J_{zz}^3 + s\theta_3^2 J_s^4] -$$
$$[c\theta_1 s\theta_1\varpi_{cx}^2 - s\theta_1^2\varpi_{cx}\varpi_{cy} + c\theta_1^2\varpi_{cx}\varpi_{cy} - c\theta_1 s\theta_1\varpi_{cy}^2] \cdot [J_s^2 + c\theta_2^2 s\theta_3^2 J_{yy}^3 + c\theta_2^2 c\theta_3^2 J_{zz}^3 + c\theta_2^2 s\theta_3^2 J_s^4] +$$
$$[c\theta_1\varpi_{cx} - s\theta_1\varpi_{cy}]^2 \cdot [c\theta_2^2 s\theta_2 c\theta_3 s\theta_3] \cdot [J_{zz}^3 - J_{yy}^3 - J_s^4]$$

$$\tau_2^{ff} = [c\theta_1\dot{\varpi}_{cx} - s\theta_1\dot{\varpi}_{cy} - s\theta_1\varpi_{cx}\varpi_{cz} - c\theta_1\varpi_{cy}\varpi_{cz}] \cdot [-s\theta_2 c\theta_3 s\theta_3] \cdot [J_{zz}^3 - J_{yy}^3 - J_s^4] -$$
$$[c\theta_1 s\theta_1\varpi_{cx}^2 - s\theta_1^2\varpi_{cx}\varpi_{cy} + c\theta_1^2\varpi_{cx}\varpi_{cy} - c\theta_1 s\theta_1\varpi_{cy}^2] \cdot [c\theta_2 c\theta_3 s\theta_3] \cdot [J_{zz}^3 - J_{yy}^3 - J_s^4] +$$
$$[c\theta_1\varpi_{cx} - s\theta_1\varpi_{cy}]^2 \cdot [c\theta_2 s\theta_2] \cdot [s\theta_3^2 J_{zz}^3 + c\theta_3^2 J_{yy}^3 + c\theta_3^2 J_s^4]$$

$$\tau_3^{ff} = [c\theta_1\varpi_{cx} - s\theta_1\varpi_{cy}]^2 \cdot [s\theta_2^2 c\theta_3 s\theta_3 J_s^4]$$

Next, some intermediate partial derivatives will be defined. These partial derivatives will eventually appear in the definitions of the A, B, and G terms.

$$\frac{\partial J_{ox}}{\partial\theta_2} = -2c\theta_2 s\theta_2 J_s^3 - 2c\theta_2 s\theta_2 s\theta_3^2 J_s^4$$

$$\frac{\partial J_{ox}}{\partial\theta_3} = 2c\theta_2^2 c\theta_3 s\theta_3 J_s^4$$

$$\frac{\partial J_{mx}}{\partial\theta_3} = -2c\theta_3 s\theta_3 J_s^4$$

$$\frac{\partial\Delta}{\partial\theta_2} = [-2c\theta_2 s\theta_2 J_s^3 - 2c\theta_2 s\theta_2 s\theta_3^2 J_s^4] \cdot [J_{xx}^2 + J_s^3 + c\theta_3^2 J_s^4] + [2c\theta_2 s\theta_2 c\theta_3^2 s\theta_3^2 J_s^4 J_s^4]$$

$$\frac{\partial \Delta}{\partial \theta_3} = [2c\theta_2^2 c\theta_3 s\theta_3 J_s^4] \cdot [J_{xx}^2 + J_s^3 + c\theta_3^2 J_s^4] + [J_{xx}^1 + J_s^2 + c\theta_2^2 J_s^3 + c\theta_2^2 s\theta_3^2 J_s^4] \cdot [-2c\theta_3 s\theta_3 J_s^4] -$$

$$[-2c\theta_2^2 c\theta_3 s\theta_3^3 J_s^4 J_s^4 + 2c\theta_2^2 c\theta_3^3 s\theta_3 J_s^4 J_s^4]$$

$$\frac{\partial \tau_1^{ff}}{\partial \theta_1} = [-s\theta_1 \dot{\varpi}_{cx} - c\theta_1 \dot{\varpi}_{cy} - c\theta_1 \varpi_{cx} \varpi_{cz} + s\theta_1 \varpi_{cy} \varpi_{cz}] \cdot [-c\theta_2 s\theta_2] \cdot [s\theta_3^2 J_{yy}^3 + c\theta_3^2 J_{zz}^3 + s\theta_3^2 J_s^4] -$$

$$[c\theta_1^2 \varpi_{cx}^2 - s\theta_1^2 \varpi_{cx}^2 - 4c\theta_1 s\theta_1 \varpi_{cx} \varpi_{cy} - c\theta_1^2 \varpi_{cy}^2 + s\theta_1^2 \varpi_{cy}^2] \cdot [J_s^2 + c\theta_2^2 s\theta_3^2 J_{yy}^3 + c\theta_2^2 c\theta_3^2 J_{zz}^3 + c\theta_2^2 s\theta_3^2 J_s^4] +$$

$$[2c\theta_2^2 s\theta_2 c\theta_3 s\theta_3] \cdot [c\theta_1 \varpi_{cx} - s\theta_1 \varpi_{cy}] \cdot [-s\theta_1 \varpi_{cx} - c\theta_1 \varpi_{cy}] \cdot [J_{zz}^3 - J_{yy}^3 - J_s^4]$$

$$\frac{\partial \tau_1^{ff}}{\partial \theta_2} = [c\theta_1 \dot{\varpi}_{cx} - s\theta_1 \dot{\varpi}_{cy} - s\theta_1 \varpi_{cx} \varpi_{cz} - c\theta_1 \varpi_{cy} \varpi_{cz}] \cdot [s\theta_2^2 - c\theta_2^2] \cdot [s\theta_3^2 J_{yy}^3 + c\theta_3^2 J_{zz}^3 + s\theta_3^2 J_s^4] -$$

$$[c\theta_1 s\theta_1 \varpi_{cx}^2 - s\theta_1^2 \varpi_{cx} \varpi_{cy} + c\theta_1^2 \varpi_{cx} \varpi_{cy} - c\theta_1 s\theta_1 \varpi_{cy}^2] \cdot [-2c\theta_2 s\theta_2 s\theta_3^2 J_{yy}^3 - 2c\theta_2 s\theta_2 c\theta_3^2 J_{zz}^3 - 2c\theta_2 s\theta_2 s\theta_3^2 J_s^4] +$$

$$[c\theta_3 s\theta_3] \cdot [c\theta_1 \varpi_{cx} - s\theta_1 \varpi_{cy}]^2 \cdot [-2c\theta_2 s\theta_2^2 + c\theta_2^3] \cdot [J_{zz}^3 - J_{yy}^3 - J_s^4]$$

$$\frac{\partial \tau_1^{ff}}{\partial \theta_3} = [c\theta_1 \dot{\varpi}_{cx} - s\theta_1 \dot{\varpi}_{cy} - s\theta_1 \varpi_{cx} \varpi_{cz} - c\theta_1 \varpi_{cy} \varpi_{cz}] \cdot [-c\theta_2 s\theta_2] \cdot [2c\theta_3 s\theta_3 J_{yy}^3 - 2c\theta_3 s\theta_3 J_{zz}^3 + 2c\theta_3 s\theta_3 J_s^4] -$$

$$[c\theta_1 s\theta_1 \varpi_{cx}^2 - s\theta_1^2 \varpi_{cx} \varpi_{cy} + c\theta_1^2 \varpi_{cx} \varpi_{cy} - c\theta_1 s\theta_1 \varpi_{cy}^2] \cdot [2c\theta_2^2 c\theta_3 s\theta_3 J_{yy}^3 - 2c\theta_2^2 c\theta_3 s\theta_3 J_{zz}^3 + 2c\theta_2^2 c\theta_3 s\theta_3 J_s^4] +$$

$$[c\theta_2^2 s\theta_2] \cdot [c\theta_1 \varpi_{cx} - s\theta_1 \varpi_{cy}]^2 \cdot [c\theta_3^2 - s\theta_3^2] \cdot [J_{zz}^3 - J_{yy}^3 - J_s^4]$$

$$\frac{\partial \tau_1^{ff}}{\partial \varpi_{cx}} = [s\theta_1 c\theta_2 s\theta_2 \varpi_{cz}] \cdot [s\theta_3^2 J_{yy}^3 + c\theta_3^2 J_{zz}^3 + s\theta_3^2 J_s^4] -$$

$$[2c\theta_1 s\theta_1 \varpi_{cx} - s\theta_1^2 \varpi_{cy} + c\theta_1^2 \varpi_{cy}] \cdot [J_s^2 + c\theta_2^2 s\theta_3^2 J_{yy}^3 + c\theta_2^2 c\theta_3^2 J_{zz}^3 + c\theta_2^2 s\theta_3^2 J_s^4] +$$

$$[2c\theta_1 c\theta_2^2 s\theta_2 c\theta_3 s\theta_3] \cdot [c\theta_1 \varpi_{cx} - s\theta_1 \varpi_{cy}] \cdot [J_{zz}^3 - J_{yy}^3 - J_s^4]$$

$$\frac{\partial \tau_1^{ff}}{\partial \varpi_{cy}} = [c\theta_1 c\theta_2 s\theta_2 \varpi_{cz}] \cdot [s\theta_3^2 J_{yy}^3 + c\theta_3^2 J_{zz}^3 + s\theta_3^2 J_s^4] -$$

$$[-s\theta_1^2 \varpi_{cy} + c\theta_1^2 \varpi_{cy} - 2c\theta_1 s\theta_1 \varpi_{cy}] \cdot [J_s^2 + c\theta_2^2 s\theta_3^2 J_{yy}^3 + c\theta_2^2 c\theta_3^2 J_{zz}^3 + c\theta_2^2 s\theta_3^2 J_s^4] +$$

$$[-2s\theta_1 c\theta_2^2 s\theta_2 c\theta_3 s\theta_3] \cdot [c\theta_1 \varpi_{cx} - s\theta_1 \varpi_{cy}] \cdot [J_{zz}^3 - J_{yy}^3 - J_s^4]$$

$$\frac{\partial \tau_1^{ff}}{\partial \varpi_{cz}} = [s\theta_1 \varpi_{cx} + c\theta_1 \varpi_{cy}] \cdot [c\theta_2 s\theta_2] \cdot [s\theta_3^2 J_{yy}^3 + c\theta_3^2 J_{zz}^3 + s\theta_3^2 J_s^4]$$

$$\frac{\partial \tau_1^{ff}}{\partial \dot{\varpi}_{cx}} = [-c\theta_1 c\theta_2 s\theta_2] \cdot [s\theta_3^2 J_{yy}^3 + c\theta_3^2 J_{zz}^3 + s\theta_3^2 J_s^4]$$

$$\frac{\partial \tau_1^{ff}}{\partial \dot{\varpi}_{cy}} = [s\theta_1 c\theta_2 s\theta_2] \cdot [s\theta_3^2 J_{yy}^3 + c\theta_3^2 J_{zz}^3 + s\theta_3^2 J_s^4]$$

$$\frac{\partial \tau_2^{ff}}{\partial \theta_1} = [-s\theta_1 \dot{\varpi}_{cx} - c\theta_1 \dot{\varpi}_{cy} - c\theta_1 \varpi_{cx} \varpi_{cz} + s\theta_1 \varpi_{cy} \varpi_{cz}] \cdot [-s\theta_2 c\theta_3 s\theta_3] \cdot [J_{zz}^3 - J_{yy}^3 - J_s^4] -$$
$$[c\theta_1^2 \varpi_{cx}^2 - s\theta_1^2 \varpi_{cx}^2 - 4c\theta_1 s\theta_1 \varpi_{cx} \varpi_{cy} + s\theta_1^2 \varpi_{cy}^2 - c\theta_1^2 \varpi_{cy}^2] \cdot [c\theta_2 c\theta_3 s\theta_3] \cdot [J_{zz}^3 - J_{yy}^3 - J_s^4] +$$
$$[c\theta_1 \varpi_{cx} - s\theta_1 \varpi_{cy}] \cdot [-s\theta_1 \varpi_{cx} - c\theta_1 \varpi_{cy}] \cdot [2c\theta_2 s\theta_2] \cdot [s\theta_3^2 J_{zz}^3 + c\theta_3^2 J_{yy}^3 + c\theta_3^2 J_s^4]$$

$$\frac{\partial \tau_2^{ff}}{\partial \theta_2} = [c\theta_1 \dot{\varpi}_{cx} - s\theta_1 \dot{\varpi}_{cy} - s\theta_1 \varpi_{cx} \varpi_{cz} - c\theta_1 \varpi_{cy} \varpi_{cz}] \cdot [-c\theta_2 c\theta_3 s\theta_3] \cdot [J_{zz}^3 - J_{yy}^3 - J_s^4] -$$
$$[c\theta_1 s\theta_1 \varpi_{cx}^2 - s\theta_1^2 \varpi_{cx} \varpi_{cy} + c\theta_1^2 \varpi_{cx} \varpi_{cy} - c\theta_1 s\theta_1 \varpi_{cy}^2] \cdot [-s\theta_2 c\theta_3 s\theta_3] \cdot [J_{zz}^3 - J_{yy}^3 - J_s^4] +$$
$$[c\theta_1 \varpi_{cx} - s\theta_1 \varpi_{cy}]^2 \cdot [c\theta_2^2 - s\theta_2^2] \cdot [s\theta_3^2 J_{zz}^3 + c\theta_3^2 J_{yy}^3 + c\theta_3^2 J_s^4]$$

$$\frac{\partial \tau_2^{ff}}{\partial \theta_3} = [c\theta_1 \dot{\varpi}_{cx} - s\theta_1 \dot{\varpi}_{cy} - s\theta_1 \varpi_{cx} \varpi_{cz} - c\theta_1 \varpi_{cy} \varpi_{cz}] \cdot [-s\theta_2] \cdot [c\theta_3^2 - s\theta_3^2] \cdot [J_{zz}^3 - J_{yy}^3 - J_s^4] -$$
$$[c\theta_1 s\theta_1 \varpi_{cx}^2 - s\theta_1^2 \varpi_{cx} \varpi_{cy} + c\theta_1^2 \varpi_{cx} \varpi_{cy} - c\theta_1 s\theta_1 \varpi_{cy}^2] \cdot [c\theta_2] \cdot [c\theta_3^2 - s\theta_3^2] \cdot [J_{zz}^3 - J_{yy}^3 - J_s^4] +$$
$$[c\theta_1 \varpi_{cx} - s\theta_1 \varpi_{cy}]^2 \cdot [c\theta_2 s\theta_2] \cdot [2c\theta_3 s\theta_3 J_{zz}^3 - 2c\theta_3 s\theta_3 J_{yy}^3 - 2c\theta_3 s\theta_3 J_s^4]$$

$$\frac{\partial \tau_2^{ff}}{\partial \varpi_{cx}} = [s\theta_1 s\theta_2 c\theta_3 s\theta_3 \varpi_{cz}] \cdot [J_{zz}^3 - J_{yy}^3 - J_s^4] -$$
$$[2c\theta_1 s\theta_1 \varpi_{cy} - s\theta_1^2 \varpi_{cy} + c\theta_1^2 \varpi_{cy}] \cdot [c\theta_2 c\theta_3 s\theta_3] \cdot [J_{zz}^3 - J_{yy}^3 - J_s^4] +$$
$$[c\theta_1 \varpi_{cx} - s\theta_1 \varpi_{cy}] \cdot [2c\theta_1 c\theta_2 s\theta_2] \cdot [s\theta_3^2 J_{zz}^3 + c\theta_3^2 J_{yy}^3 + c\theta_3^2 J_s^4]$$

$$\frac{\partial \tau_2^{ff}}{\partial \varpi_{cy}} = [c\theta_1 s\theta_2 c\theta_3 s\theta_3 \varpi_{cz}] \cdot [J_{zz}^3 - J_{yy}^3 - J_s^4] -$$
$$[-s\theta_1^2 \varpi_{cx} + c\theta_1^2 \varpi_{cx} - 2c\theta_1 s\theta_1 \varpi_{cy}] \cdot [c\theta_2 c\theta_3 s\theta_3] \cdot [J_{zz}^3 - J_{yy}^3 - J_s^4] +$$
$$[c\theta_1 \varpi_{cx} - s\theta_1 \varpi_{cy}] \cdot [-2s\theta_1 c\theta_2 s\theta_2] \cdot [s\theta_3^2 J_{zz}^3 + c\theta_3^2 J_{yy}^3 + c\theta_3^2 J_s^4]$$

$$\frac{\partial \tau_2^{ff}}{\partial \varpi_{cz}} = [s\theta_1 \varpi_{cx} + c\theta_1 \varpi_{cy}] \cdot [s\theta_2 c\theta_3 s\theta_3] \cdot [J_{zz}^3 - J_{yy}^3 - J_s^4]$$

$$\frac{\partial \tau_2^{ff}}{\partial \dot{\varpi}_{cx}} = [-c\theta_1 s\theta_2 c\theta_3 s\theta_3] \cdot [J_{zz}^3 - J_{yy}^3 - J_s^4]$$

$$\frac{\partial \tau_2^{ff}}{\partial \dot{\varpi}_{cy}} = [s\theta_1 s\theta_2 c\theta_3 s\theta_3] \cdot [J_{zz}^3 - J_{yy}^3 - J_s^4]$$

$$\frac{\partial \tau_3^{ff}}{\partial \theta_1} = [c\theta_1 \varpi_{cx} - s\theta_1 \varpi_{cy}] \cdot [-s\theta_1 \varpi_{cx} - c\theta_1 \varpi_{cy}] \cdot [2s\theta_2^2 c\theta_3 s\theta_3 J_s^4]$$

$$\frac{\partial \tau_3^{ff}}{\partial \theta_2} = [c\theta_1 \varpi_{cx} - s\theta_1 \varpi_{cy}]^2 \cdot [2c\theta_2 s\theta_2 c\theta_3 s\theta_3 J_s^4]$$

$$\frac{\partial \tau_3^{ff}}{\partial \theta_3} = [c\theta_1 \varpi_{cx} - s\theta_1 \varpi_{cy}]^2 \cdot [c\theta_3^2 - s\theta_3^2] \cdot [s\theta_2^2 J_s^4]$$

$$\frac{\partial \tau_3^{ff}}{\partial \varpi_{cx}} = [c\theta_1 \varpi_{cx} - s\theta_1 \varpi_{cy}] \cdot [2c\theta_1 s\theta_2^2 c\theta_3 s\theta_3 J_s^4]$$

$$\frac{\partial \tau_3^{ff}}{\partial \varpi_{cy}} = [c\theta_1 \varpi_{cx} - s\theta_1 \varpi_{cy}] \cdot [-2s\theta_1 s\theta_2^2 c\theta_3 s\theta_3 J_s^4]$$

Finally, with these terms defined, the A, B, and G matrix terms can now be computed.

$$A_{1,5} = -\frac{J_{mx}}{\Delta} \left(\frac{\partial \tau_1^{ff}}{\partial \theta_1} \right) - \frac{c\theta_2 c\theta_3 s\theta_3 J_s^4}{\Delta} \left(\frac{\partial \tau_2^{ff}}{\partial \theta_1} \right)$$

$$A_{1,6} = \left\{ J_{mx}\left[-c\theta_2\tau_3 + s\theta_2 c\theta_3\tau_4 - \left(\frac{\partial \tau_1^{ff}}{\partial \theta_2} \right) \right] \cdot \Delta - J_{mx}\left[\tau_1 - s\theta_2\tau_3 - c\theta_2 c\theta_3\tau_4 - \tau_1^{ff} \right] \cdot \left(\frac{\partial \Delta}{\partial \theta_2} \right) \right\} \cdot \frac{1}{\Delta^2} +$$

$$\left(\begin{array}{l} \left\{ \left[c\theta_2 c\theta_3 s\theta_3 J_s^4 \right] \cdot \left(-\frac{\partial \tau_2^{ff}}{\partial \theta_2} \right) - \left[s\theta_2 c\theta_3 s\theta_3 J_s^4 \right] \cdot \left[\tau_2 - s\theta_3\tau_4 - \tau_2^{ff} \right] \right\} \cdot \Delta - \\[6pt] \left[c\theta_2 c\theta_3 s\theta_3 J_s^4 \right] \cdot \left[\tau_2 - s\theta_3\tau_4 - \tau_2^{ff} \right] \cdot \left(\frac{\partial \Delta}{\partial \theta_2} \right) \end{array} \right) \cdot \frac{1}{\Delta^2}$$

$$A_{1,7} = \left(\begin{array}{l} \left\{ J_{mx}\left[c\theta_2 s\theta_3\tau_4 - \left(\frac{\partial \tau_1^{ff}}{\partial \theta_3} \right) \right] + \left[\tau_1 - s\theta_2\tau_3 - c\theta_2 c\theta_3\tau_4 - \tau_1^{ff} \right] \cdot \left(\frac{\partial J_{mx}}{\partial \theta_3} \right) \right\} \cdot \Delta - \\[6pt] J_{mx}\left[\tau_1 - s\theta_2\tau_3 - c\theta_2 c\theta_3\tau_4 - \tau_1^{ff} \right] \cdot \left(\frac{\partial \Delta}{\partial \theta_3} \right) \end{array} \right) \cdot \frac{1}{\Delta^2} +$$

$$\left(\begin{array}{l} \left\{ \left[c\theta_2 c\theta_3 s\theta_3 J_s^4 \right] \cdot \left[-c\theta_3\tau_4 - \left(\frac{\partial \tau_2^{ff}}{\partial \theta_3} \right) \right] + \left[c\theta_2 c\theta_3^2 J_s^4 \right] \cdot \left[\tau_2 - s\theta_3\tau_4 - \tau_2^{ff} \right] \right\} \cdot \Delta - \\[6pt] \left[c\theta_2 c\theta_3 s\theta_3 J_s^4 \right] \cdot \left[\tau_2 - s\theta_3\tau_4 - \tau_2^{ff} \right] \cdot \left(\frac{\partial \Delta}{\partial \theta_3} \right) \end{array} \right) \cdot \frac{1}{\Delta^2}$$

$$A_{2,5} = -\frac{c\theta_2 c\theta_3 s\theta_3 J_s^4}{\Delta}\left(\frac{\partial \tau_1^{ff}}{\partial \theta_1} \right) - \frac{J_{ox}}{\Delta}\left(\frac{\partial \tau_2^{ff}}{\partial \theta_1} \right)$$

$$A_{2,6} = \left(\begin{array}{l} \left\{ \begin{array}{l} \left[c\theta_2 c\theta_3 s\theta_3 J_s^4 \right] \cdot \left[-c\theta_2\tau_3 + s\theta_2 c\theta_3\tau_4 - \left(\frac{\partial \tau_1^{ff}}{\partial \theta_2} \right) \right] - \\[6pt] \left[s\theta_2 c\theta_3 s\theta_3 J_s^4 \right] \cdot \left[\tau_1 - s\theta_2\tau_3 - c\theta_2 c\theta_3\tau_4 - \tau_1^{ff} \right] \end{array} \right\} \cdot \Delta - \\[12pt] \left[c\theta_2 c\theta_3 s\theta_3 J_s^4 \right] \cdot \left[\tau_1 - s\theta_2\tau_3 - c\theta_2 c\theta_3\tau_4 - \tau_1^{ff} \right] \cdot \left(\frac{\partial \Delta}{\partial \theta_2} \right) \end{array} \right) \cdot \frac{1}{\Delta^2} +$$

$$\left(\left\{ J_{ox}\left(-\frac{\partial \tau_2^{ff}}{\partial \theta_2} \right) + \left[\tau_2 - s\theta_3\tau_4 - \tau_2^{ff} \right] \cdot \left(\frac{\partial J_{ox}}{\partial \theta_2} \right) \right\} \cdot \Delta - J_{ox}\left[\tau_2 - s\theta_3\tau_4 - \tau_2^{ff} \right] \cdot \left(\frac{\partial \Delta}{\partial \theta_2} \right) \right) \cdot \frac{1}{\Delta^2}$$

$$A_{2,7} = \left\{ \begin{array}{l} \left\{ \begin{array}{l} \left[c\theta_2 c\theta_3 s\theta_3 J_s^4 \right] \cdot \left[c\theta_2 s\theta_3 \tau_4 - \left(\dfrac{\partial \tau_1^{ff}}{\partial \theta_3} \right) \right] + \\[4mm] \left[c\theta_2 J_s^4 \right] \cdot \left[c\theta_3^2 - s\theta_3^2 \right] \cdot \left[\tau_1 - s\theta_2 \tau_3 - c\theta_2 c\theta_3 \tau_4 - \tau_1^{ff} \right] \end{array} \right\} \cdot \Delta - \\[10mm] \left[c\theta_2 c\theta_3 s\theta_3 J_s^4 \right] \cdot \left[\tau_1 - s\theta_2 \tau_3 - c\theta_2 c\theta_3 \tau_4 - \tau_1^{ff} \right] \cdot \left(\dfrac{\partial \Delta}{\partial \theta_3} \right) \end{array} \right\} \cdot \dfrac{1}{\Delta^2} +$$

$$\left\{ \begin{array}{l} \left\{ J_{ox} \left[-c\theta_3 \tau_4 - \left(\dfrac{\partial \tau_2^{ff}}{\partial \theta_3} \right) \right] + \left[\tau_2 - s\theta_3 \tau_4 - \tau_2^{ff} \right] \cdot \left(\dfrac{\partial J_{ox}}{\partial \theta_3} \right) \right\} \cdot \Delta - \\[10mm] J_{ox} \left[\tau_2 - s\theta_3 \tau_4 - \tau_2^{ff} \right] \cdot \left(\dfrac{\partial \Delta}{\partial \theta_3} \right) \end{array} \right\} \cdot \dfrac{1}{\Delta^2}$$

$$A_{3,5} = -\frac{1}{J_{ix}} \left(\frac{\partial \tau_3^{ff}}{\partial \theta_1} \right)$$

$$A_{3,6} = -\frac{1}{J_{ix}} \left(\frac{\partial \tau_3^{ff}}{\partial \theta_2} \right)$$

$$A_{3,7} = -\frac{1}{J_{ix}} \left(\frac{\partial \tau_3^{ff}}{\partial \theta_3} \right)$$

$$A_{5,1} = -1$$

$$A_{6,2} = -1$$

$$A_{6,5} = c\theta_1 \varpi_{cx} - s\theta_1 \varpi_{cy}$$

$$A_{7,1} = s\theta_2$$

$$A_{7,3} = -1$$

$$A_{7,5} = -s\theta_1 c\theta_2 \varpi_{cx} - c\theta_1 c\theta_2 \varpi_{cy}$$

$$A_{7,6} = c\theta_2 \varpi_{1x} - c\theta_1 s\theta_2 \varpi_{cx} + s\theta_1 s\theta_2 \varpi_{cy}$$

$$A_{8,1} = c\theta_2 c\theta_3$$

$$A_{8,1} = s\theta_3$$

$$A_{8,4} = -1$$

$$A_{8,5} = s\theta_1 s\theta_2 c\theta_3 \varpi_{cx} + c\theta_1 s\theta_2 c\theta_3 \varpi_{cy}$$

$$A_{8,6} = -s\theta_2 c\theta_3 \varpi_{1x} - c\theta_1 c\theta_2 c\theta_3 \varpi_{cx} + s\theta_1 c\theta_2 c\theta_3 \varpi_{cy}$$

$$A_{8,6} = -c\theta_2 s\theta_3 \varpi_{1x} + c\theta_3 \varpi_{2x} + c\theta_1 s\theta_2 s\theta_3 \varpi_{cx} - s\theta_1 s\theta_2 s\theta_3 \varpi_{cy}$$

$$B_{1,1} = \left[J_{mx} \right] \cdot \frac{1}{\Delta}$$

$$B_{1,2} = \left[c\theta_2 c\theta_3 s\theta_3 J_s^4 \right] \cdot \frac{1}{\Delta}$$

$$B_{1,3} = \left[-s\theta_2 J_{mx} \right] \cdot \frac{1}{\Delta}$$

$$B_{1,4} = \left[-c\theta_2 c\theta_3 J_{mx} - c\theta_2 c\theta_3 s\theta_3^2 J_s^4 \right] \cdot \frac{1}{\Delta}$$

$$B_{2,1} = \left[c\theta_2 c\theta_3 s\theta_3 J_s^4 \right] \cdot \frac{1}{\Delta}$$

154

$$B_{2,2} = [J_{ox}] \cdot \frac{1}{\Delta}$$

$$B_{2,3} = \left[- c\theta_2 s\theta_2 c\theta_3 s\theta_3 J_s^4\right] \cdot \frac{1}{\Delta}$$

$$B_{2,4} = \left[- s\theta_3 J_{ox} - c\theta_2^2 c\theta_3^2 s\theta_3 J_s^4\right] \cdot \frac{1}{\Delta}$$

$$B_{3,3} = \frac{1}{J_{ix}}$$

$$B_{4,4} = \frac{1}{J_s^4}$$

$$G_{1,1} = -\frac{J_{mx}}{\Delta}\left(\frac{\partial \tau_1^{ff}}{\partial \dot{\varpi}_{cx}}\right) - \frac{c\theta_2 c\theta_3 s\theta_3 J_s^4}{\Delta}\left(\frac{\partial \tau_2^{ff}}{\partial \dot{\varpi}_{cx}}\right)$$

$$G_{1,2} = -\frac{J_{mx}}{\Delta}\left(\frac{\partial \tau_1^{ff}}{\partial \dot{\varpi}_{cy}}\right) - \frac{c\theta_2 c\theta_3 s\theta_3 J_s^4}{\Delta}\left(\frac{\partial \tau_2^{ff}}{\partial \dot{\varpi}_{cy}}\right)$$

$$G_{1,4} = -\frac{J_{mx}}{\Delta}\left(\frac{\partial \tau_1^{ff}}{\partial \varpi_{cx}}\right) - \frac{c\theta_2 c\theta_3 s\theta_3 J_s^4}{\Delta}\left(\frac{\partial \tau_2^{ff}}{\partial \varpi_{cx}}\right)$$

$$G_{1,5} = -\frac{J_{mx}}{\Delta}\left(\frac{\partial \tau_1^{ff}}{\partial \varpi_{cy}}\right) - \frac{c\theta_2 c\theta_3 s\theta_3 J_s^4}{\Delta}\left(\frac{\partial \tau_2^{ff}}{\partial \varpi_{cy}}\right)$$

$$G_{1,6} = -\frac{J_{mx}}{\Delta}\left(\frac{\partial \tau_1^{ff}}{\partial \varpi_{cz}}\right) - \frac{c\theta_2 c\theta_3 s\theta_3 J_s^4}{\Delta}\left(\frac{\partial \tau_2^{ff}}{\partial \varpi_{cz}}\right)$$

$$G_{2,1} = -\frac{c\theta_2 c\theta_3 s\theta_3 J_s^4}{\Delta}\left(\frac{\partial \tau_1^{ff}}{\partial \dot{\varpi}_{cx}}\right) - \frac{J_{ox}}{\Delta}\left(\frac{\partial \tau_2^{ff}}{\partial \dot{\varpi}_{cx}}\right)$$

$$G_{2,2} = -\frac{c\theta_2 c\theta_3 s\theta_3 J_s^4}{\Delta}\left(\frac{\partial \tau_1^{ff}}{\partial \dot{\varpi}_{cy}}\right) - \frac{J_{ox}}{\Delta}\left(\frac{\partial \tau_2^{ff}}{\partial \dot{\varpi}_{cy}}\right)$$

$$G_{2,4} = -\frac{c\theta_2 c\theta_3 s\theta_3 J_s^4}{\Delta}\left(\frac{\partial \tau_1^{ff}}{\partial \varpi_{cx}}\right) - \frac{J_{ox}}{\Delta}\left(\frac{\partial \tau_2^{ff}}{\partial \varpi_{cx}}\right)$$

$$G_{2,5} = -\frac{c\theta_2 c\theta_3 s\theta_3 J_s^4}{\Delta}\left(\frac{\partial \tau_1^{ff}}{\partial \varpi_{cy}}\right) - \frac{J_{ox}}{\Delta}\left(\frac{\partial \tau_2^{ff}}{\partial \varpi_{cy}}\right)$$

$$G_{2,6} = -\frac{c\theta_2 c\theta_3 s\theta_3 J_s^4}{\Delta}\left(\frac{\partial \tau_1^{ff}}{\partial \varpi_{cz}}\right) - \frac{J_{ox}}{\Delta}\left(\frac{\partial \tau_2^{ff}}{\partial \varpi_{cz}}\right)$$

$$G_{5,6} = 1$$

$$G_{6,4} = s\theta_1$$

$$G_{6,5} = c\theta_1$$

$$G_{7,4} = c\theta_1 c\theta_2$$

$$G_{7,5} = -s\theta_1 c\theta_2$$

$$G_{8,4} = -c\theta_1 s\theta_2 c\theta_3$$

$$G_{8,5} = s\theta_1 s\theta_2 c\theta_3$$

Appendix C Nominal Gimbal Angle Calculation

As discussed in section 2.3, it is possible to transform between the body-fixed gimbal reference frames by taking the product of a series of Direction Cosine Matrices or DCM. Using (2.3.1), the appropriate transformation from the UVW platform frame to the RPY missile frame is as follows. The UVW platform frame will be denoted with a UP, and the RPY missile frame with an XM.

$$T_{UP}^{XM} = \begin{bmatrix} 0 & 0 & -1 \\ 0 & 1 & 0 \\ 1 & 0 & 0 \end{bmatrix} \cdot \begin{bmatrix} 0 & c\theta_1 & s\theta_1 \\ 0 & -s\theta_1 & c\theta_1 \\ 1 & 0 & 0 \end{bmatrix} \cdot \begin{bmatrix} 0 & c\theta_2 & s\theta_2 \\ 0 & -s\theta_2 & c\theta_2 \\ 1 & 0 & 0 \end{bmatrix} \cdot \begin{bmatrix} 0 & c\theta_3 & s\theta_3 \\ 0 & -s\theta_3 & c\theta_3 \\ 1 & 0 & 0 \end{bmatrix} \cdot \begin{bmatrix} 0 & c\theta_4 & s\theta_4 \\ 0 & -s\theta_4 & c\theta_4 \\ 1 & 0 & 0 \end{bmatrix} \cdot \begin{bmatrix} 0 & 0 & 1 \\ 1 & 0 & 0 \\ 0 & 1 & 0 \end{bmatrix} \quad (C.1)$$

Here and elsewhere, the following notation is used.

$$c\theta_i = \cos(\theta_i) \quad (C.2)$$

$$s\theta_i = \sin(\theta_i) \quad (C.3)$$

Notice equation (C.1) contains the standard DCM between the gimbals as well as fixed permutation matrices which are a consequence of the definition of the RPY and UVW frames as related to the XYZ gimbal frames. The terms of the resulting transformation matrix are presented below.

$$T_{UP}^{XM}(1,1) = -c\theta_2 s\theta_3 s\theta_4 - s\theta_2 c\theta_4 \quad (C.4)$$

$$T_{UP}^{XM}(2,1) = -s\theta_1 \left\{ -s\theta_2 s\theta_3 s\theta_4 + c\theta_2 c\theta_4 \right\} - c\theta_1 c\theta_3 s\theta_4 \quad (C.5)$$

$$T_{UP}^{XM}(3,1) = c\theta_1\{-s\theta_2 s\theta_3 s\theta_4 + c\theta_2 c\theta_4\} - s\theta_1 c\theta_3 s\theta_4 \qquad \text{(C.6)}$$

$$T_{UP}^{XM}(1,2) = c\theta_2 s\theta_3 c\theta_4 - s\theta_2 s\theta_4 \qquad \text{(C.7)}$$

$$T_{UP}^{XM}(2,2) = -s\theta_1\{s\theta_2 s\theta_3 c\theta_4 + c\theta_2 s\theta_4\} + c\theta_1 c\theta_3 c\theta_4 \qquad \text{(C.8)}$$

$$T_{UP}^{XM}(3,2) = c\theta_1\{s\theta_2 s\theta_3 c\theta_4 + c\theta_2 s\theta_4\} + s\theta_1 c\theta_3 c\theta_4 \qquad \text{(C.9)}$$

$$T_{UP}^{XM}(1,3) = -c\theta_2 c\theta_3 \qquad \text{(C.10)}$$

$$T_{UP}^{XM}(2,3) = s\theta_1 s\theta_2 c\theta_3 + c\theta_1 s\theta_3 \qquad \text{(C.11)}$$

$$T_{UP}^{XM}(3,3) = -c\theta_1 s\theta_2 c\theta_3 + s\theta_1 s\theta_3 \qquad \text{(C.12)}$$

With the middle or inner angle equal to zero or π, some of the various terms in the equations above become zero or one. For these special gimbal configurations, wherein lambda is zero, simplified equations for the transformation matrix containing only the three remaining gimbal angles can be obtained. The cases will be treated individually.

First, for $\theta_2 = 0$, the following equations are obtained.

$$T_{UP}^{XM}(1,1) = -s\theta_3 s\theta_4 \qquad \text{(C.13)}$$

$$T_{UP}^{XM}(1,2) = s\theta_3 c\theta_4 \qquad \text{(C.14)}$$

$$T_{UP}^{XM}(1,3) = -c\theta_3 \qquad \text{(C.15)}$$

$$T_{UP}^{XM}(2,3) = c\theta_1 s\theta_3 \qquad \text{(C.16)}$$

158

$$T_{UP}^{XM}(3,3) = s\theta_1 s\theta_3 \qquad\qquad (C.17)$$

Given these five equations, it is desired to compute three angles. Clearly this will involve inverse trigonometric functions. It is desired to keep all angles in the following range.

$$-\pi \leq \theta_i \leq \pi \qquad\qquad (C.18)$$

To maintain the range given in (C.18), a four-quadrant inverse tangent function is used. Care must be taken when using the four-quadrant inverse tangent, as the signs of the numerators and denominators determine the correct quadrant and therefore must be preserved. Hence, the first step in solving for the angles is to move terms to the left hand side in equations (C.13) to (C.17).

$$T_{UP}^{XM}(3,3)/s\theta_3 = s\theta_1 \qquad\qquad (C.19)$$

$$T_{UP}^{XM}(2,3)/s\theta_3 = c\theta_1 \qquad\qquad (C.20)$$

$$T_{UP}^{XM}(2,3)/c\theta_1 = s\theta_3 \qquad\qquad (C.21)$$

$$-T_{UP}^{XM}(1,3) = c\theta_3 \qquad\qquad (C.22)$$

$$-T_{UP}^{XM}(1,1)/s\theta_3 = s\theta_4 \qquad\qquad (C.23)$$

$$T_{UP}^{XM}(1,2)/s\theta_3 = c\theta_4 \qquad\qquad (C.24)$$

Now, to solve for the outer gimbal angle, (C.19) can be divided by (C.20) and the inverse tangent taken. This solution is as follows.

159

$$\theta_1 = \tan^{-1}\left\{\frac{T_{UP}^{XM}(3,3)}{T_{UP}^{XM}(2,3)}\right\} \qquad\qquad \text{(C.25)}$$

In (C.25), it appears that it is acceptable to cancel the sine term, as it appears in both the numerator and denominator. As long as the sine of the inner gimbal angle is positive, it is in fact acceptable to make this cancellation. However, in the case that the sine is negative, the correct answer for the outer gimbal angle would be computed as follows.

$$\theta_1 = \tan^{-1}\left\{\frac{-T_{UP}^{XM}(3,3)}{-T_{UP}^{XM}(2,3)}\right\} \qquad\qquad \text{(C.26)}$$

This then leaves two possible answers for the outer gimbal angle, different by 180 degrees. However, when choosing the nominal outer angle, the choice between these two solutions can be properly taken as the solution which is closest to the current outer gimbal angle.

A similar situation to the outer gimbal angle exists when calculating the nominal platform gimbal angle by dividing (C.23) by (C.24) and taking the inverse tangent. This leaves the two solutions below. Although a nominal platform gimbal angle is not used in the lambda controller, if it were needed it could be chosen based on the current platform gimbal angle.

$$\theta_4 = \tan^{-1}\left\{\frac{-T_{UP}^{XM}(1,1)}{T_{UP}^{XM}(1,2)}\right\}, \quad s\theta_3 > 0 \qquad\qquad \text{(C.27)}$$

$$\theta_4 = \tan^{-1}\left\{\frac{T_{UP}^{XM}(1,1)}{-T_{UP}^{XM}(1,2)}\right\}, \quad s\theta_3 < 0 \qquad\qquad \text{(C.28)}$$

Finally, solving for the inner gimbal angle is done by dividing (C.21) by (C.22) and taking the inverse tangent as follows. Again, the inner angle is not needed for the lambda controller, but the solution is presented here for completeness.

$$\theta_3 = \tan^{-1}\left\{ \frac{T_{UP}^{XM}(2,3)/c\theta_1}{-T_{UP}^{XM}(1,3)} \right\} \qquad (C.29)$$

Unlike for the outer and platform calculations, in (C.29), the cosine term is not cancelled by a term in the denominator. This prevents the positive versus negative problem encountered previously, but introduces a new problem. For outer gimbal angles where the cosine of the angle is zero, the numerator in (C.29) is undefined and the solution fails. In these instances, a different solution is needed. This second solution can be derived using a different term as follows.

$$T_{UP}^{XM}(3,3)/s\theta_1 = s\theta_3 \qquad (C.30)$$

Now, by dividing (C.30) above, by (C.22) and taking the inverse tangent, the inner gimbal angle can be determined as follows.

$$\theta_3 = \tan^{-1}\left\{ \frac{T_{UP}^{XM}(3,3)/s\theta_1}{-T_{UP}^{XM}(1,3)} \right\} \qquad (C.31)$$

The choice between the two solutions given in (C.29) and (C.31) is straightforward. For outer gimbal angles where the cosine of the angle approaches zero, the sine of the angle will approach one, and (C.31) can be used. Elsewhere, (C.29) can be used.

Following are the solutions for the nominal angles for the remaining lambda-nulling conditions. As these solutions are very similar to those presented above, little explanation will be given and only the simplifications and dual solutions will be reported.

For $\theta_2 = \pi$, the simplifications are thus.

$$T_{UP}^{XM}(1,1) = s\theta_3 s\theta_4 \tag{C.32}$$

$$T_{UP}^{XM}(1,2) = -s\theta_3 c\theta_4 \tag{C.33}$$

$$T_{UP}^{XM}(1,3) = c\theta_3 \tag{C.34}$$

$$T_{UP}^{XM}(2,3) = c\theta_1 s\theta_3 \tag{C.35}$$

$$T_{UP}^{XM}(3,3) = s\theta_1 s\theta_3 \tag{C.36}$$

The following are solutions for the nominal gimbal angles.

$$\theta_1 = \tan^{-1}\left\{\frac{T_{UP}^{XM}(3,3)}{T_{UP}^{XM}(2,3)}\right\}, \quad s\theta_3 > 0 \tag{C.37}$$

$$\theta_1 = \tan^{-1}\left\{\frac{-T_{UP}^{XM}(3,3)}{-T_{UP}^{XM}(2,3)}\right\}, \quad s\theta_3 < 0 \tag{C.38}$$

$$\theta_3 = \tan^{-1}\left\{\frac{T_{UP}^{XM}(2,3)/c\theta_1}{T_{UP}^{XM}(1,3)}\right\}, \quad c\theta_1 \neq 0 \tag{C.39}$$

$$\theta_3 = \tan^{-1}\left\{\frac{T_{UP}^{XM}(3,3)/s\theta_1}{T_{UP}^{XM}(1,3)}\right\}, \quad c\theta_1 \approx 0 \tag{C.40}$$

$$\theta_4 = \tan^{-1}\left\{\frac{T_{UP}^{XM}(1,1)}{-T_{UP}^{XM}(1,2)}\right\}, \quad s\theta_3 > 0 \tag{C.41}$$

$$\theta_4 = \tan^{-1}\left\{\frac{-T_{UP}^{XM}(1,1)}{T_{UP}^{XM}(1,2)}\right\}, \quad s\theta_3 < 0 \tag{C.42}$$

For $\theta_3 = 0$, the simplifications are as follows.

$$T_{UP}^{XM}(1,1) = -s\theta_2 c\theta_4 \tag{C.43}$$

$$T_{UP}^{XM}(1,2) = -s\theta_2 s\theta_4 \tag{C.44}$$

$$T_{UP}^{XM}(1,3) = -c\theta_2 \tag{C.45}$$

$$T_{UP}^{XM}(2,3) = s\theta_1 s\theta_2 \tag{C.46}$$

$$T_{UP}^{XM}(3,3) = -c\theta_1 s\theta_2 \tag{C.47}$$

Again, the solutions are similar.

$$\theta_1 = \tan^{-1}\left\{\frac{T_{UP}^{XM}(2,3)}{-T_{UP}^{XM}(3,3)}\right\}, \quad s\theta_2 > 0 \tag{C.48}$$

$$\theta_1 = \tan^{-1}\left\{\frac{-T_{UP}^{XM}(2,3)}{T_{UP}^{XM}(3,3)}\right\}, \quad s\theta_2 < 0 \tag{C.49}$$

$$\theta_2 = \tan^{-1}\left\{\frac{-T_{UP}^{XM}(3,3)/c\theta_1}{-T_{UP}^{XM}(1,3)}\right\}, \quad c\theta_1 \neq 0 \tag{C.50}$$

$$\theta_2 = \tan^{-1}\left\{\frac{T_{UP}^{XM}(2,3)/s\theta_1}{-T_{UP}^{XM}(1,3)}\right\}, \quad c\theta_1 \approx 0 \tag{C.51}$$

163

$$\theta_4 = \tan^{-1}\left\{\frac{-T_{UP}^{XM}(1,2)}{-T_{UP}^{XM}(1,1)}\right\}, \quad s\theta_2 > 0 \tag{C.52}$$

$$\theta_4 = \tan^{-1}\left\{\frac{T_{UP}^{XM}(1,2)}{T_{UP}^{XM}(1,1)}\right\}, \quad s\theta_2 < 0 \tag{C.53}$$

Finally, for $\theta_3 = \pi$ the simplifications are as expected.

$$T_{UP}^{XM}(1,1) = -s\theta_2 c\theta_4 \tag{C.54}$$

$$T_{UP}^{XM}(1,2) = -s\theta_2 s\theta_4 \tag{C.55}$$

$$T_{UP}^{XM}(1,3) = c\theta_2 \tag{C.56}$$

$$T_{UP}^{XM}(2,3) = -s\theta_1 s\theta_2 \tag{C.57}$$

$$T_{UP}^{XM}(3,3) = c\theta_1 s\theta_2 \tag{C.58}$$

And, the solutions follow.

$$\theta_1 = \tan^{-1}\left\{\frac{-T_{UP}^{XM}(2,3)}{T_{UP}^{XM}(3,3)}\right\}, \quad s\theta_2 > 0 \tag{C.59}$$

$$\theta_1 = \tan^{-1}\left\{\frac{T_{UP}^{XM}(2,3)}{-T_{UP}^{XM}(3,3)}\right\}, \quad s\theta_2 < 0 \tag{C.60}$$

$$\theta_2 = \tan^{-1}\left\{\frac{T_{UP}^{XM}(3,3)/c\theta_1}{T_{UP}^{XM}(1,3)}\right\}, \quad c\theta_1 \neq 0 \tag{C.61}$$

$$\theta_2 = \tan^{-1} \left\{ \frac{-T_{UP}^{XM}(2,3)/s\theta_1}{T_{UP}^{XM}(1,3)} \right\}, \quad c\theta_1 \approx 0 \tag{C.62}$$

$$\theta_4 = \tan^{-1} \left\{ \frac{-T_{UP}^{XM}(1,2)}{-T_{UP}^{XM}(1,1)} \right\}, \quad s\theta_2 > 0 \tag{C.63}$$

$$\theta_4 = \tan^{-1} \left\{ \frac{T_{UP}^{XM}(1,2)}{T_{UP}^{XM}(1,1)} \right\}, \quad s\theta_2 < 0 \tag{C.64}$$

Note that above, all solutions for the gimbal angles are in terms of inverse tangents. This is to preserve a consistent range as given in (C.18). Also note that the solutions presented here are not exclusive, but rather are the analytically simplest forms of solution which preserve the inverse tangent function.

To calculate the nominal gimbal angles the assumption is made that the platform orientation, and thus T_{UP}^{XM}, remains constant. The gyro controllers ensure that the platform maintains a constant orientation thus, this is a good assumption. As all the gimbal angles are readily measured with the resolvers, the transformation matrix is known. By applying the logic discussed above and in section 4.4.3 to choose which angle to null and hence which set of equations to use, the outer and middle nominal gimbal angles can be calculated using the measured values of the transformation matrix, and the equations above.

This page intentionally left blank.

Appendix D Simulink Diagrams

Following are diagrams of the two simulation models incorporating the classical and LQR controllers. These block diagrams are functional models in Matlab Simulink from which the results in Chapter 5 have been generated. The diagrams presented below are not intended to be a comprehensive documentation of the Simulink models. Only areas of interest to the two control schemes will be presented.
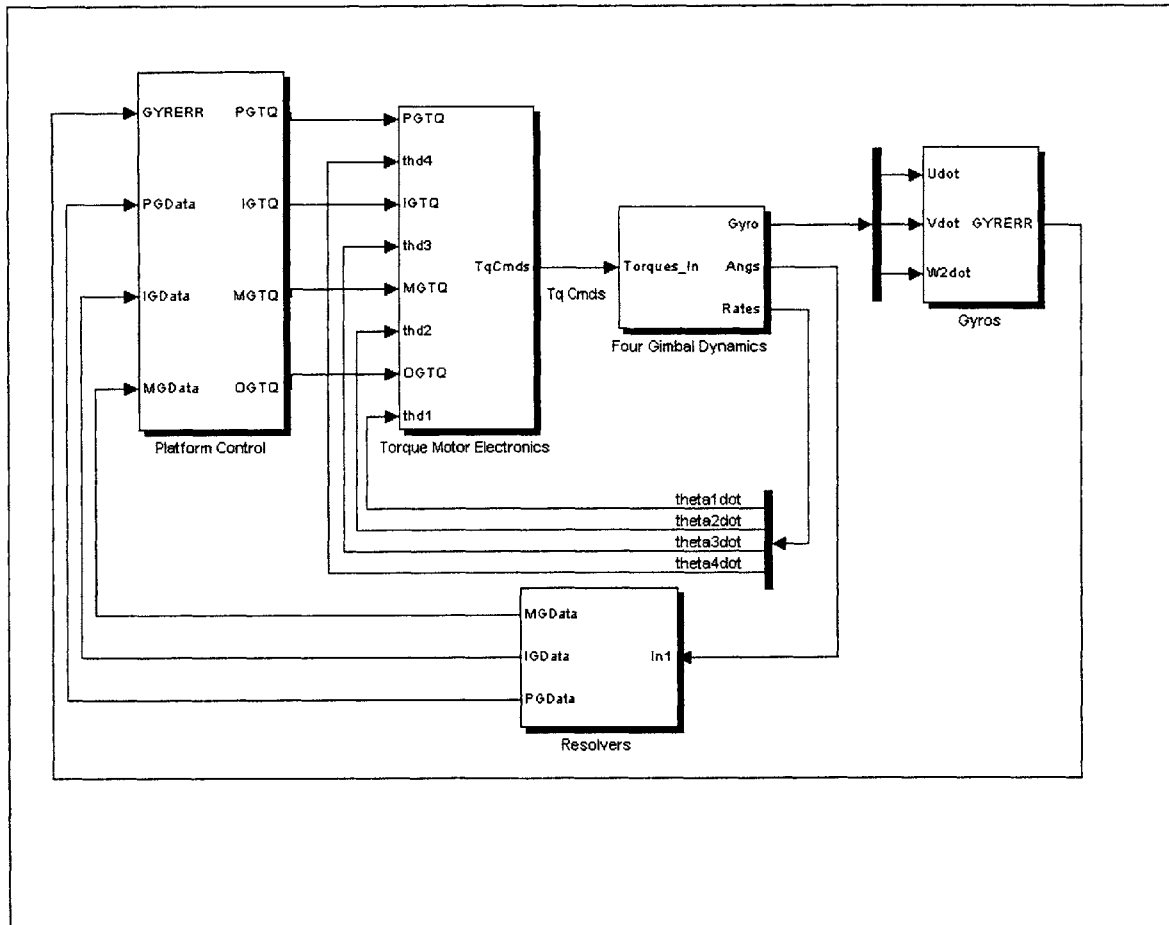
Figure D.1 - Block diagram overview of the four gimbal classical control model.

Figure D.1 above shows the top level of the Simulink model for the classical controller. This diagram shows the platform controller, as well as the models for the torque motors,

four gimbal dynamics, gyros and resolvers and is equivalent to Figure 2.1.2. Only the platform control block from Figure D.1 above will be examined in further detail below.
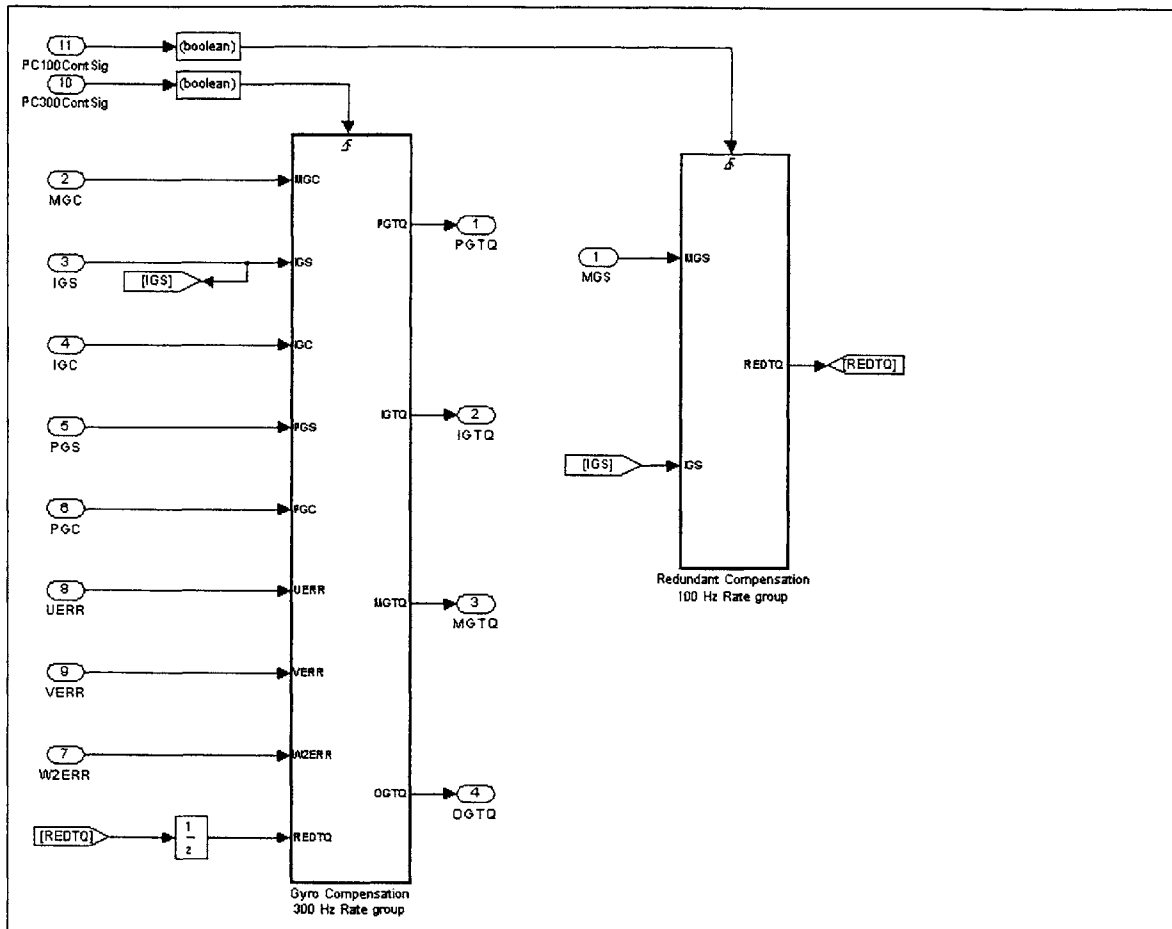
Figure D.2 - Block diagram of the multi-axis gyro and redundant compensators.

Figure D.2 above is contained within the platform control block of Figure D.1. In Figure D.2, the two separate controllers for the gyros and the redundant loop can be observed. It can be noted that the controllers operate at different frequencies, as pictured in the diagram.
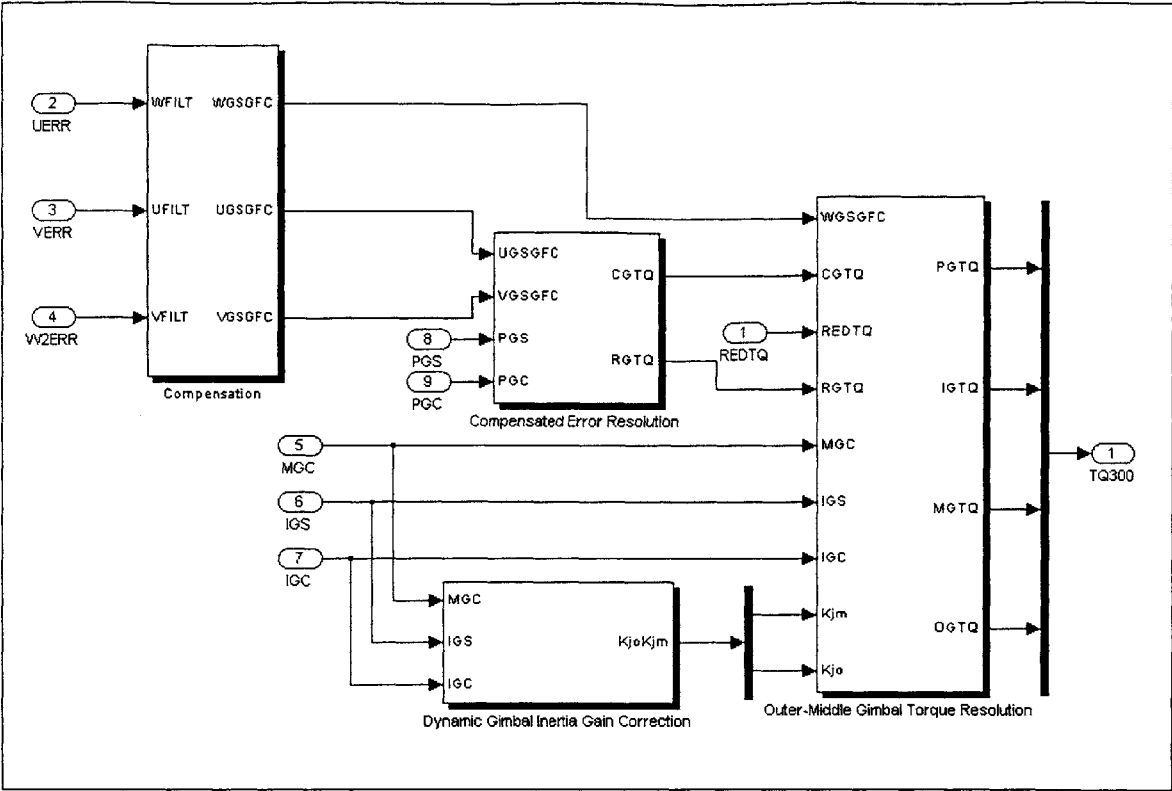
Figure D.3 - Block diagram of the gyro error compensator.

Figure D.3 shows the multi-axis gyro error compensator as described in section 3.2.2. The figures which follow will show each of the blocks present in Figure D.3. A functional description of all of these blocks can be found in Chapter 3.
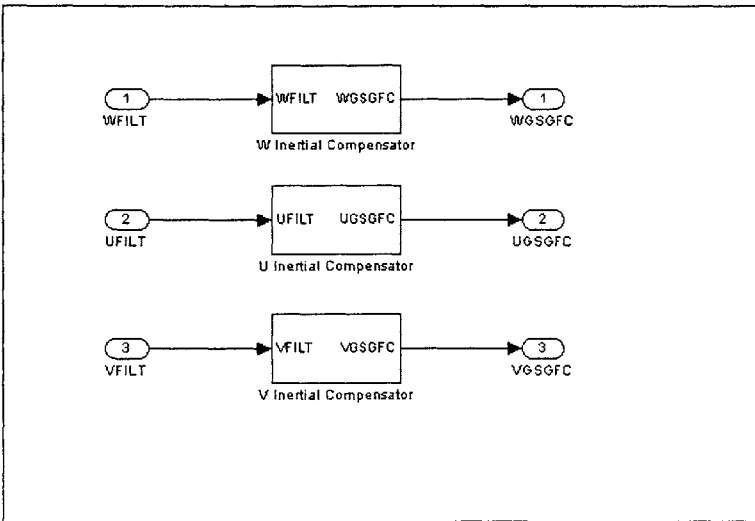
Figure D.4 - Block diagram of the compensation block.

169
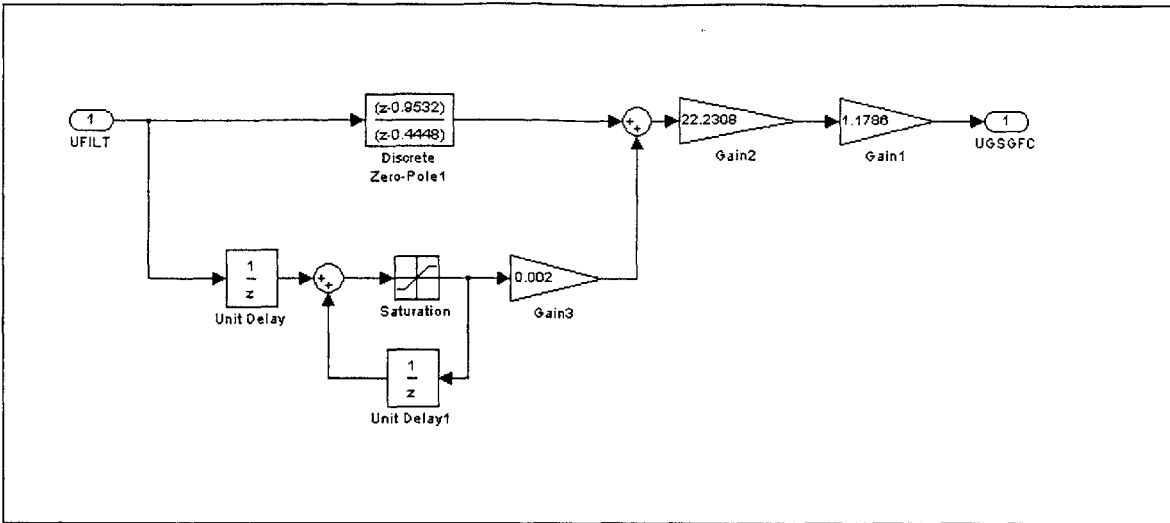
Figure D.5 - Block diagram of the U gyro compensator.
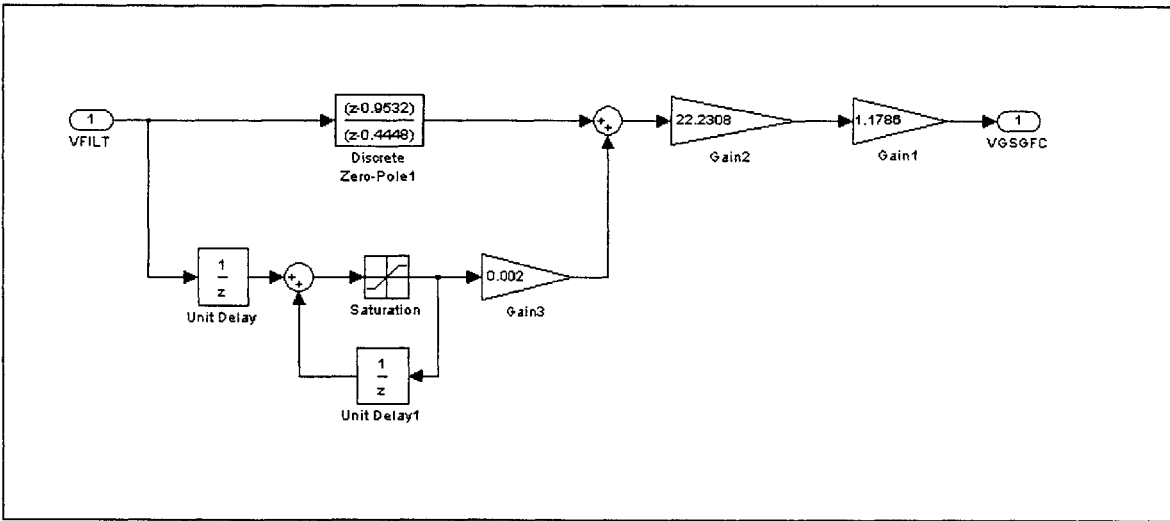
Figure D.6 - Block diagram of the V gyro compensator.
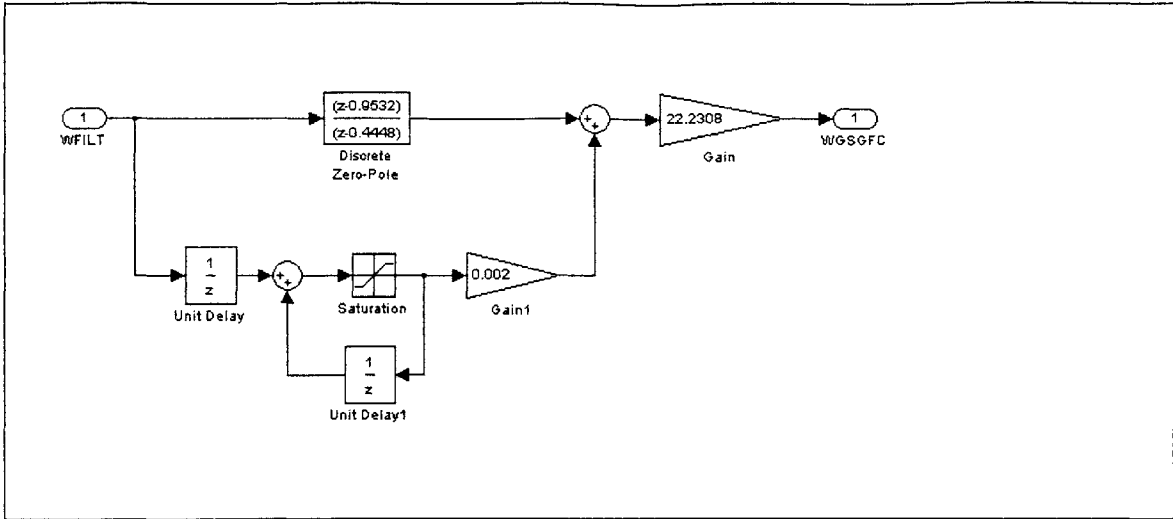
Figure D.7 - Block diagram of the *W* gyro compensator.
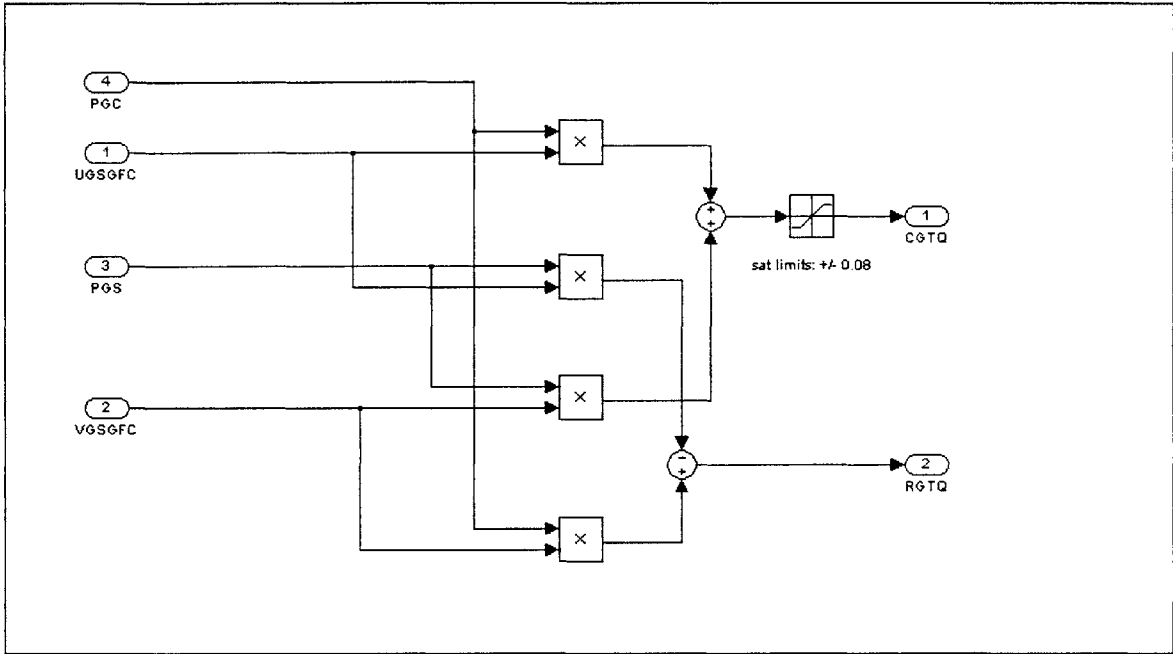
Figure D.8 - Block diagram of the compensated error resolution.
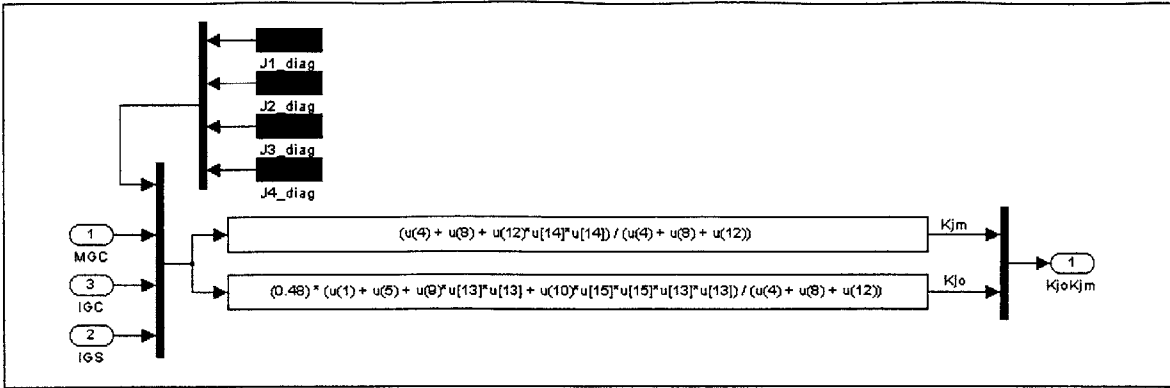
Figure D.9 - Block diagram of the dynamic gimbal inertia gain correction.
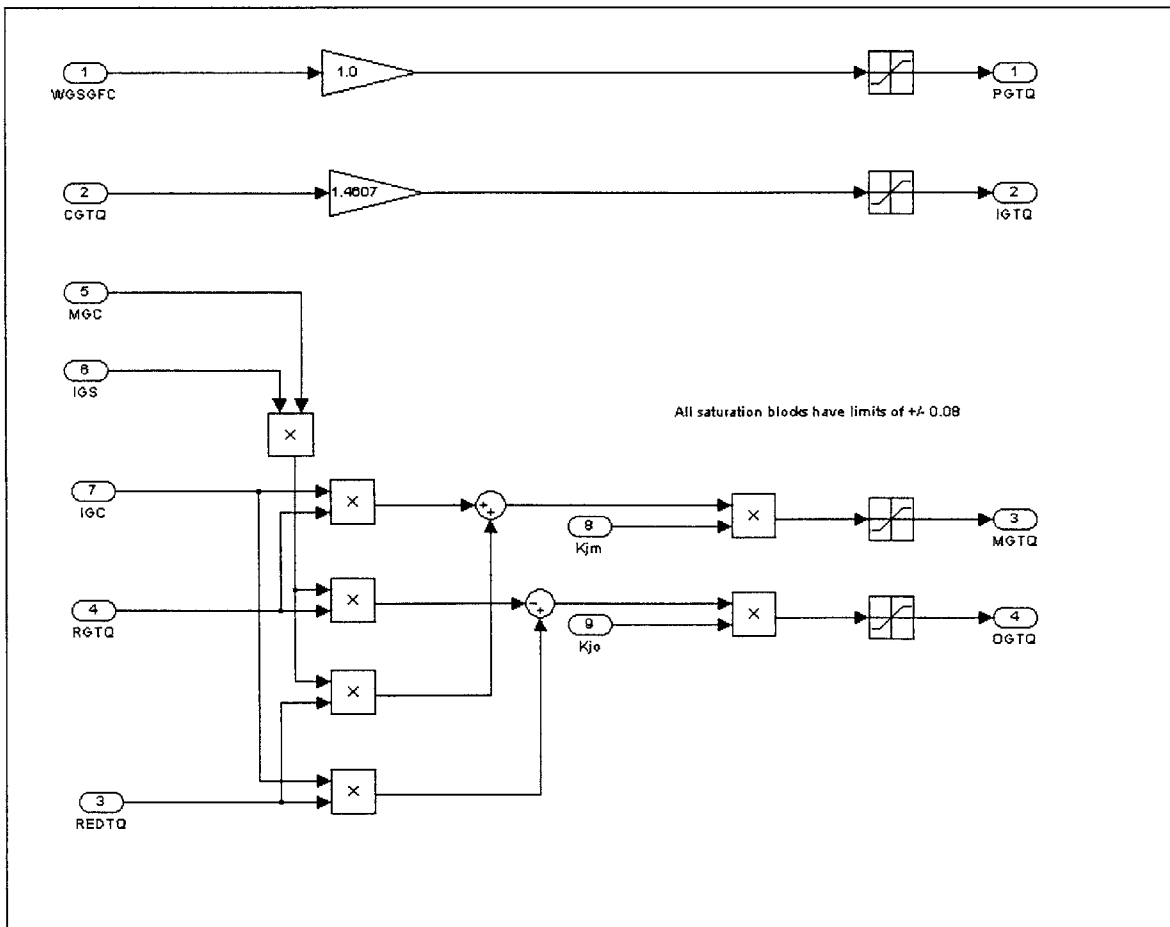
Figure D.10 - Block diagram of the outer-middle gimbal torque resolution.

The following figures depict the redundant compensation block of Figure D.2.
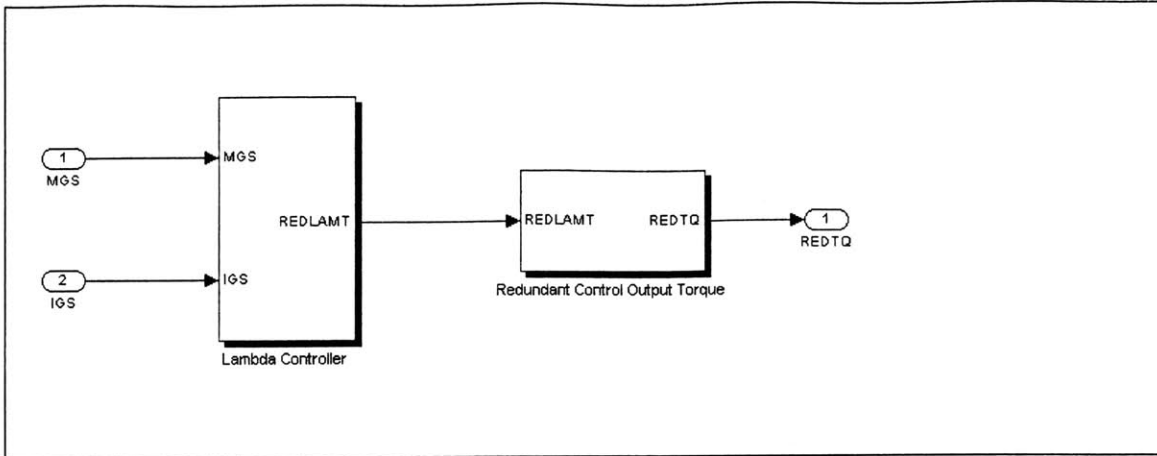
Figure D.11 - Block diagram of the redundant compensator.

This block executes the following pseudocode:
%   if ((dabs(U1(0))-dabs(U2(0))) > sin(0.05))   { Q1 = 1. ; } %
%   if ((dabs(U1(0))-dabs(U2(0))) < -sin(0.05))   { Q1 = -1. ; } %
%   REDLAMT = Q1*U3(0) ;   %
where U3(0) represents the output of the lambda compensation gain block
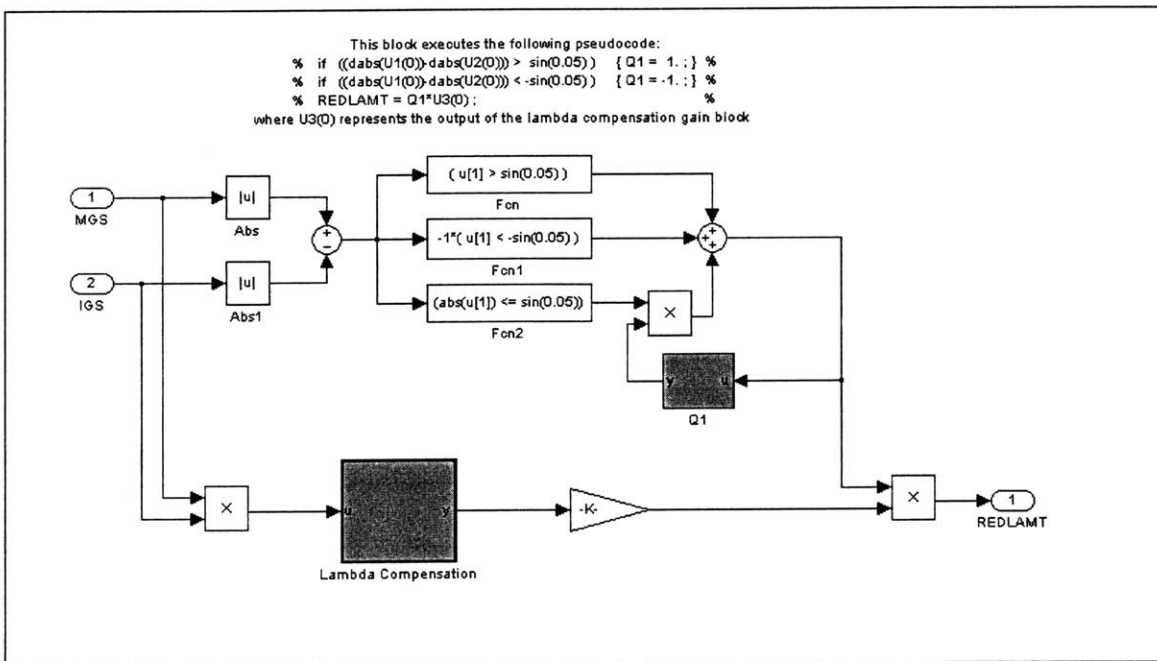
Figure D.12 - Block diagram of the lambda controller.

sat limits: +/- 0.044
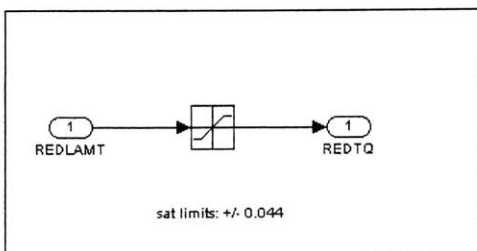
Figure D.13 - Block diagram of the redundant control output torque.

Next, block diagrams for the LQR controller will be presented. Some of the diagrams for the LQR controller are equivalent to the diagrams above for the classical controller. Where this is the case, the diagrams will not be repeated.
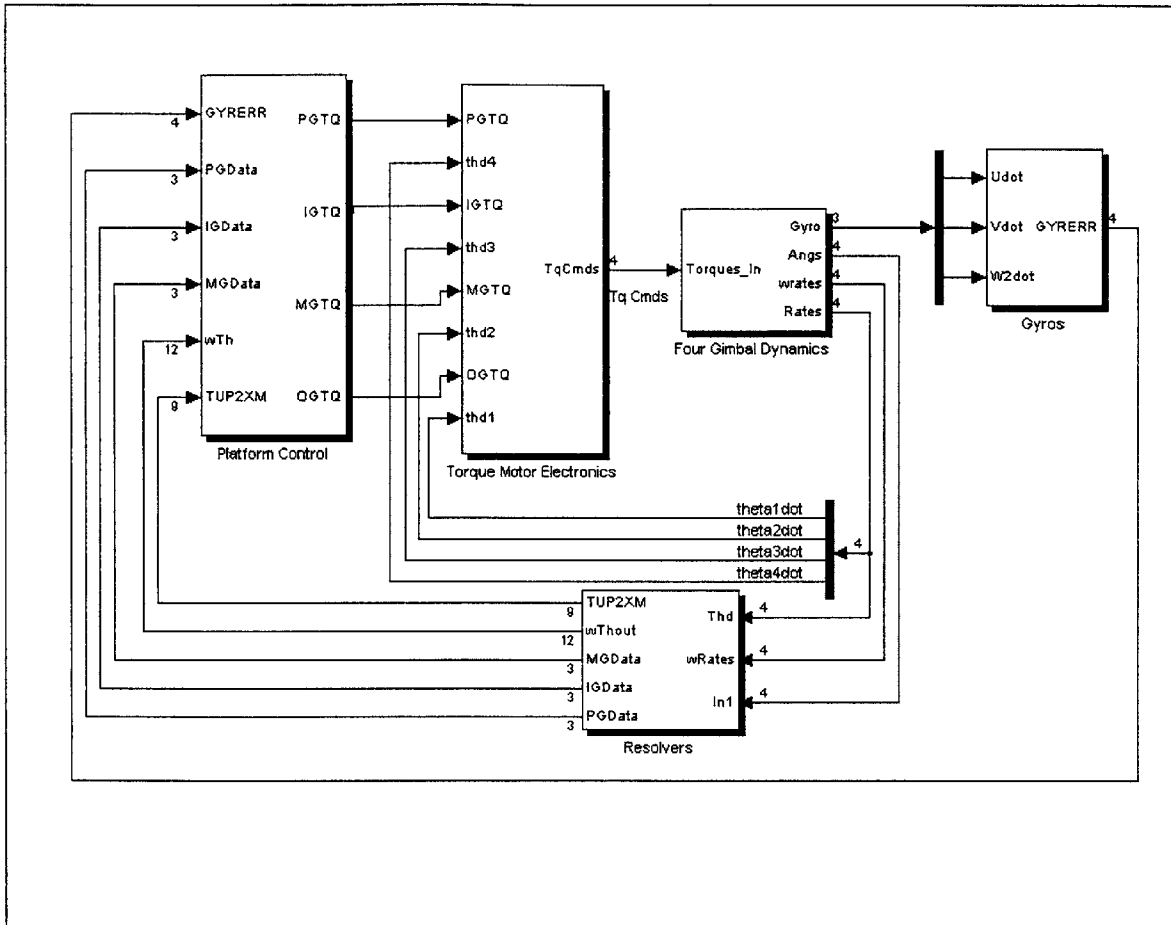
Figure D.14 - Block diagram overview of the four gimbal LQR control model.

Figure D.14 above is the overview for the LQR controller. One notable difference when compared with the classical controller in Figure D.1 is the presence of the TUP2XM. This is required for the calculation of the nominal conditions as discussed in section 4.4.3.

Figure D.2 is essentially identical for the LQR controller and will not be repeated here. In addition, all the multi-axis gyro compensator figures are the same, as the same

174

compensation is used for both the classical and LQR controllers, with the exception of the outer-middle gimbal torque resolution block which is depicted below.
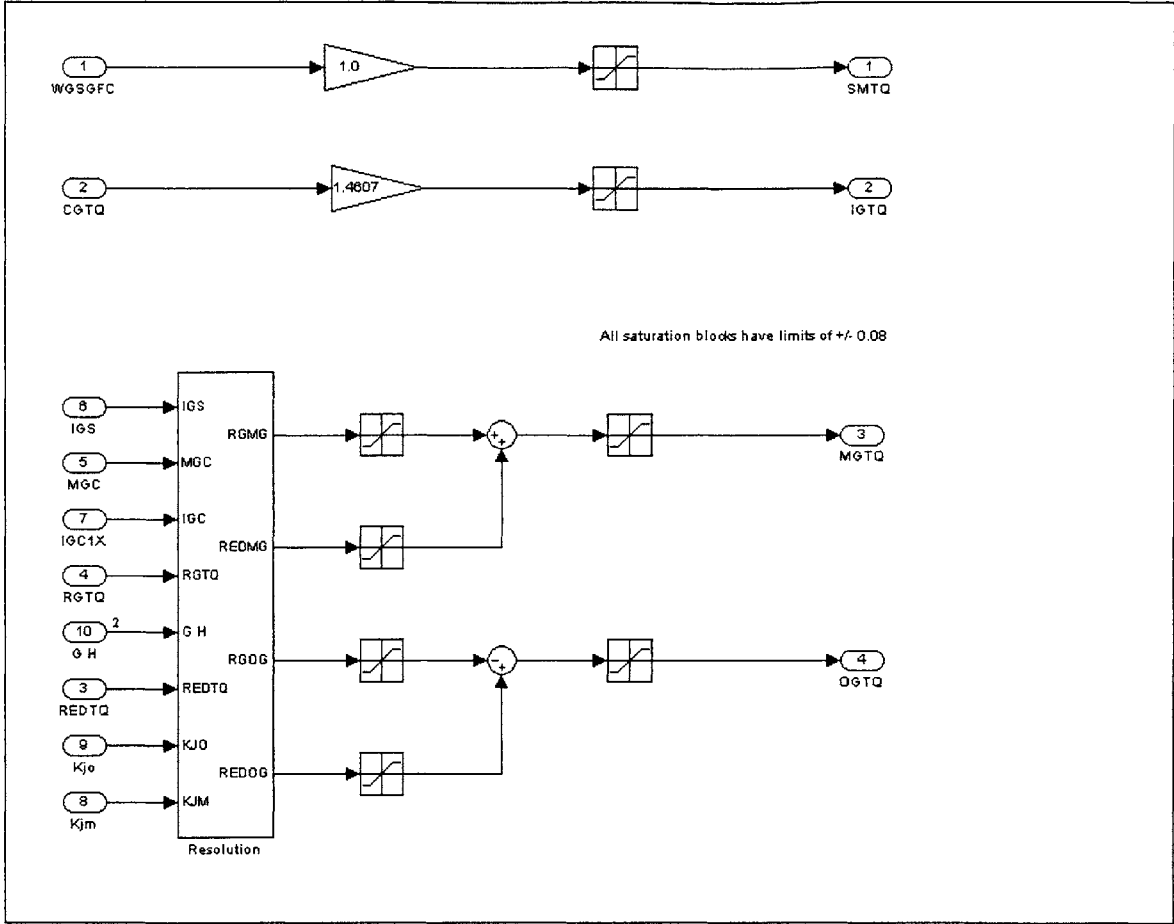
Figure D.15 - Block diagram of the outer-middle gimbal torque resolution for the LQR controller.

In Figure D.15 above, the resolution block now contains everything necessary to add the redundant command to the gyro compensation commands. The resolution block appears below.
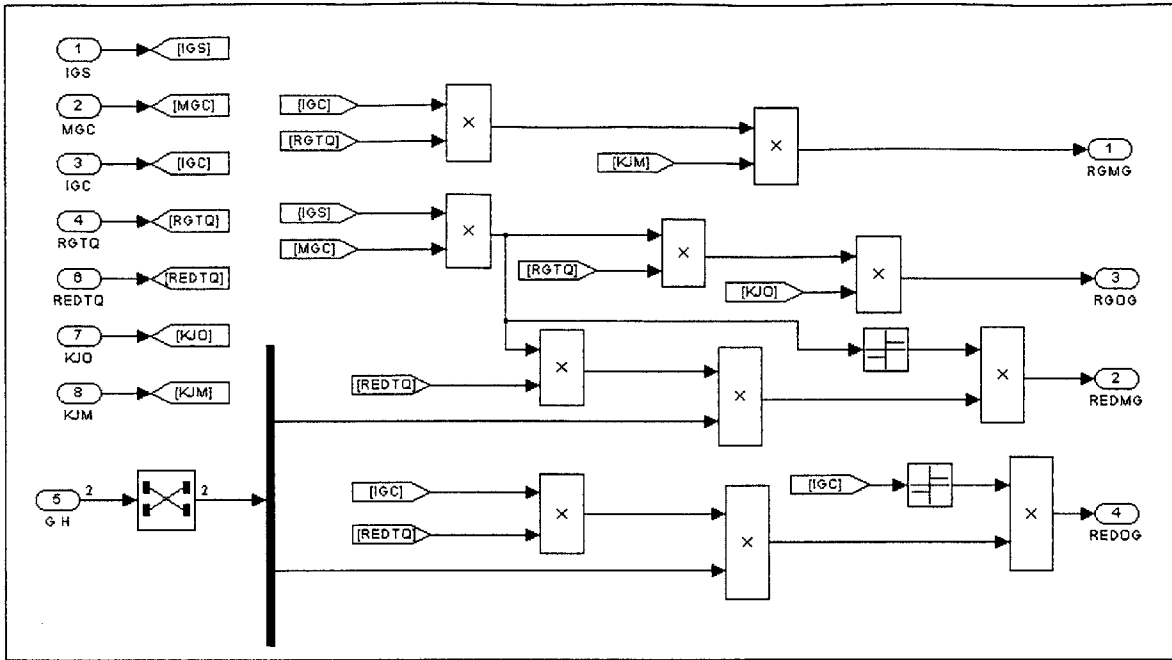
Figure D.16 - Block diagram of the resolution block.

The function of the block diagrams in Figure D.15 and Figure D.16 above are described in section 4.4.6.

Following is the redundant compensation block for the LQR controller, which is significantly different than for the classical controller.
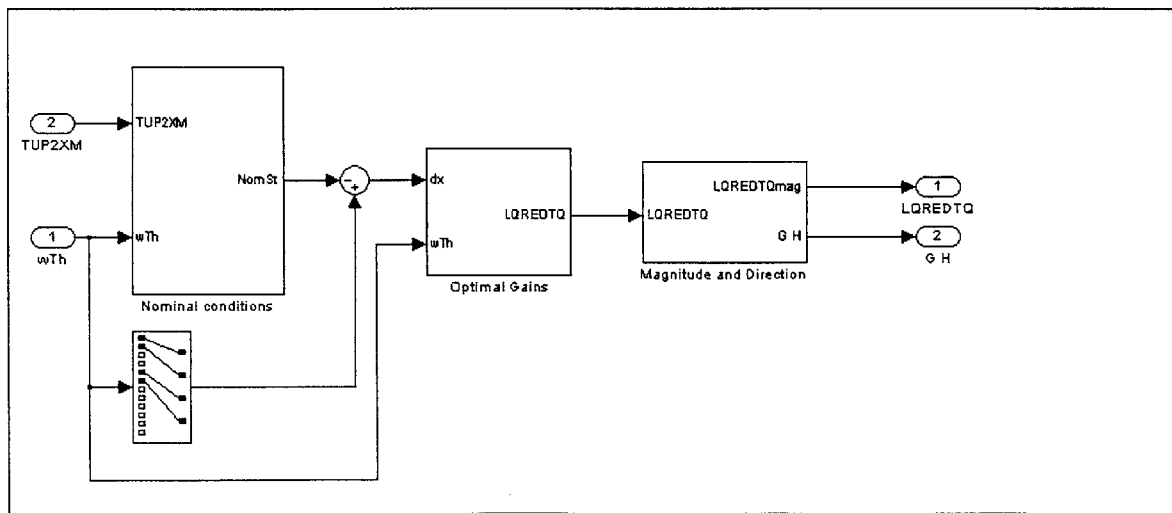
Figure D.17 - Block diagram of the redundant compensator for the LQR controller.

Figure D.17 is the LQR equivalent of Figure D.11 above. Functional descriptions of all the blocks in Figure D.17 are given in section 4.4. Block diagrams of each of the blocks follow.
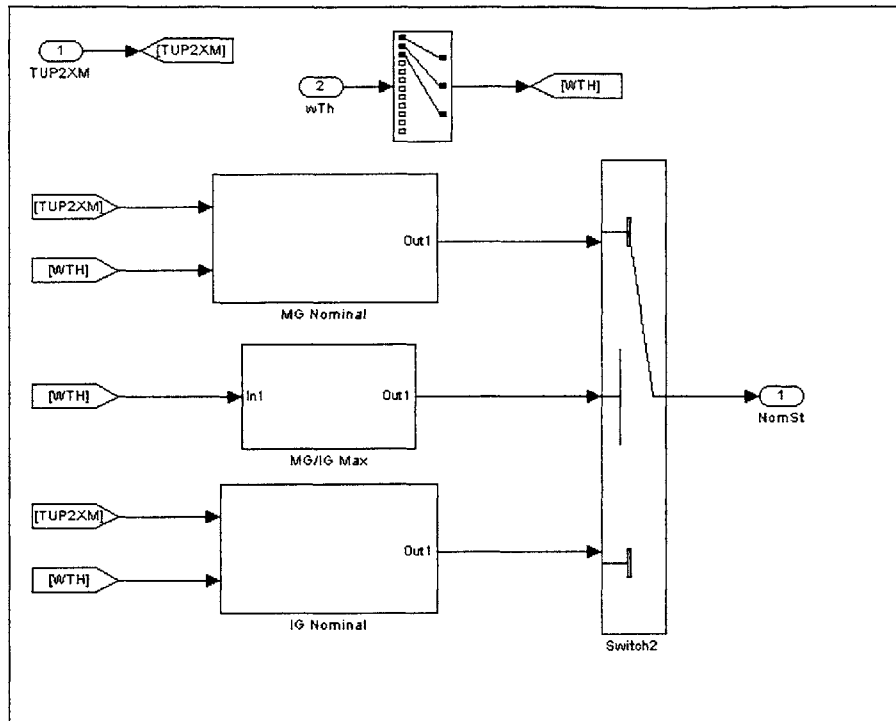
Figure D.18 - Block diagram of the nominal conditions block.

In Figure D.18 above, the choice between nulling the middle and nulling the inner gimbal is made.
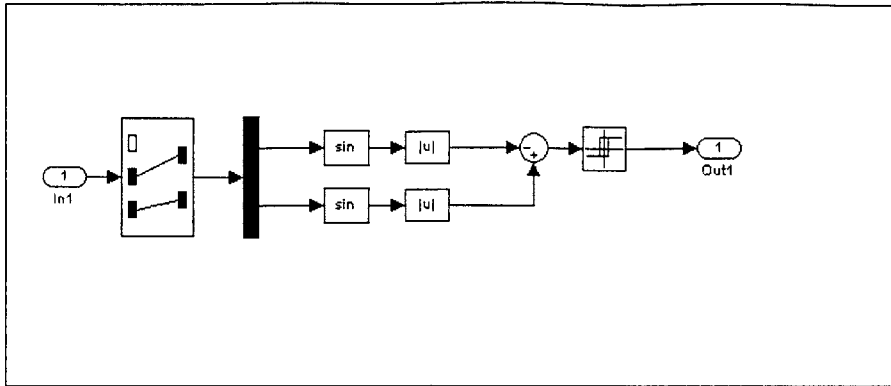
Figure D.19 - Block diagram of the MG/IG max block.

Figure D.19 displays the logic used to choose between nulling the middle gimbal and nulling the inner gimbal angle.
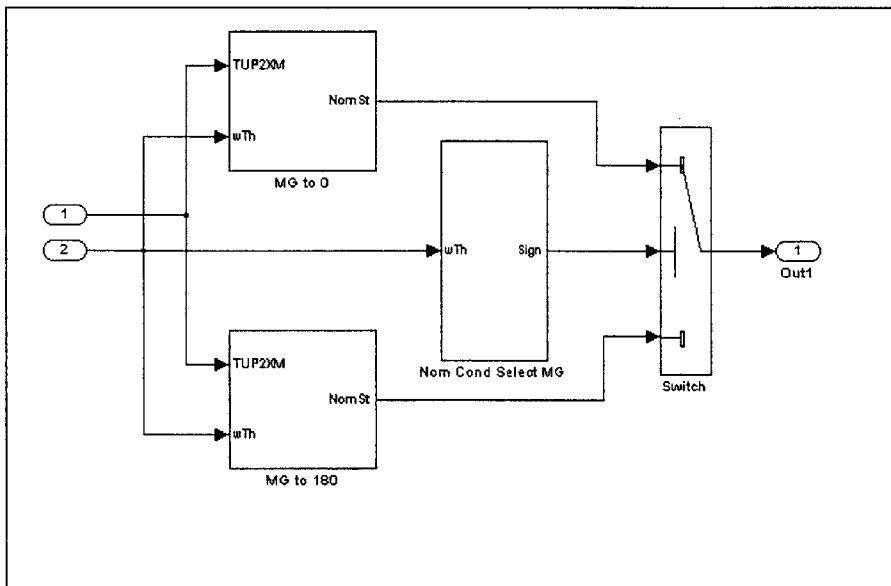
Figure D.20 - Block diagram of the MG nominal block.

In the case that the middle gimbal is nulled, Figure D.20 depicts the block where the choice of whether to drive the gimbal to 0 or 180 degrees is made. The IG nominal block looks equivalent, so it will not be repeated here.
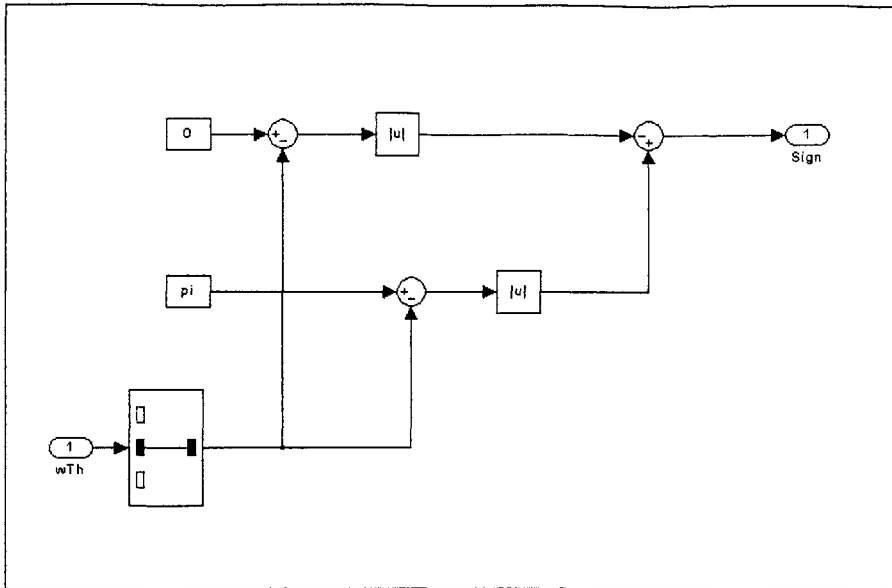
178

Figure D.21 - Block diagram of the MG nominal conditions selection block.

Figure D.21 shows the nominal conditions selection block of the middle gimbal angle from Figure D.20. The logic in Figure D.21 decides whether the gimbal will be driven to 0 or 180 degrees.
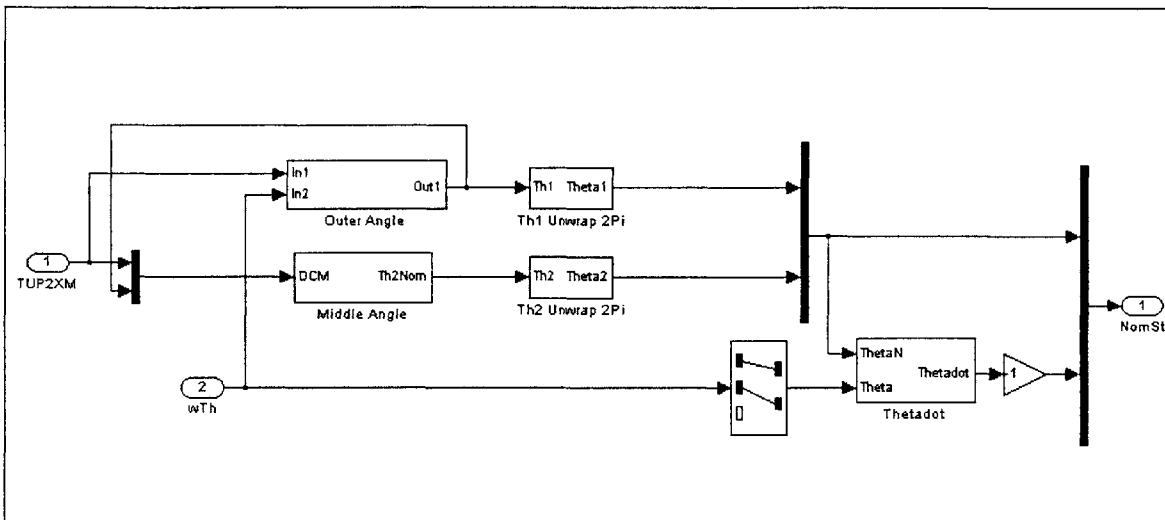

Figure D.22 - Block diagram of the IG to 0 block.

Figure D.22 shows the calculation of the nominal gimbal angles in the case where the inner gimbal is being driven to zero. Diagrams for the other nominal conditions are

equivalent and will not be repeated. Appendix C explains the function of all these blocks in computing nominal conditions for different values of middle and inner gimbal angle.
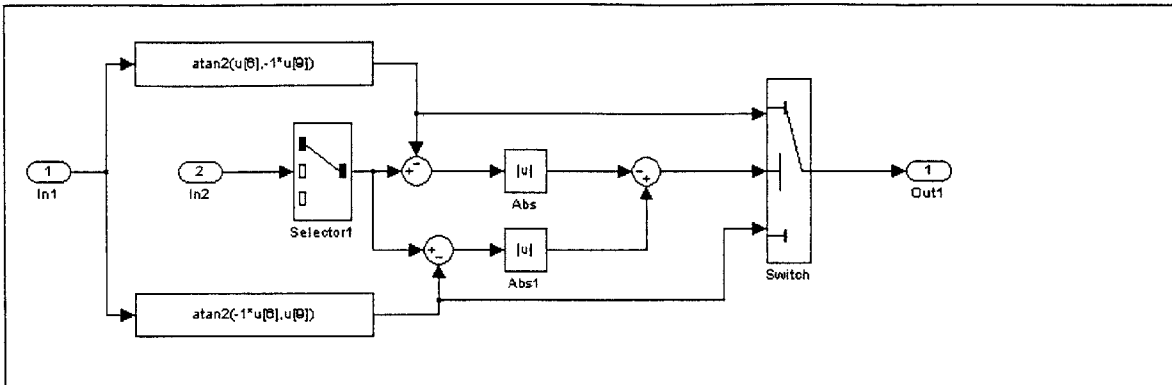

Figure D.23 - Block diagram of the outer angle block.

Figure D.23 above shows the calculation of the nominal outer gimbal angle. Two different equations are used as explained in Appendix C. The equivalent block for the middle gimbal angle, with the appropriate equations from Appendix C, will not be shown.
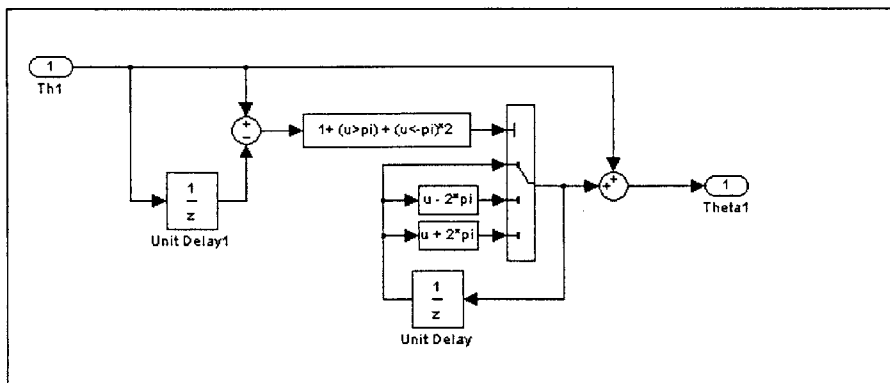

Figure D.24 - Block diagram of the angle unwrapping block.

Figure D.24 shows the outer angle unwrapping block from Figure D.22. As the inverse tangent functions used to compute the nominal angles only have a range of $\pm \pi$ and the actual gimbal angles have unlimited range, the unwrapping block corrects for situations

where the inverse tangent function jumps suddenly between $-\pi$ and $+\pi$. Equivalent unwrapping blocks for the other angles are not shown.
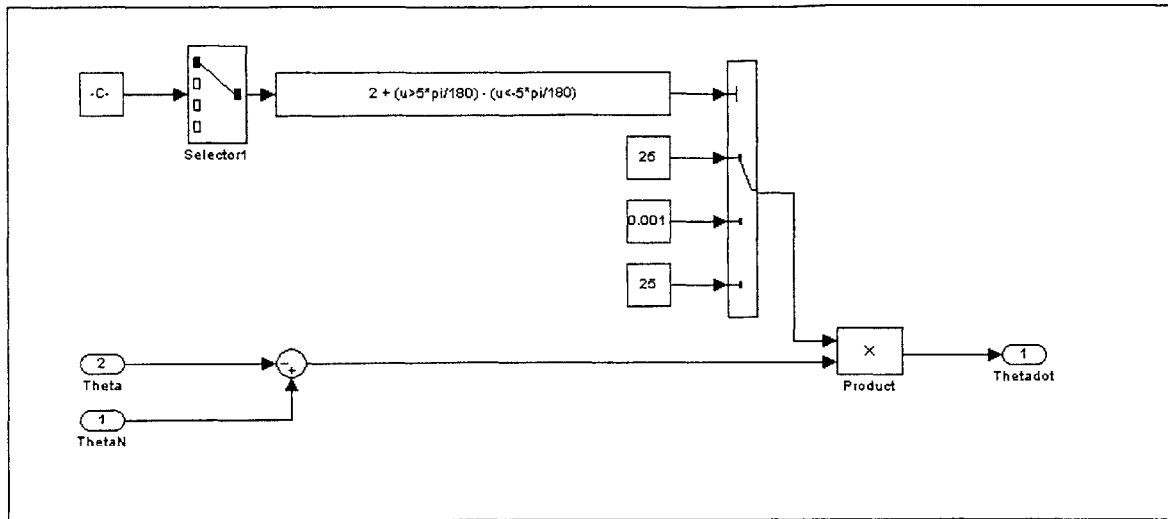

Figure D.25 - Block diagram of the theta dot block.

In Figure D.25, the nominal theta dot is calculated. Here, the logic which chooses the correct theta dot gain, as explained in section 5.3.1, is shown. The output of this block is the nominal relative angular rate and for zero case motion, the negative of the output is the nominal inertial angular rate as can be seen from (4.4.1).

In returning back to the LQR redundant compensator of Figure D.17, the following are the other blocks in the figure.
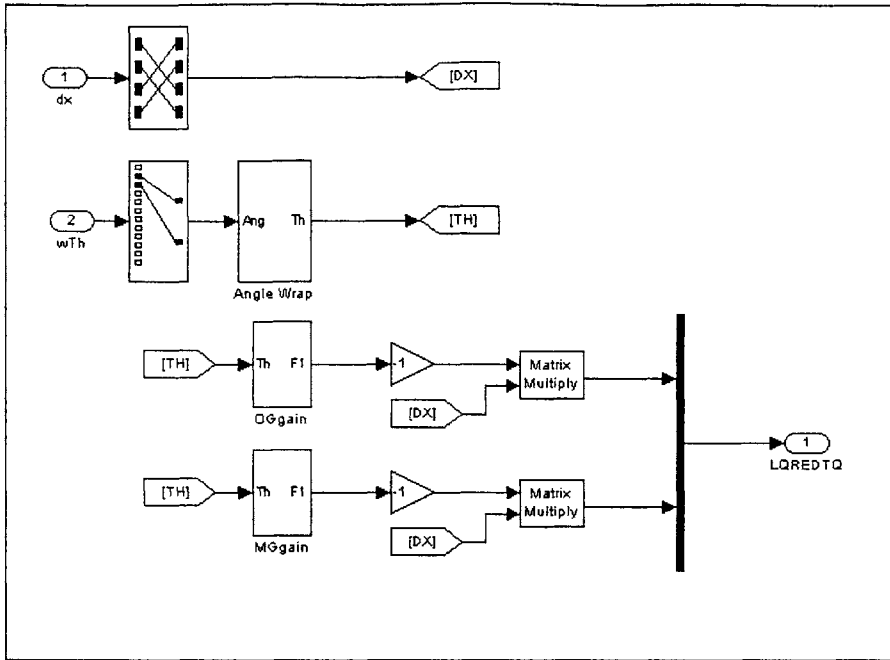
Figure D.26 - Block diagram of the optimal gains block.

Figure D.26 above shows the choosing of the optimal gain. With the optimal gain chosen, the perturbed states are multiplied by the gain. The outer and middle torque commands are treated separately in Figure D.26.
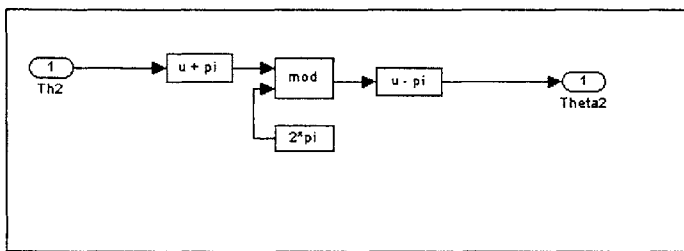

Figure D.27 - Block diagram of the angle wrap block.

Figure D.27 shows the angle wrapping from Figure D.26 above. This wrapping, which is essentially the inverse of the functionality in Figure D.24, is necessary so that the continuous middle and inner gimbal angles can be brought into the $\pm \pi$ range for use in the look-up tables.
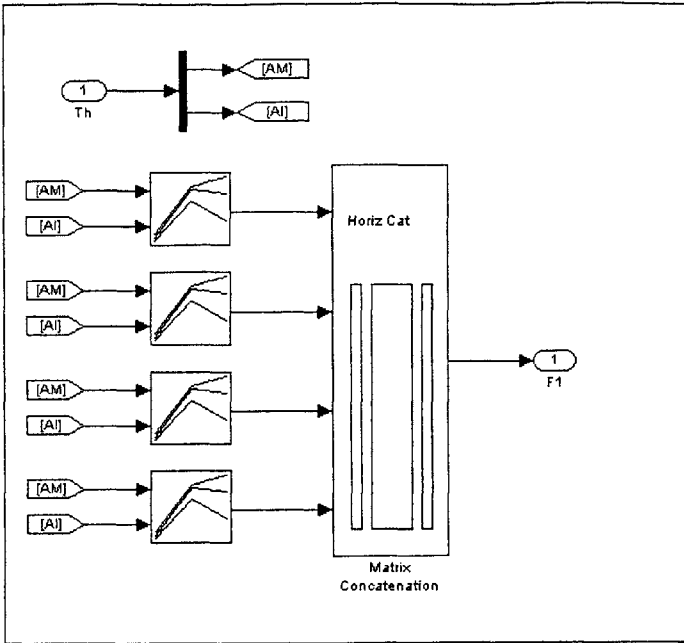
182

Figure D.28 - Block diagram of OG gain block.

Figure D.28 shows the OG gain block from Figure D.26. This block contains the look-up tables which store the various F gains based on the discretized nominal conditions. A look-up table is used for each term in the F matrix. The terms are concatenated into a vector which is matrix multiplied by the perturbed state vector resulting, in this case, in the outer gimbal torque command. An equivalent functionality is used for the middle torque command in the MG gain block, but is not shown.

Finally, the magnitude and direction block of Figure D.17 above will be presented below.
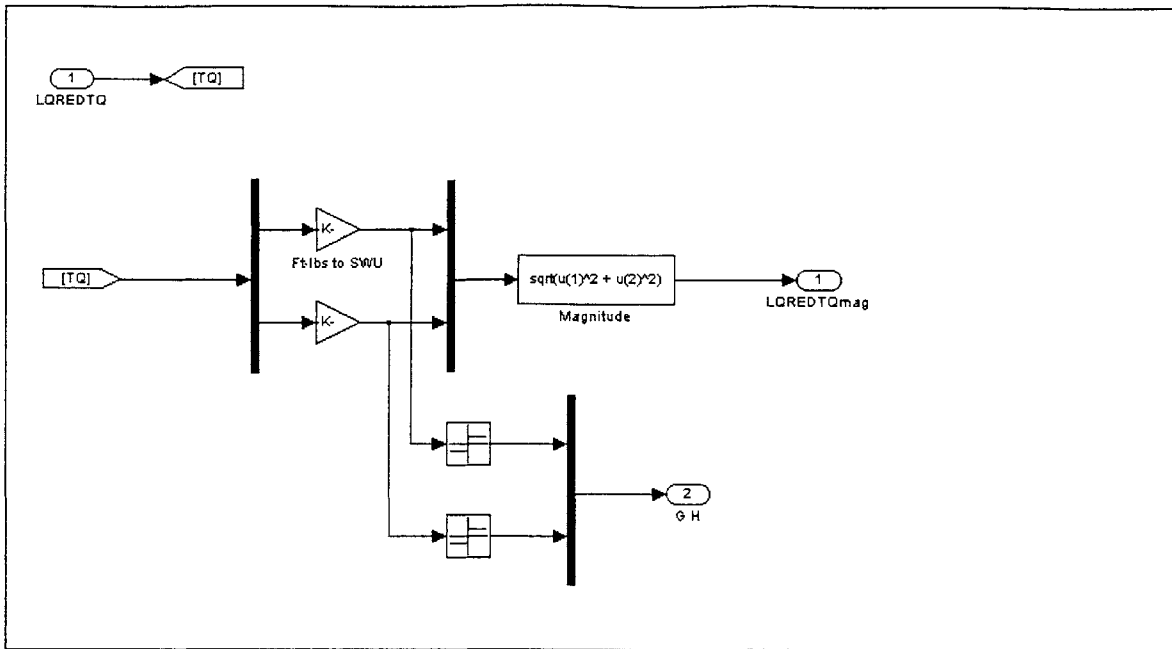
Figure D.29 - Block diagram of the magnitude and direction block.

The magnitude and direction block, as depicted in Figure D.29 above, determines the magnitude of the torque commands and saves the signs of the outer and middle components for use in the outer-middle gimbal torque resolution block of Figure D.15. This functionality is explained in section 4.4.5.

References

[1]   Greenspan, R. L., "Inertial Navigation Technology from 1970-1995,"
        NAVIGATION: *Journal of The Institute of Navigation*, Vol. 42, No. 1, spring
        1995, pp.165-185.

[2]   Kwakernaak, H., and Sivan, R., *Linear Optimal Control Systems*, John Wiley &
        Sons, Inc., New York, 1972.

[3]   Lewis, F. L., and Syrmos, V. L., *Optimal Control*, 2nd ed., John Wiley & Sons,
        Inc., New York, 1995.

[4]   Kirk, D. E., *Optimal Control Theory: An Introduction*, Prentice-Hall, Inc., New
        Jersey, 1970.

[5]   Franklin, G. F., Powell, J. D., and Emami-Naeini, A., *Feedback Control of
        Dynamic Systems*, 4th ed., Prentice-Hall, Inc., New Jersey, 2002.

[6]   Katz, P., *Digital Control Using Microprocessors*, Prentice-Hall International,
        Inc., New Jersey, 1981.

[7]   "Function Reference: dlqr," *Control System Toolbox Reference*, Ver. 5, The
        MathWorks, Inc., Natick, Massachusetts, 2002.

[8]   Zhou, K., Doyle, J. C., and Glover, K., *Robust and Optimal Control*, Prentice-
        Hall, Inc., New Jersey, 1996.

[9]   Woods, R. L., and Lawrence, K. L., *Modeling and Simulation of Dynamic
        Systems*, Prentice-Hall, Inc., New Jersey, 1997.

[10]   Hughes, P. C., *Spacecraft Attitude Dynamics*, John Wiley & Sons, Inc., New
        York, 1986.

[11]   Shabana, A. A., *Dynamics of Multibody Systems*, 2nd ed., Cambridge University
        Press, New York, 1998.

[12]   Chatfield, A. B., *Fundamentals of High Accuracy Inertial Navigation*, edited by
        P. Zarchan, Vol. 174, Progress in Astronautics and Aeronautics, AIAA, Virginia,
        1997.

[13]   Jekeli, C., *Inertial Navigation systems with Geodetic Applications*, Walter de
        Gruyter, New York, 2001.

[14]   Gennert, M. A., "Analysis of Optimal Control of a Four-Gimbal System," Masters
        Thesis, Massachusetts Institute of Technology, 1980.

[15]   Kayton, M., "Inertial Navigation," *Avionics Navigation Systems*, John Wiley & Sons, Inc., New York, 1969, pp. 281-341.